TEM investigation of growth mechanisms and microstructure of model YBCO coated conductor architectures deposited by metalorganic decomposition

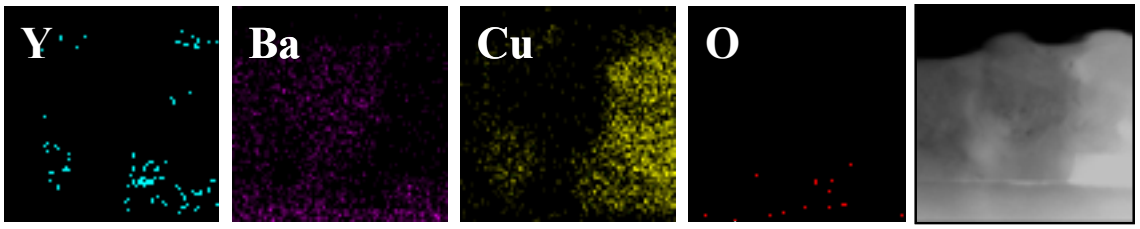

Jaume Gàzquez Alabart

2006

TEM investigation of growth mechanisms and microstructure of model YBCO coated conductor architectures deposited by metalorganic decomposition

Jaume Gàzquez Alabart

Programa de doctorat en Ciència de Materials
Department de química de la Universitat Autònoma de Barcelona

Departament de Materials Magnètics i Superconductors
ICMAB-CSIC

Director: Dr. Felip Sandiumenge
Tutor: Dr. Àlvar Sánchez

Memoria presentada per a l'obtenció del grau de doctor

Bellaterra, 6 de Novembre de 2006

Felip Sandiumenge Ortiz, Investigador Científic de l'Institut de Ciències de Materials de Barcelona del CSIC, i **Àlvar Sánchez**, Professor Titular de la Universitat Autònoma de Barcelona.

CERTIFIQUEN

Que en Jaume Gàzquez Alabart, Llicenciat en Física, ha dut a terme sota la seva direcció el treball que porta per títol "TEM investigation of growth mechanisms and microstructure of model YBCO coated conductor architectures deposited by metalorganic decomposition" i que queda recollit en aquesta memòria per optar al Grau de Doctor en Física.

I per a que així consti, signen el present certificat.

Director: Dr. Felip Sandiumenge **Tutor: Dr. Àlvar Sánchez**

Bellaterra, 6 de Novembre de 2006

ACKNOWLEDGMENTS

First of all a very special acknowledgment to Dr. Felip Sandiumenge, supervisor of this Thesis, thanks for all the opportunities you have given to me, for your confidence, your helpful advises, your support and of course for all the time you have dedicated to this work.

To Prof. X. Obradors, thanks for bring me the opportunity to work in his group, for his help, his advices and for showing so much interest in the topic I was working on.

To Dra. Teresa Puig for continuous support and teach me her knowledge about the superconducting world.

To Dra. Marie-Jo Casanove, for the nice time I spent in CEMES, Toulose, for her help and the exceptional welcome she gave me. I also want to thank Dr. Christian Roucau for his help in front of the CM30, to Dr. Yolande Kihn for her help me with the EELS facility, and especially to Dr. Jacques Crestou for his help in the field of samples preparation.

To Dra. Carmen Ballesteros, for all the facilities and advices she gave me during my stay in the Universidad Carlos III, Leganés.

To Dr. Jacques Rabier and Dra. Anne Proult, for their help when I was in the Laboratoire de Métallurgie Physique of Poitiers.

That work would have not been possible without the financial support of Spanish government's Ministerio de Educación y Ciencia, through its FPI fellowship.

People I will mention bellow has been directly involved in part of the results presented in that thesis. Firstly, I would like to thanks to the incomparable and tireless chemists of the Superconductivity group, Oscar Castaño, Andrea Cavallaro, Mariona

Coll, Neus Romà, Stéphanie Morlens and Anna Llordés, as well as Katerina Zalamova, who acts as a chemist too, for the samples they provided me. My work would have been impossible without taking advantage of their progress in CSD synthesis, otherwise. Thanks to Pep Bassas, Dr. Jordi Arbiol and Dr. Quim Portillo from the Serveis Científic Tècnics de la Universitat de Barcelona for all the time they dedicated to me. To Narcis Mestres and J.C. González for their Raman knowledge transferences. To Joffre Gutierrez, Jose Pérez and Alberto Pomar for the transport and critical current densities measurements present in this thesis. To Ángel Pérez, Andrea Cavallaro and Mariona Coll for their Atomic Force Microscopy images. To Bernat Bozzo for shearing his computing knowledge with me.

I would also like to thanks to all the colleagues and friends of ICMAB, being of my group or not, which have helped me in many cases during all this time. And, of course, I would like to express my appreciation to people from computing and workshop and sustenance teams for their disposition to help me at any time.

Finally, I would like to thank to Mariona for answering me repeatedly ‘where is the Montardo?’.

No puc oblidar a ma mare i a la Sara, per tenir cura del Lluc durant tants matins i tardes.

MOTIVATION

Any manufacturing method for coated conductors relies on the epitaxial deposition of a high T_c superconductor film onto a textured template of one or more oxide buffer layers and a normal metal substrate. Of all the high T_c superconductors, $YBa_2Cu_3O_7$ (YBCO) seems to be the most promising material due to the fact that it has an extremely high irreversibility field as well as the ability to carry high current densities in zero field if high angle grain boundaries can be eliminated. To do so, a substrate tape must be coated with an YBCO layer in such a way as to obtain both in-plane and out-of plane texturing of the grains (biaxial alignment). In addition, it is desirable to devise a method of depositing the buffer layers and the superconductor which is cheap and can be scaled up. In the recent years chemical solution deposition (CSD) methodologies have shown to be very promising to achieve cost-effective fabrication of second generation conductors. In particular, in 2001 the Superconductivity group at ICMAB took the challenge to produce all CSD YBCO coated conductors with a high critical current density in the scope of a European Project called SOLSULET. One natural extension of this research leads to the topic of this Thesis: *TEM investigation of growth mechanisms and microstructure of model YBCO coated conductor architectures deposited by metalorganic decomposition.*

Material defects control the overall critical current density of present conductors and these defects are intimately tied to their particular fabrication processes. The specifics of such particular fabrication process (CSD) are the scope of this thesis. Most of the experimental research has been focused on thin films deposited on single crystal dielectric substrates as model systems, studying the nucleation and growth process, the resulting microstructure and fundamental properties of both CeO_2 as a buffer layer and YBCO.

My task in the superconductivity group is X-ray diffraction (XRD) and transmission electron microscopy (TEM) analysis, which are particularly suited for studying the orientation of the film on the substrate, as well as secondary phases appeared during the growth process, and the local structure and structural imperfections of materials. Although during the first year of my stay in ICMAB I mainly worked on the X-ray diffraction characterization of samples, since the beginning and in collaboration with Jordi Arbiol I was also involved in the TEM sample's preparation. My visits at CEMES in Toulouse in April 2003 turned out to be decisive to consolidate my technique. Actually, during my PhD I have had the chance to collaborate with different European groups. The results presented in this Thesis arise from the fruitful collaboration with them.

This thesis is divided in six chapters. In the first one, we expose an amenable brief introduction to the YBCO compound, as well as to the CSD method. Then, in the second chapter we describe briefly the experimental techniques used for the physical characterization of the CSD thin films presented in this work. The results, chapters 3, 4 , 5 and 6, are presented in two parts: Part I reports many aspects governing the growth mechanisms of CSD films, in particular the identification of those factors controlling the evolution of microstructures, which remain poorly established in comparison with vacuum deposited films. We give first an account of the evolution from a partially oriented granular microstructure to a dense epitaxial one in CeO_2 films deposited from chemical solutions (chapter 3), and second the microstructural evolution of YBCO from trifluoroacetate precursors, which follow a complex compositional trajectory (chapter 4). In part II the microstructure of TFA-YBCO thin films with high critical current densities is analysed. We depict intrinsic structural defects occurring within YBCO films, focusing in extended defects which can lead to strong flux-pinning and high critical current density (chapter 5). The microstructure of TFA-YBCO films with artificial defects has been also studied (chapter 6). The inclusion of $BaZrO_3$ results in strong increase of the critical current density, demonstrating that chemical solution growth is a very flexible methodology to nanostructure YBCO films and coated conductors.

Finally, we present the general conclusions of this study.

CONTENTS

CHAPTER 1
INTRODUCTION

1.1 The structure of High-T_c superconductors

The ideal perovskite-type structure (space group $Pm\bar{3}m$) is described by the general formula ABX_3 and consists of corner-linked octahedra of X-anions (mostly O or F) with B cations at their centres and A cations at the sites in-between the octahedra. The structural modulations involve tilting if the octahedra or cation displacements. Partial substitution of cations can result in ordering giving rise to superstructure formation.

The spectrum of physical properties exhibited by pereovskites is broad, specially the electrical properties: ranging from insulator over semiconductor, conductor and even high-T_c superconductor (HTS). The perovskite related superconductors are layered copper oxides. The most investigated of these materials is $YBa_2Cu_3O_{7-\delta}$ (YBCO), a tripled perovskite with a cation ordering. We can describe the cuprates as identical copper oxide layers with invariable oxygen content, responsible for the superconductivity and different layers of other materials such as Cu, Pd, Bi, Tl etc. acting as a 'charge reservoirs'. Changes in the oxidation state of the charge reservoir can be transferred to the superconducting copper oxide layers, usually through the bridging oxygen. The two important factors governing the superconducting properties are the mixed valence of copper and the two-dimensionality of the structure. Structural modifications of these factors are the keys to synthesise superconducting materials [1].

1.1.1 The $YBa_2Cu_3O_{7-\delta}$ compound

The structure of YBCO consists of three perovskite blocks with a cation ordering Ba-Y-Ba. The Cu-O substructure consist of Cu(2) pyramidaly surrounded by O and Cu(1) atoms in a square planar configuration. The Y layer is free from oxygen and the Y-perovskite block is therefore contracted as compared to the Ba-containing perovskite blocks. A schematic representation is shown in Figure 1-1.

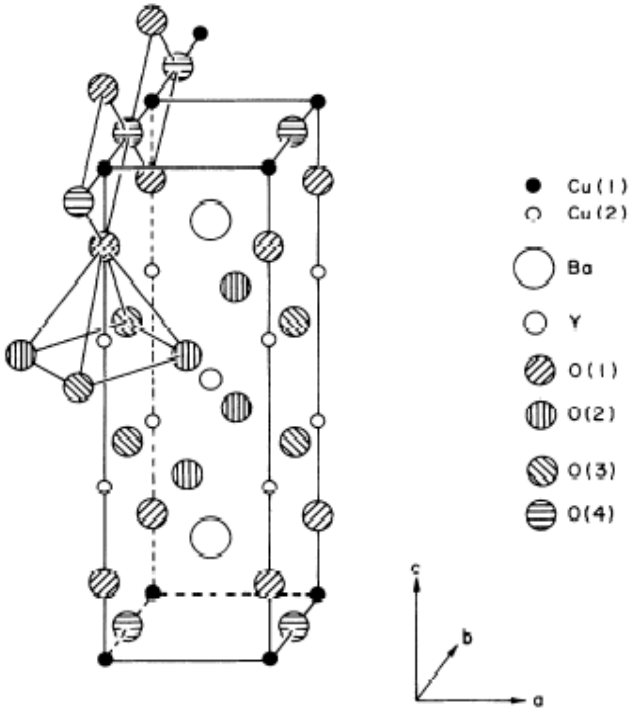

Figure 1-1. YBCO orthorhombic unit cell. YBCO is a complex, layered perovskite centered on a yttrium layer, around which are stacked the CuO_2 planes, and a double layer of BaO and CuO.

The oxygen content can vary between 6 and 7; i.e. non-superconducting, superconducting with reduced T_c of 60 K and superconducting with optimized T_c of 92 K. The structure of $YBa_2Cu_3O_7$ is orthorhombic P(mmm) with lattice parameters a = 0.3856, b = 0.3870 and c = 1.1666 nm [2].

1.1.2 Irreversibility line

An important property of YBCO relates to the ability of this material to carry significant currents at high external magnetic induction field and as any type II superconductor, the magnetic induction field penetrates the HTS cuprates in the form of vortices in the mixed state [1]. The vortices have a normal core of radius ξ. The core is surrounded by a region of larger radius, λ, within which superconducting currents are flowing. These currents generate a flux quantum in each vortex.

At a given temperature, each HTS material has a maximum magnetic field, B_{irr}, above which loss-free d_c current flow is not possible, dissipation starts due to motion of vortices at any small applied current. This line, called irreversibility line, is very important for application purposes since it sets the position from where the material is not anymore useful although it is still in the superconducting state [3].

Figure 1-2 shows the irreversibility line for typical superconductors and temperatures of cryogenic liquids. As it is shown, YBCO is the best candidate for high-power applications at 77 K at high external magnetic fields.

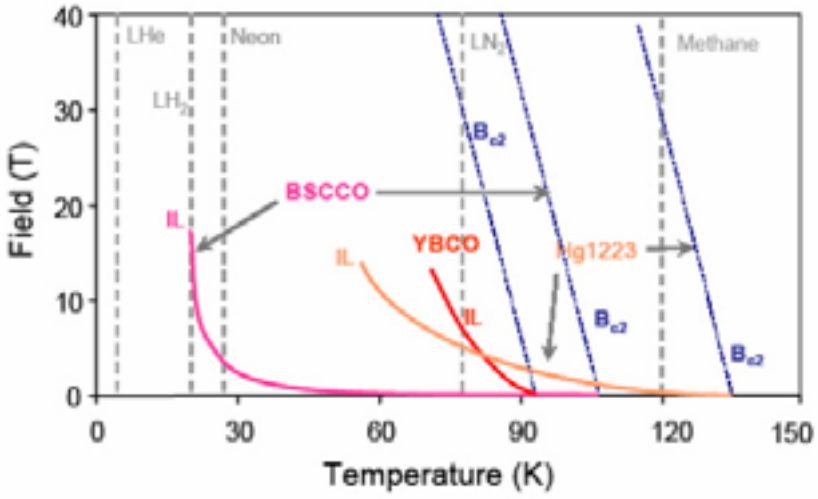

Figure 1-2. Upper critical fields (discontinued lines) and irreversibility lines (continued lines) for some HTS superconducting materials [3]. Superconductivity does persist up to the upper critical field B_{c2} [1].

1.1.3 YBCO thin films

A deposited layer onto a substrate can grow with randomly oriented crystallites, giving a polycrystalline film. The grains of the film can be identically oriented along the substrate normal but lacking orientation in the substrate plane. This is a film textured by growth, having uniaxial texture. When the grains of the film are oriented identically along the substrate normal and crystallographic directions in the substrate surface plane the films grows 'epitaxially' on the substrate. The term 'YBCO thin film' will be used for an epitaxial overgrowth of a high-T_c YBCO superconductor on a single crystal substrate. Typically the thickness of such films is around 300 nm. The limit on the thickness for a deposited layer to be called 'thin film' is associated with the loss of its epitaxy upon further growth. Furthermore, in the case of YBCO thin films, grain boundaries have a detrimental effect on the critical transport currents. Highly oriented thin films are a way to come around this problem. YBCO thin films are known to have the highest critical currents densities.

There are various deposition techniques to yield YBCO thin films of high quality. In all cases three atomic species have to be intimately mixed in the correct proportions to form the proper structure of the high-T_c materials. Moreover the temperatures to obtain epitaxial growth are rather high and close to the melting temperature (>700 ºC), and the oxygenation should be sufficient to obtain superconducting films. Typical ones are pulsed laser deposition (PLD) (see for example [4]), thermal evaporation [5,6], metalorganic chemical vapour deposition [7], liquid phase epitaxy [8], ex situ electron beam processing [9,10], metalorganic decomposition (MOD) [11,12,13,14] and the sol-gel process [15].

Characterization is an important part of YBCO thin film research. Due to the complexity of the deposition resulting in impurities or inhomogeneities the properties of thin films can differ from those exhibited by bulk samples. The superconducting properties strongly depend on the microstructure of thin films. Deviations from the perfect structure can be beneficial or detrimental depending on their nature, size and distribution. Important measurements include: the transition temperature T_c, the resistivity, the critical current density J_c, the stoichiometry, the crystalline perfection… As it will be discussed below, TEM characterization of YBCO thin films requires an

elaborate specimen preparation which is moreover destructive. Therefore it is combined with non-destructive techniques such as XRD, RHEED and AFM as will be illustrated in this work.

1.2 Second generation coated conductors

Since the advent of high temperature superconductivity a very wide extended effort has been carried out to develop high critical current conductors which may allow developing advanced power systems and high field magnets and hence fully exploiting the technological potentiality of these advanced materials. Due to the low current-carrying capability of "first generation" wires and tapes, particularly in modest magnetic fields, effort is now concentrated on development of a "second generation" (2G) of wires and tapes with higher critical current density which can be maintained in high magnetic fields [3,16].

YBCO coated conductors can support critical current densities, J_c, exceeding 2.1 A/m^2 (77 K, self field) on biaxially aligned substrates with an appropriate lattice match. Unlike typical conductors, oxide based superconductor materials are brittle and easily damaged and thus they are difficult to process and handle, especially in the form of large and flexible wires. Several approaches have been addressed for the preparation of these 2G conductors based mainly in vacuum deposition methodologies of epitaxial layers on top of metallic substrates. There are two methods to provide such templates for the epitaxial growth of the superconductor. The first method uses an untextured metal substrate along with a technique to induce texture in a buffer layer, yttria-stabilized zirconia (YSZ), such as ion-beam assisted (IBAD) [3]. The second method begins with a textured metal substrate, Ni, which is buffered with an epitaxial film for diffusion resistance and chemical compatibility with the superconductor. The rolling method to achieve a biaxially textured substrate is called RABITS [16]. These tapes, as substrates, present several difficulties at growth temperatures. The simple and direct deposition of YBCO in their top will lead to an unwanted interdiffusion, and they do not present good lattice match to YBCO.

These deleterious effects can at least be partly overcome by using a buffer layer between substrate and film. A number of properties are related to good quality buffers for the deposition of textured layers: they must provide a suitably textured surface to

promote the required ordered growth of the YBCO crystals so that only low angle grain boundaries result. This implies that the substrate lattice parameters are compatible with the deposited thin film. Furthermore the mechanical properties of the buffer should be adequate, i.e. it should have an expansion coefficient similar to that of the deposited YBCO thin film.

In this work we use CeO_2 on (001) oriented Y-stabilised ZrO_2 (YSZ) single crystal as a model system in view of the development of coated conductor architectures based on YSZ^{IBAD}/SS and on $La_2Zr_2O_7/Ni^{RABIT}$ by CSD. CeO_2 is the most attractive choice because of its good lattice match with YBCO. Considering $[100]CeO_2 \,||\, [100]$ YSZ, a 45º in-plane rotation of the orthorhombic YBCO with respect to the cubic CeO_2 results in a 1.8 % lattice mismatch in the ⟨010⟩ direction and a 0.2 % lattice mismatch in the ⟨100⟩ direction.

Chemical solution deposition (CSD) has only recently appeared as a low cost alternative for the fabrication of 2G coated conductors. The main advantage of this methodology is that low capital investment and supply costs are envisaged, thus becoming a competitive alternative to vapour deposition techniques requiring the use of vacuum systems. Sol-gel science is now a well established discipline which has reached a wide use for the production of materials with high performance such as nanoparticles, bulk ceramics, hybrid materials, mesoporous solids, coatings, etc [17,18]. In addition, another advantage of this technique for the preparation of advanced ceramics is that molecular scale homogeneity can be preserved during the gelification process and hence it allows to reach controlled nanostructures and to reduce the final firing temperature to prepare a compound. The achievement of oxide epitaxial films using CSD was demonstrated more recently and it was shown that the growth of epitaxial layers has as a driving force the elimination of grain boundaries in the random nanocrystalline film resulting after the pyrolysis [19].

1.3 Introduction to Chemical Solution Deposition

The film growth by chemical solution deposition (CSD) method is reviewed and summarized with emphasis on the growth of YBCO thin films and buffer layers.

The deposition method based on chemical solution has several advantages over the vacuum methods to deposit and grow thin films, as for instance excellent homogeneity and short processing times at low temperature. Furthermore, since it does not need high vacuum it is cost effective.

Two routes of CSD will be considered, sol-gel and metal-organic decomposition (MOD). There are some differences in the procedure: Sol-gel processes use alkoxide precursors that undergo primarily hydrolysis and condensation, which convert a liquid in a gel, and followed by a low temperature heat treatment. MOD route is simply based on the thermal decomposition of a metal-organic precursor. The most used route for the growth of YBCO films is the metal-organic decomposition of trifluoroacetates (MOD-TFA).

1.3.1 Sol-gel method

In the sol-gel processes, the precursors consist of a metal surrounded by ligands [18]. The ligands are organic molecules; the most widely used in sol-gel synthesis are alkoxides. The solution converts to a colloidal suspension of particles (with size between 1 nm and 1 μm) in a liquid named sol. Successive hydrolysis and condensation reactions form oligomer and finally inorganic polymers during the sol to gel conversion. The gel contains a solid polymer skeleton enclosing a continuous liquid phase.

In sol-gel route, the precursor is applied to the substrate surface by dip or spin coating. Then the evaporation of solvent takes place during a low temperature heat treatment, called pyrolysis. The densification approaches the reactive species.

1.3.2 Metal-organic decomposition

MOD routes use carboxylate precursors that do not undergo significant condensation reactions during either solution preparation or film deposition. Since the starting compounds are water-insensitive, they do not display the oligomerization

behaviour discussed above, and the precursor species that exist in the solution retain a strong resemblance to the starting molecules.

The MOD method consists on combining precursors of the desired metals in the corresponding ratio, which are deposited on substrates, and this precursor film is transformed in the final material by high temperature thermal decompositions.

This method possesses some limitations that must be overwhelmed. The large organic ligands may cause cracking during thin film processing due to excessive weight loss and shrinkage. To circumvent this, short chain carboxylate (e.g. acetate in the case of YBCO) and strongly chelating β-diketone (e.g. acetilacetonate in the case of CeO_2) compounds are used. Furthermore, for YBCO compounds, some difficulties arise due to the formation of barium carbonates ($BaCO_3$) instead of oxides during the firing process. Metal-organic decomposition using trifluoroacetates (MOD-TFA), first developed by Gupta et al [20], appears as a good alternative to grow YBCO films.

The MOD-TFA method to fabricate YBCO-based coated conductors involves several steps: solution preparation and deposition, pyrolysis of the metal-organic precursor leading to nanometric phases, and the growth process of the epitaxial crystalline phase.

1.4 Crystallization and microstructure development of films grown by CSD route

In the CSD route to epitaxial films, the solution is simply a vehicle to deposit the desired elements onto a substrate. During the heating, the solution decomposes to a polycrystalline inorganic film, which in turn, will be converted to a single-crystal film at higher temperatures. Since pyrolyzed films are typically amorphous or quasi-amorphous, film crystallization in solution-derived thin films occurs by a nucleation-and-growth process. The theoretical description for nucleation and growth processes in solution derived films is similar to those concerning the transformation of a gel into a glass, where an amorphous solid is transformed into a crystal material [21].

1.4.1 Nucleation and growth

The characteristics of nucleation and growth will define the microstructure of the films. In those where the nucleation takes place in the interface will display a columnar nature, whereas those in which the nucleation occurs throughout the film are polycrystalline with equiaxed grains. From a thermodynamic point of view, the driving forces that govern the transformation from a quasi-amorphous (pyrolized) film to a crystalline ceramic play a significant role in determining the nucleation events, and consequently, the microstructure. Figure 1-3 presents a schematic diagram of the free energies of solution-derived quasia-morphous film and the crystalline ceramic phase [21,22].

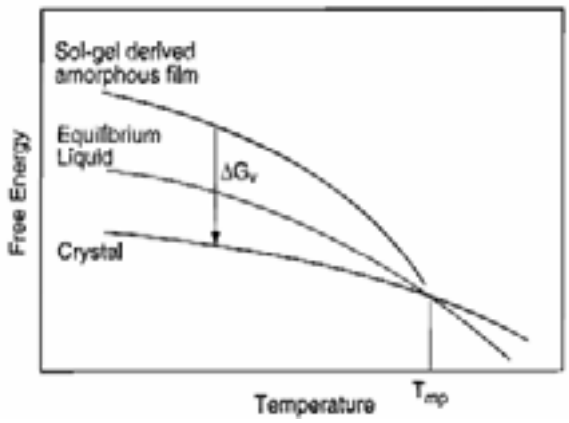

Figure 1-3. Schematic diagram of the free energies of a solution derived amorphous film, the ideal supercooled liqud, and the crystalline phase. ΔG_v is the thermodynamic driving force for crystallization [21,22].

ΔG_v is the driving force of the crystallization, i.e. the difference in free energy between the amorphous and crystalline states. It is important since it influences the barriers for nucleation of the crystalline phase at different locations within the film: substrate interface, surface, bulk. The energy available (via heat treatment during the crystallization anneal) to surmount these different nucleation barriers define which of the nucleation events take place and thus the resulting microstructure.

The crystallization driving force is determined by the free energy of the two material states and the temperature at which crystallization occurs. The free energy of the crystalline phase is lower than the amorphous one due the thermodynamic stability

(lattice energy). The energy barriers for homogeneous and heterogeneous nucleation (see e.g. [22]), and their dependence on driving force, are:

$$\Delta G^*_{\mathrm{hom}o} = \frac{16\pi\gamma^3}{3(\Delta G_v)^2} \qquad \text{Eq. 1-1}$$

and

$$\Delta G^*_{hetero} = \frac{16\pi\gamma^3}{3(\Delta G_v)^2} f(\theta) \qquad \text{Eq. 1-2}$$

where γ is the interfacial energy, ΔG_v is the driving force for crystallization, i.e. the free energy difference per unit volume associated with the amorphous film-crystalline film transformation, and $f(\theta)$ is a function related to the contact angle, θ, according to equation (for a hemispherical nucleus):

$$f(\theta) = \frac{2 - 3\cos\theta + \cos^3\theta}{4} \qquad \text{Eq. 1-3}$$

The difference in barrier heights for interface, surface and bulk nucleation is therefore defined by the surface energy term, the driving force for crystallization, and the contact angle with substrate.

A few concepts need to be kept in mind to use the diagram in Figure 1-3 to interpret film crystallization behaviour:

The transformation pathway (from the amorphous film to the final crystalline ceramic) has a major effect on nucleation and growth behaviour. *As the crystallization driving force is increased*, bulk nucleation becomes as probable as interface nucleation. Although the $f(\theta)$ term still results in a lower energy barrier for interface nucleation, when ΔG_v is high, there is more than sufficient energy to surmount the energy barriers for all (including less energetically favourable) nucleation events. Unless rapid thermal processing techniques are used, film crystallization usually begins during heating to the growth temperature. Therefore, *as the temperature increases*, more energy becomes available to surmount the barriers for nucleation events in addition to the energetically most favourable nucleation event. Crystallization *at higher temperatures* results in lower ΔG_v, and due to the $f(\theta)$ term, lower energy heterogeneous nucleation events become more important.

1.4.2 Epitaxial grain growth

Keeping in mind that highly oriented CeO_2 and YBCO are required for the fabrication of coated conductors, the control of nucleation at the interface is needed. In the case of YBCO that is processed at high temperatures, lattice matching with the substrate is a key factor in the preparation of epitaxial films. Considering the diagram of Figure 1-3, nucleation at higher temperatures implies that the crystallization process occurs with a lower driving force, which causes heterogeneous nucleation at the substrate to become more important in defining microstructure.

When the film and the substrate have similar structures, despite different chemistry, and their lattice mismatch is small, $f(\theta)$ is expected to be < 1, the development of epitaxial films involves the growth of small, nonometer sized grains at the substrate/film interface. The grains eventually grow along the interface and then through the film to consume randomly oriented grains. YBCO epitaxial growth becomes more complicated; crystallization can be delayed to higher temperatures, which means that during heating metastable phases, extended solid-solutions and nonequilibrium structures can crystallize, as in fact they do.

When a strong chemical interaction exists between a film and a substrate, and the lattice mismatch is less than 4 %, films can grow epitaxially layer by layer, via the named Frank-van Der Merwe mechanism. However, when the chemical interactions and lattice mismatch are not so good the film grows by three-dimensional nucleation of islands, which grow until they impinge to each other and coalescence to form a film. This growth mechanism is referred as Volmer-Weber mechanism. And there is another mechanism, close to the latter, in which a polycrystalline, continuous film, undergoes grain growth after a *post-nucleation* process: grain growth is driven by the reduction in boundary energy as the total grain boundary area is decreased. When the size of the grain is comparable to the film thickness, the energy of a grain in a thin film includes not only the energy associated with the grain boundary, but also the energy of the top and bottom of the film. This energy is usually dependent on the crystallographic orientation of the grain, so those grains having favoured epitaxial orientation grow at the expenses of grains having a less-favoured one, leading to abnormal or secondary grain growth [23].

1.4.3 Motion of grain boundaries

The diffusion of atoms is generally necessary for changes in microstructure to take place in processes such as the densification of films, grain growth and the formation of solid-state reaction products. Diffusive mass transport takes place when there is a gradient in the chemical potential and when the species in question have sufficient mobility.

Mobility is defined as the velocity of an entity per unit driving force (M = v /F). Depending on the process under consideration, this driving force may be a chemical potential gradient, an electrical potential gradient (electric field), an interfacial energy gradient, elastic strain energy gradient, and so forth. So, it is possible to define mobility for atoms, electrons, dislocations, grain boundaries or other entities. For atomic transport, the diffusion coefficient, D (of the Fick's first law $J = -D\ (dC/dX)$), is directly proportional to the atomic mobility [24]:

$$D = kTM \qquad \text{Eq. 1-4}$$

where k is Boltzmann's constant, T the temperature and M the mobility due to the gradient in the *driving force*.

We limit our discussion to grain boundary and lattice diffusion and the role of defects. Grain boundary motion can be seen as atoms crossing the plane of the boundary. This process is always necessary, but it is not always the slowest or rate-limiting step. When it is, the mobility is termed *intrinsic*, and is given by the mobility of atoms moving across the boundary (D_b/kT), divided by the number of atoms involved per unit area of grain boundary (δ/Ω):

$$M_b = \frac{D_b \Omega}{\delta kT} \qquad \text{Eq. 1-5}$$

where Ω is the atomic volume and δ is the boundary thickness. For a ceramic solid in which both cations and anions must diffuse, the limiting diffusivity D_b is the slower of the two.

We need also to keep in mind that pores, inclusions and secondary phases could also exert a drag force on the boundary. Furthermore, if the solute concentration is high enough it would become a grain growth inhibitor. *Solute drag* occurs when a strong interaction between segregated impurities and the grain boundary requires the solute distribution to be carried along the moving boundary. Solute diffusion in the near

boundary region is usually slower than the intrinsic diffusion of host atoms across the boundary plane, and becomes rate-limiting. From a solute drag theory, in the limit where the intrinsic drag is negligible compared to the solute drag, the mobility is given by [24]:

$$M_b(solute\ drag) \approx \frac{D_s \Omega}{2\delta kT\left(C_s e^{U/RT}\right)} \qquad \text{Eq. 1-6}$$

where D_s is the solute diffusivity, Ω is the atomic volume and δ is the boundary thickness, k is Boltzmann's constant, T the temperature, C_s the bulk concentration, U the interaction energy between the solute and the boundary plane and R the gas constant. We see that the grain boundary mobility is directly proportional to the rate-limiting diffusivity and inversely proportional to the segregated concentration of solute.

The grain boundary mobility is a velocity per unit driving force (M = v /F). The change in chemical potential of atoms across a curved grain boundary is the driving force that makes the boundary move towards its centre of curvature. Over some range of driving force (e.g. grain size) the solute drag mobility is a constant –the velocity increases in direct proportion to the driving force. However, the amount of segregation carried by the boundary is not constant with velocity. The theoretical relationship between velocity and driving force is shown in Figure 1-4.

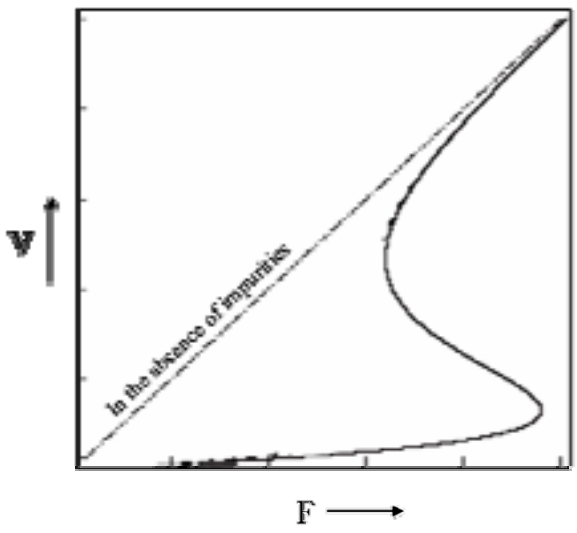

Figure 1-4. The grain boundary velocity–driving-force relation in the absence of impurities (dashed line) and in the presence of solute drag (continue line) [25].

For a sufficiently high driving force, it is able to break away from the solute drag cloud altogether and migrate at the intrinsic velocity. The region where the slope is negative is unphysical. At a driving force where such a solution exists, the steady-state velocity will be that given by one of the two parts of the curve where the slope is positive [25]. In both cases there are two regimes of the boundary motion: small velocity regime, where the boundary mobility differs from that in the pure system by several orders of magnitude, and a high velocity regime, where the impurity drag effect is relatively small. In the small velocity regime the boundary mobility is solute-drag limited, and a high velocity regime, where the impurity drag effect is relatively small and there is a sudden transition (“breakaway”) to the intrinsic mobility.

CHAPTER 2
SAMPLE CHARACTERIZATION

2.1 Experimental techniques

The techniques that we have directly used in this Thesis to characterize YBCO/CeO_2/YSZ multilayers and YBCO thin films are presented in this section.

As a member of a multidisciplinary group I am in charge of TEM and X-rays characterization of thin films. It is worth noting that during my PhD I have had the chance to collaborate with different European groups, and to work with different microscopes: a Philips CM30 operated at 300 kV and a Jeol 2010 FEG operated at 200 kV and equipped with a Gatan Image Filter 200 EELS spectrometer with an energy resolution of 0.8 eV, located in the Serveis Cientifico Tècnics de Barcelona in Barcelona. A Philips CM30 operated at 300 kV and a Philips CM20 operated at 200 kV and equipped with a Gatan Image Filter 200 EELS spectrometer with an energy resolution of 0.8 eV, located in the Centre d'Elaboration des Matériaux et d'Etudes Structurales (CEMES-CNRS) in Toulouse, thanks to the collaboration with Dr. Marie-jo Casanove. A Philips Technai STEM microscope equipped with EDX, operated at 200 kV, located in Universidad Carlos III de Madrid in Leganés (Madrid), thanks to the collaboration with Dr. Carmen Ballesteros. Finally a Jeol 200 CX operated at 200 kV, located in the Laboratoire de Métallurgie Physique in Poitiers, thanks to collaboration with Anne Joulien.

X-rays texture analysis has been performed at the Serveis Cientifico Tècnics de Barcelona in Barcelona and in the ICMAB, using a Philips MRD and a Brucker GAADS system.

The Reflection High Energy Electron Diffraction measures presented in this work have been performed at the Götinghen University and in the Leibniz Institut für Festkörper und Werkstoffforscung (IFW) of Dresden.

The Atomic Force Microscopy images shown in the present work were measured in a Microscopy PicoSPM (Molecular Imaging) system, located at the ICMAB, performed by A. Pérez, A. Caballaro and M. Coll.

Critical current densities measurements have been performed at the "Institut de Ciència de Materials de Barcelona (ICMAB)" carried out by Dr. A. Pomar, J.M. Pérez and J. Gutièrrez.

2.1.1 Structural aspects: TEM

The electron microscope is a powerful and versatile tool for materials science investigations. It offers a variety of information obtained from different operation modes such as bright field (BF) and dark field (DF) imaging, selected area electron diffraction (SAD) and high resolution lattice imaging (HREM). The functioning and the underlying principles of the electron microscope will not be detailed here. Excellent textbooks exist giving a complete introduction to electron diffraction and imaging [26,27,28].

BF and DF imaging are used to characterise defects and domain structures. SAD combined to tilting of the crystal in the microscope allows reconstructing the reciprocal space and in that way obtain information of the crystal structure, and identifying different phases. HREM allows, under certain conditions, to visualise directly the projected crystal potential.

2.1.1.1 Specimen preparation

Cross sections

Understanding the epitaxial growth of our oxide films on substrates and buffer layers is necessary and requires transmission electron microscopy analysis in cross-section. The preparation of such TEM cross-sectional (XTEM) samples is difficult for different reasons. The substrates $LaAlO_3$ (LAO), $SrTiO_3$ (STO) and YSZ single crystals are insulating and extremely hard in comparison with YBCO and CeO_2 films. The mechanical polishing of such samples requires extreme care due to the fragility of such substrates. Furthermore, the ion milling rates of LAO or YSZ and oxide films are significantly different, oxide films are thinned faster than substrates. There is another difficulty to be overcame, namely that these substrates become charged during the ion milling and deflect the ion beam, slowing down the milling rate.

Instead of these difficulties the TEM cross-section samples are possible if one proceeds carefully. Figure 2-1 presents the method used and its steps.

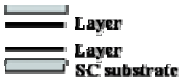

Figure 2-1. Sketch of the preparation process: the sample is cut in two halves and glued face to face, then mechanically polished down to 20-30 μm. Finally, glued on a grid and ion etched from both sides until a hole appears in the interface.

The typical dimension of substrate wafers is 5mm x 5mm and 0.5mm thick. The sample is cut in two pieces with a low speed diamond saw (with a damage of about 100μm thick) and glued face to face with epoxy glue. It is needed to press carefully so the glue spacing between the halves is as low as possible. After that, the sandwich is heated at 80ºC for 8 hours so that the glue hardens by polymerization. The next step is cutting the sample in slices with the diamond saw in the direction perpendicular to the YBCO-substrate interface. Such a pieces (~ 400-500 μm thick perpendicularly to the interface) are ground on both faces with SiC 600 paper down to 200 μm, then both faces are mirror-polished with diamond-coated abrasive foils of 15, 6, 3 and 1 μm grains down to 20-30 μm thickness. During the whole polishing procedure, which is done with a tripod, the sample was continually kept under an ethanol jet. Finally, the 20-30 μm thick sample is glued with M-Bond 610 on a grid (a 3 mm diameter cupper ring) and ion etched from both sides, first in a Fishione's 1010 LAMP Ion Mill machine, using a liquid nitrogen cooled stage, operated at 3.5 kV, 5mA and 10º during ~ 5 hours, and second in a PIPS (Gatan's precision ion polishing system) machine operated at 5 kV, 0.5 mA with a 8º angle for ~ 1 hour, 6º for 1-2 hours until a hole of ~ 0.5 mm diameter appears in the middle of the sample (see Figure 2-2). In the last step the sample is ion milled for a 15 minutes at 3 kV under an angle of 4º. The corners of the hole are thin enough for electrons going through, i.e. to be transparent to electrons.

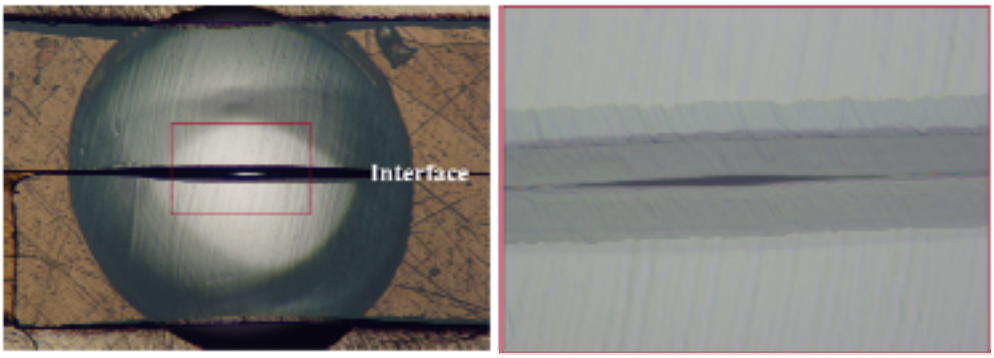

Figure 2-2. Picture of a cross sectional TEM sample glued on a cupper ring (russet color) and the magnification of the little hole (framed in red) done by PIPS. The corners of the hole are thin enough to ensure the electron transparency.

The key steps of the preparation are:

1. After cutting the sample in two halves, pressing the two pieces in order to get the thickness of the glue as thin as possible. It will ensure an optimal ion milling rate, i.e. if the glue quantity is too high the ion mill will remove it quicker than the sample, resulting a hole with a sharp edge, opaque to electrons.
2. The single crystal substrates are very hard but fragile, so a carefully sample polishing is required. With thicknesses < 20 μm cracks appear through the sample, and then it can not be handled any more.
3. We are dealing with single crystals and layers having different structures, thus the thinning rate will depend on specimen crystal structure. The angle of incidence of the ion beam is quite important, high angles mean rapid thinning but it could lead to undesired surface roughness and differential thinning, i.e. soft material will be removed faster than harder one. High energies could lead to ion implantation, amorphous layers, point defects, phase changes …
4. The ion radiation charge insulating substrates and deflect the ion beam, being a critical issue to deal with: the deflection of the ion beam produce the disappearance of the cupper ring where the sample is glued. This leads to an extremely fragile TEM specimen. It has been observed that cooling the sample during ion milling reduces this effect.

Planar Views

A planar view specimen allows us to study the microstructure in the plane parallel to the substrate surface. A piece of 2.5 by 2.5 mm is sawn from the film wafer by using a diamond saw. This piece is mounted with the film side glued in the tripod holder by means of wax and then polished on various diamond-coated abrasive foils of 15, 6, 3 and 1 μm grains, down to 20-30 μm thickness. The polishing is performed on the substrate surface. As in the previous case, the specimen is mounted on a cupper grid with a centred hole. Finally, ion-beam etching from the substrate side under different angles (from 8º to 4º) is performed in a PIPS machine operated at 5 kV and 0.5 mA.

2.1.2 Compositional analyses: EDX and EELS

In addition to structural information, chemical information can also be obtained within the electron microscope. The inelastically scattered electrons transfer part of their energy to the specimen. The energy transferred to the specimen is then released in different ways and, if detectable, the different signals may be collected.

X-ray energy dispersive spectroscopy (EDX): An electron entering the material will interact with the electron cloud around each nucleus, and transfer part of its energy to the electrons of the material. As one of the results, electrons in the atomic shells will gain sufficient energy to escape from the bounding of the nuclei. Thus, the atom is ionised. When this happens, the atom is left with an electron vacancy in one of its shells, and a way to fill its vacancy is catching one of the electrons from another shell. This electron with higher energy jumps into an inner shell and the difference in energy is released as emission of an X-ray quantum. Since the electron energy levels of the atomic shells are distinctive and since the allowed jumps from one shell to another are subjected to quantum mechanical rules, the energy of the emitted X-ray quantum is characteristic [26].

When an electron probe is scanning across a specimen linearly or rectangularly in STEM mode, the X-ray signal at each pixel may be collected simultaneously. The amount of characteristic X-ray of certain chemical elements may be displayed as plotted

curves or as pixel brightness in a two-dimensional presentation. It is called X-ray mapping.

When an electron beam hits an atom in the specimen it can eject an electron from its orbit around the nucleus losing an amount of energy. These inelastic scattered electrons carry some information, which may be also used to characterize the sample: by acquiring the **electron energy loss spectrum (EELS)** [26,29].

Plasmons are collective electron excitations in the solid state and it can give some information about dielectric constants or optical properties. The inner shell excitation provides valuable information about the chemical composition of the sample. Furthermore the shapes and positions of these peaks (called edges) have information about the valence, bounding and coordination of the corresponding atoms. Moreover, this information may be obtained in a TEM with a lateral resolution down to atomic level.

For EELS the microscope is equipped with an Imaging Filter, which is mounted underneath the projection chamber. The Filter accepts electrons passing through an entrance aperture at the centre of projection chamber. The electron beam passes through a magnet prism that separates the electrons according to their energy. Thus an EELS spectrum is obtained in the energy dispersive plane. In the imaging mode the lenses restore the image at the entrance aperture so it can be viewed on a TV or recorded on a slow-scan camera. By filtering and selecting a range of energy it is also possible to record a map. In spectrum mode the energy dispersive plane is projected in different magnifications on the slow-camera to acquire the EELS spectrum of the illuminated area of the sample.

2.1.3 Surface studies: RHEED and AFM

Reflection high energy electron diffraction (RHEED): The main traditional application of RHEED is the examination of surface reconstructions and surface roughness. It gives a statistical view of disorder rather than a local picture. The RHEED geometry is quite simple; an electron beam, of energy 5 to 30 keV, is directed at a glacing angle of ~ 1º at a single crystal held in the centre of an ultra-high vacuum chamber. Diffracted electrons fall on a phosphor screen on the other side of the chamber

giving a streaked pattern, which depends on the structure and morphology of the proved surface. Diffraction results when the Laue condition is satisfied: k_i-k_o = G. Where k_i and k_o are the wave vectors for the diffracted and incident beams, respectively, and G is the reciprocal-lattice vector. So the reflection diffraction pattern consists on spots aligned on Laue circles. For a surface with domains, e.g., terraces, grains, etc., the spots on the arcs are elongated into streaks perpendicular to the shadow edge. This is explained in terms of broadening of the reciprocal rods, i.e., the cross-sections between the reciprocal rods and the Ewald sphere become longer. In case of a rough surface, the e-beam can penetrate through surface islands. In this case, the electrons produce 3D Bragg diffraction and a spotty RHEED pattern that looks like an image from a transmission electron microscope. The variation of the RHEED intensity along the streaks is related to the step density of the surface and can be used to study basic growth processes [30].

Atomic force microscopy (AFM) enables to obtain surface images with an excellent resolution. The analysis can be done in air and is non destructive for the sample. An atomically sharp tip is mounted on a flexible cantilever and the sample is attached to a XYZ piezo-element. The van der Waals forces between the tip and the atoms of the sample surface are sufficient to deflect the cantilever. This is detected by analysing the reflection of a laserbeam on the cantilever with light sensitive diodes [31,32,30].

2.1.4 Average analysis of epitaxy: X-ray diffraction

In general, diffraction is possible when the length of the wave is of the same order of magnitude as the distance between the regularly spaced scattering objects. That is why X-rays analysis becomes important in materials science. In our case X-ray diffraction gives us information about the phases present in our thin films, their structure, orientation and quality.

A diffracted beam may be defined as a beam composed of a large number of scattered rays mutually reinforcing one another. To do so they need to be in phase. Two scattered rays are in phase if their path difference is equal to a whole number n of wavelengths. Scattered rays emerging from a plane surface as a result of a beam incident to that surface have a path difference equal to a whole number of wavelengths

if $n\lambda = 2d_{hkl} \sin\theta$, where d_{hkl} is the distance between diffracting planes in the crystal and θ is the angle between the incident beam and the surface. n is called the number of reflection and is an integer [33,34].

To use the Bragg law, two things are worth to remember: the normal to the reflecting plane and the incident and diffracted beams are always coplanar. The angle between the transmitted beam and the diffracted one is 2θ. The shape and the size of the unit cell solely determine diffraction directions. All we can infer by looking at the directions of the diffracted beams are the dimensions of the unit cell.

The position of the atoms in the unit cell will affect the intensities, but not the positions of the diffracted beams. Because of the periodic arrangement of the atoms, the interference of waves scattered from different atoms may be either constructive or destructive, leading to either systematic absences of reflections, or differences in intensity from one (*hkl*) reflection to another. In the particular case of films grown epitaxialy, the diffraction pattern will exhibit only one family of planes.

X-ray diffraction measurements were performed in a four-circle MRD Philips diffractometer. In this system, the adjustment of four angles allows to define the geometry of the experiment (see Figure 2-3).

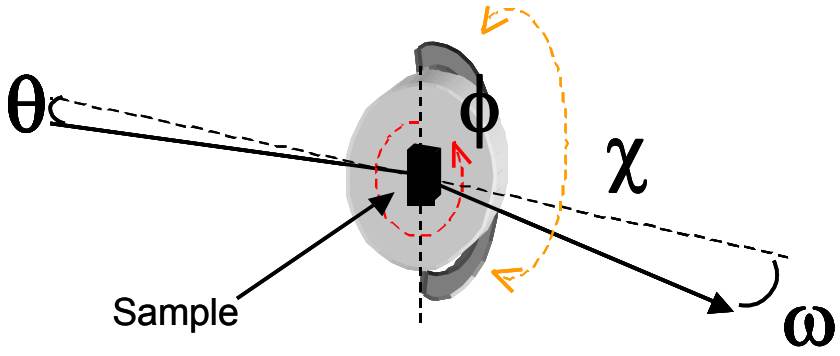

Figure 2-3. Schematic view of the goniometer of the X-ray diffractometer and the four angles: θ, ϕ, χ and ω.

Rotations of these four angles (ϕ, χ, θ and ω) allow setting individual crystals of polycrystalline film at diffraction condition.

Conventional X-ray techniques are described:

- *ω-2θ scans*. The motion of the detector (2θ) and the rotation of the goniometer are coupled. For symmetric reflections, we have $\omega = \theta$. These scans allow studying the film orientation and the out-of plane lattice parameters.

- *Rocking curves (ω-scans)*. The position of the detector is fixed, whereas the ω angle is swept within a given range. The full width at half height characterizes the off-plane misorientation spread of the sample. Samples with larger mosaic spreads show broader rocking curves.

- *ϕ-scans*. These scans are performed for asymmetric reflections. It allows to determine the film epitaxial relationship and the in-plane misorientation spread of the film.

- *Pole figure*. It is used to study the distribution of crystallographic orientations of the sample, or texture. Typically, a crystallographic plane is selected by fixing the 2θ value, and its spatial distribution is analysed by rotating the sample about the χ and ϕ angles.

The conventional X-ray diffraction measurements, ω-2θ scans and rocking curves were performed on a Rigaku Rotaflex RU-200BV located at the ICMAB and ϕ-scans and pole figures on a Philips PW 3710 mrd located at the Serveis Científico-Tècnics of the Universitat de Barcelona.

2.1.5 Critical Current Density Measurements

The critical current densities of YBCO films were determined by using a superconducting quantum interference device (SQUID) magnetometer of the *Quantum Design* Company, with a superconducting coil able to generate up to 7 T, located in ICMAB.

The four-probe method has been applied to determine the critical current density of YBCO films in the presence of and applied magnetic field ($\mu\mathbf{H}$) as a function of the angle θ between the **H** and the *c* axis [35].

CHAPTER 3
CHEMICAL SOLUTION GROWTH OF CeO_2 CAP LAYER FOR YBCO COATED CONDUCTORS

Chapter preview

The CSD (chemical solution deposition) technique is a promising method for the deposition of thin films. CSD growth of CeO_2 buffers on metal tapes has received considerable attention. The close lattice match between CeO_2 and YBCO raises the possibility of its application to coated-conductors. We report in this chapter the essential issues of the growth mechanism of CeO_2 films deposited onto YSZ substrates by CSD. A grain growth inhibition mechanism for CeO_2 films grown by CSD under reducing atmospheric conditions has been identified, which results in nanocrystalline and porous films. Unblocking grain growth via post processing under oxidising conditions or via doping ceria with gadolinium results in a dramatic evolution of the granular structure towards a highly epitaxial film terminated with polar (001) surfaces.

MOD-YBCO films with a high critical current density, $J_c > 1\times106 Acm^{-2}$, have been achieved in the MOD buffers of CeO_2.

3.1 Introduction

Deposition and growth mechanism of CeO_2 onto (001)-oriented YSZ single substrates, as a model system, have been studied in view of the development of coated conductor architectures based on YSZ^{IBAD}/SS and on $La_2Zr_2O_7/Ni^{RABIT}$ by CSD. Specific issues associated with the performance of CeO_2 as buffer layer are mainly: (1) small mismatch in order to guarantee good transmission of texture through the multilayer (mismatch strain with YSZ is ~ - 5%); (2) low surface roughness, which appears intimately related to film granularity; (3) high performance against cation/oxygen diffusion; and (4) keep chemical reactivity with $YBa_2Cu_3O_7$ leading to $BaCeO_3$ [36] to a minimum. In this context, the granular character of the microstructure is important as it may affect, either directly or indirectly, issues (2) to (4). On the other hand, granularity is especially relevant to CSD films owing to specific kinetic and thermodynamic effects [22]. As proposed 36 years ago by Roy [21], the free energy difference between a sol-gel derived amorphous film and the crystalline ceramic phase (that is, the thermodynamic driving force for crystallisation ΔG_{th}), is significantly larger than the corresponding difference between the supercooled liquid and the crystalline phase. Under such large driving forces there is energy in excess to surmount the energy barriers for all nucleation events, and therefore heterogeneous and homogeneous nucleation may occur with similar probability. This particular circumstance results in a strong tendency towards homogeneous nucleation inherent to CSD films. Moreover, since ΔG_{th} increases as the temperature is decreased below the melting point, crystallisation throughout the whole volume of the film starts during heating to the processing temperature. The fact is that, this behaviour, together with reducing atmospheric conditions, will influence the future microstructure of the CSD-derived CeO_2 films, as we will see below.

This chapter is divided in two parts. The first one is devoted to the microstructural and morphological transformations occurring during epitaxial sintering of CeO_2 films. Controlling sintering of the nanocrystalline precursor material may be interesting to tune specific film microstructures. For that purpose we have studied the microstructure evolution of ceria films grown under different atmospheric conditions (sections 3.3 and 3.5) and from different solution precursors (section 3.6). Finally it was studied the effect of trivalent Gadolinium dopant on ceria films (section 3.7).

The second part of the present chapter is devoted to the microstructure study of a CSD-derived YBCO film deposited on a Gd-CeO_2 buffered YSZ substrate. The main features concerning the YBCO nucleation and growth will be considered in the next chapter.

3.2 Experimental procedure

In this section, the sample preparation procedure of ceria and YBCO layers grown by our group will be described. All samples were made in ICMAB [37,38].

3.2.1 Synthesis of ceria films

The first ceria film characterized, referred to as as-grown ceria film, is fabricated from Cerium(III) Acetilacetonate precursors dissolved in acetic acid. This sample was subsequently deposited on (001)-YSZ single crystal substrates by spin coating at 6000 rpm and an acceleration of 3000 rpm/s. The solution's life time was of several hours after which white cerium acetate precipitates were found to nucleate, as determined by NMR analysis. The growth of the films was performed under Ar/5%H_2 at 750 ºC for 4 hr [37].

Films having a thickness comprised in the range of 7-87 nm were produced by controlling the precursor solution concentration (0.0025M-0.9M) in order to determine the residual stress of such films. The thickness of the films varies linearly with concentration within the explored concentration range, thus allowing fine tuning. Furthermore, complete substrate coverage was observed for concentrations ≥ 0.08M [39].

Spanková et al. studied CeO_2/Al_2O_3 films grown by off-axis (rf) sputtering and reported a significant improvement of the crystalline quality of CeO_2 films after a 3 hours anneal at 1000 ºC in air [40]. Prompted by this previous report, standard films were submitted to post annealing at 1000 ºC in either air or oxygen, for 4 hours [39]. Since no significant differences between films post-processed under air and oxygen were found, in what follows no distinction between them is made. The effect of such

high temperature post-processing in oxidizing atmospheres on the microstructure was investagated.

Finally, it was investigated the microstructure of solution-deposition Gd-doped ceria films. Its preparation consisted of the dissolution of a stoichiometric amount of gadolinium pentadionate ($Gd(acac)_3$, 99.9% from Aldrich) in 1 mL of propionic acid and 1 mL of isopropanol (instead of glacial acetic acid, as in the as-grown ceria films). The purpose was to increase the solution's lifetime and improve metal-organic precursor decomposition leading to less carbon *poisoning* of grain boundaries [38]). The solution was stirred and heated (40 ºC) for 20 minutes, followed by the addition of cerium pentadionate ($Ce(acac)_3$, 99.9% from Alfa) and stirred for another 20 minutes at 60 ºC. The total metal concentration of the solution was controlled to be 0.25 M. 15 μl of the Gd-doped CeO_2 precursor solution were deposited on a (100) YSZ single crystal substrate by spin-coating, following the deposition and growth conditions described by modified CeO_2, 8 hr at 900 ºC under Ar/5% H_2 [38].

3.2.2 Synthesis of YBCO

TFA solutions were prepared following a modified procedure [14]. YBCO commercial powder was dissolved in a stoichiometric quantity of trifluoroacetic anhydride and a small quantity of trifluoroacetic acid (used as catalyst) in acetone. The resulting solution was refined by evaporation under vacuum to yield a glassy green residue. This residue was then dissolved in sufficient methanol to give a final anhydrous solution with an ion metal concentration of 1.5 mol/l. The gel films were deposited onto a Gd-CeO_2/YSZ (single crystal) by spin coating.

The high temperature heating profile for high quality YBCO growth on Gd-CeO_2 has been optimized for Gd-CeO_2 cap layer. The growth process consists of three stages of heat treatment which are: first a low temperature calcination, a pyrolysis step, which is carried out under a wet oxygen atmosphere, in order to avoid any sublimation of $Cu(TFA)_2$. This stage favours the burning of the organic content of the precursor. Secondly, a high temperature (770 ºC) firing step for film sintering (50 min wet dwell + 30 min dry dwell). In accordance with the optimized values found elsewhere the following growth parameters were settled: $P(O_2)$ = 0.02 kPa, $P(H_2O)$ = 2,2 kPa, gas

flow rate = 2.03×10^{-2} m/s [38]. Finally, films are oxygenated at 450 ºC under a flow of O_2 for 3.5h to reach the superconducting phase.

A sample was removed from the furnace at 770 ºC in order to investigate the $BaCeO_3$ formation. All the other growth parameters remained constant.

A. Microstructural and morphological transformations occurring during epitaxial sintering of CeO_2 films

3.3 Microstructure of ceria films grown at 750 ºC in Ar/5% H_2

The surface morphology of the as-grown films was studied by AFM analysis. The surface of as-grown films exhibits a granular morphology with rounded grains. An example is shown in Figure 3-1 for a 20 nm thick film grown at 750ºC (rms roughness 3-3.5 nm). No apparent grain size and shape variations were detected by comparison of films with different thickness.

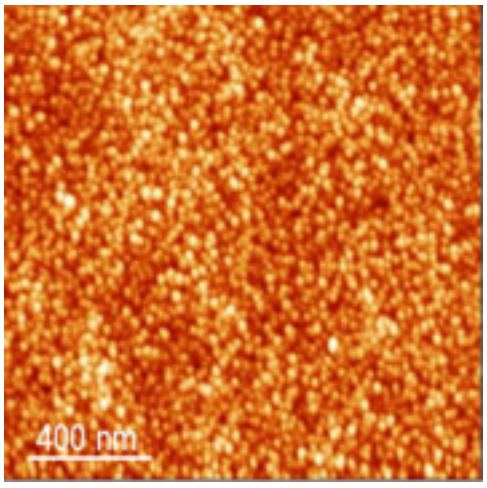

Figure 3-1. Typical AFM image of an as-grown CeO_2 film (750 ºC) exhibiting a granular morphology with rounded grains [37].

Typical XRD $\theta/2\theta$ patterns of as-grown and post-processed CeO_2/YSZ films are shown in Figure 3-2. Only (00*l*) peaks are observed and no secondary phases are detected. ω-scans of films having different thickness yielded FWHM values within 0.2º-0.1º ($\Delta\omega$=0.1º is the value measured for the YSZ single crystal substrate, indicating

that the misorientation spreads of best films are below the resolution of the diffractometer).

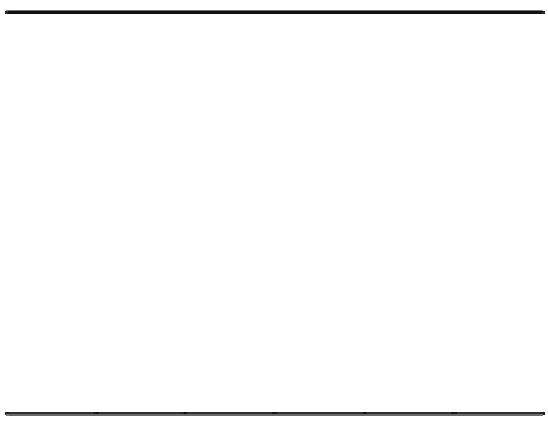

Figure 3-2. $\theta/2\theta$ XRD patterns of an as-grown film and a film post-processed in oxidizing conditions. (Broad features below $2\theta = 30º$, at $2\theta \approx 40º$, and $2\theta \approx 50º$, are instrumental artifacts).

ϕ-scans of the (111) reflection show four peaks 90° apart, thus signaling a unique in-plane orientation (Figure 3-3). It was verified that peak positions coincide with those corresponding to the (111) substrate reflection, indicating that CeO_2 grows on (001)-YSZ with a cube on cube type epitaxial relationship. Off-normal $\theta/2\theta$ scans recorded through the CeO_2 and YSZ (111) reflections at a sample inclination of χ=54.7° clearly indicated that ϕ-scans are free from any substrate contribution.

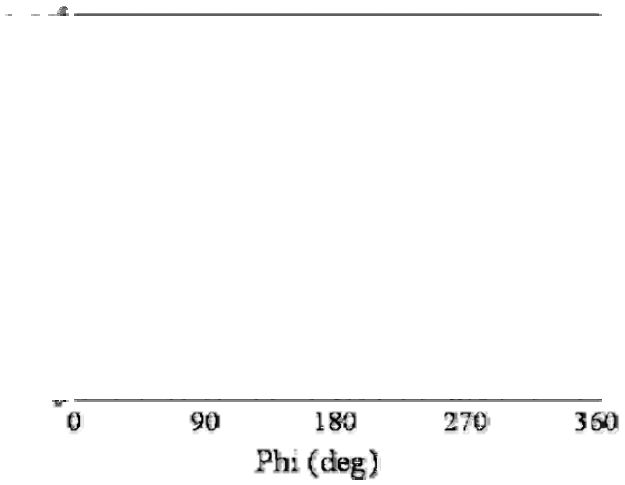

Figure 3-3. ϕ-Scan taken through the (111) reflection corresponding to an as-grown CeO_2 film.

Measuring the FWHM of the peaks we realized that they exhibit an anomalous shape. If usually one can fit the peaks with a Gaussian or Lorentzian curves to get the FWHM, peaks of Figure 3-3 can be fitted with two Gaussian curves. Figure 3-4 (a) shows an enlargement of a ϕ-scan's peak. Careful inspection revealed that the peaks consist of two contributions, one broad peak and a superposed narrow one. Interestingly, it was found that their relative weight is thickness dependent, as illustrated in Figure 3-4 (b). It can be observed that while $\Delta\phi$ values of the narrow and intense peak is kept constant up to a thickness of 41 nm, the corresponding values for the broad peak decrease with increasing thickness. At a thickness of 80 nm, the two contributions merge into one single peak which follows the thickness dependence of the broader peaks of thinner films.

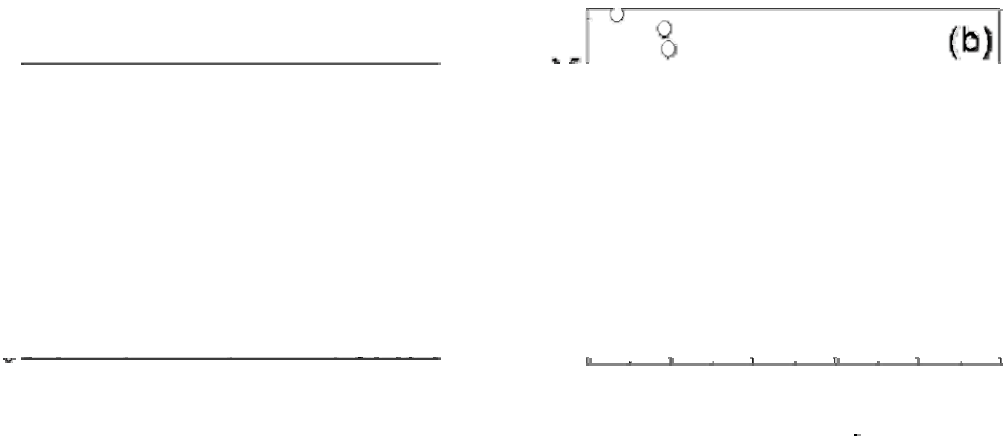

Figure 3-4. (a) Fit of a (111) ϕ-scan peak to two Gaussian contributions depicted as doted lines. Circles correspond to the experimental curve, and the solid curve represents the sum of both contributions. (b) Thickness variation of the narrow and broad components (full and open circles, respectively) of the in-plane misorientation spread determined from least-squares fits to the (111) ϕ-scans.

XTEM observations provided insights into the origin of the bimodal line shapes of ϕ-scans. Figure 3-5 (a) is a high resolution image of the interface. Clearly, the films exhibit a nanometric granular microstructure which contrasts with the columnar one usually reported for films deposited by vacuum techniques [41]. Typically, grains are rounded with sizes comprised between 5 and 20 nm, and no significant through-thickness variations are observed. Careful inspection of Figure 3-5 (a) reveals that only those grains nucleated on the substrate display a strict cube-on-cube orientation, as demonstrated by the Fast Fourier Transform (FFT) pattern taken across the interface, shown as inset. Arrowheads mark the position of heterogeneously nucleated epitaxial grains. However, the texture of the grains nucleated on top of the latter ones will be worsened mostly due to the irregularities found on the surface of the first layer of epitaxial grains, rather than to their misorientation. (See the grain indicated by an arrow, which exhibits (002) lattice fringes inclined to the interface.) Above this layer, grains will find both, a "substrate" exhibiting a finite misorientation spread and an irregular topography. Then, the texture is likely to be rapidly lost from this level to the surface. Figure 3-5 (b) is a high resolution image of the grain structure at the top-most part of the film. Simple inspection of their lattice images reveals that the grains are highly misoriented one to each other.

In order to obtain an average measure of surface disorder RHEED images have been recorded: Figure 3-6 clearly reveals a ring pattern consistent with a randomly

oriented surface, in agreement with high resolution XTEM images (Figure 3-5 (b)). It appears that the films exhibit a pronounced texture gradient, such that the epitaxial orientation of crystallites nucleated on the substrate is gradually lost towards the top of the films, resulting in a randomly oriented surface.

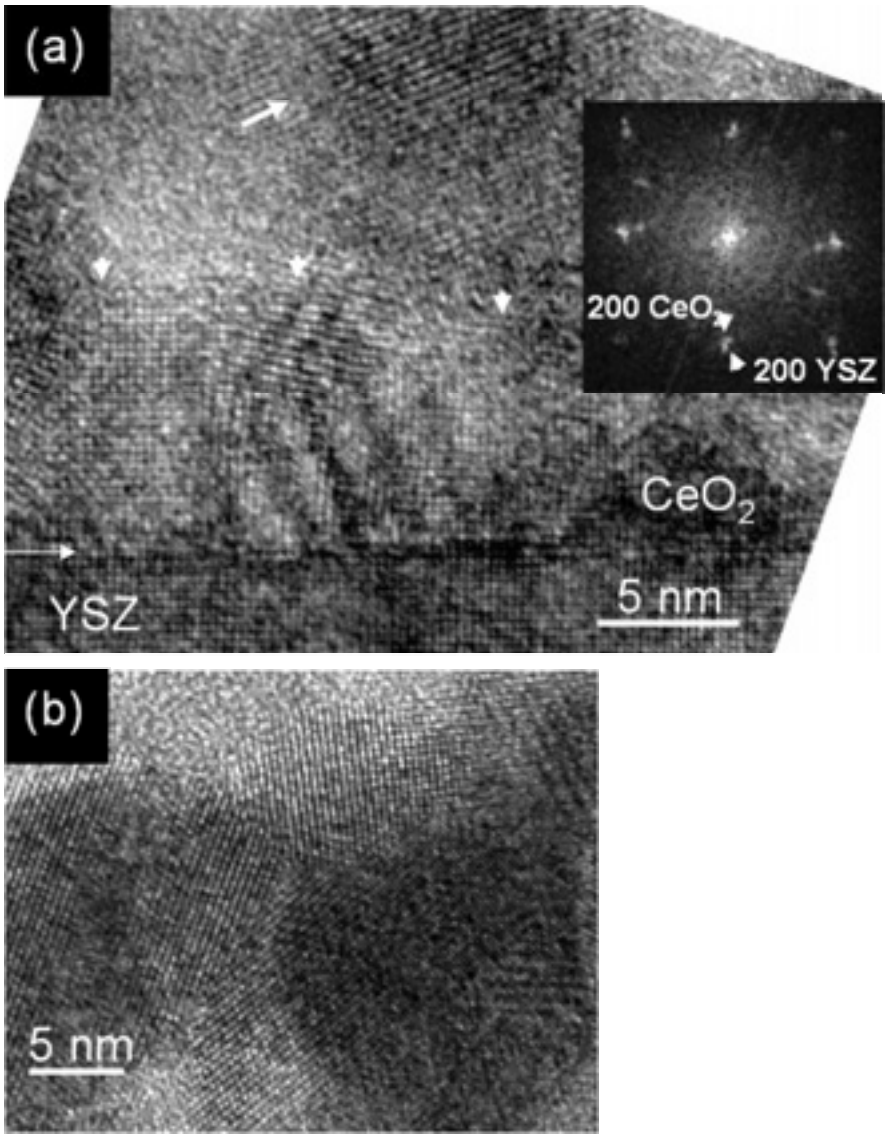

Figure 3-5. (a) High-resolution XTEM image of an as-grown CeO_2/YSZ film viewed along the <100> direction, showing a nanometric granular and porous microstructure. The interface is indicated by a horizontal arrow. Inset shows the FFT spectrum taken across the interface, including CeO_2 crystallites nucleated on the substrate (indicated by arrowheads). (b) High-resolution XTEM image showing a detail of the grain structure at the topmost region of the film.

Hence, the microstructure revealed by XTEM imaging nicely reconciles with ϕ-scan line shapes. The observed bimodal ϕ-scan line shapes can be attributed to the contribution of a well aligned slab of material in contact with the substrate, and a

superposed intensity scattered by the less textured crystallites nucleated on top of it, responsible for the narrow and wide contributions, respectively.

The intensity scattered by the topmost layer of grains is randomly distributed throughout a half-sphere, and will cause a negligible enhancement of the background. Such a microstructure bares witness of a crystallization event occurring under a high undercooling, as expected for CSD [22], in which heterogeneous and homogeneous nucleation have occurred simultaneously. Classical grain growth models of polycrystalline films [19,23], state that those grains having a favored epitaxial orientation grow at the expenses of grains having a less favored one, leading to abnormal or secondary grain growth. Such a behavior has been indeed reported for other CSD systems, where the randomly oriented film is consumed by the advancing growth front of the first epitaxial layer [19]. However, after the 4 h anneal, our microstructure still resembles a snapshot of the nucleated film prior to the growth stage, indicating that some mechanism has inhibited the propagation of the epitaxial growth front through the adjacent nanocrystalline matrix.

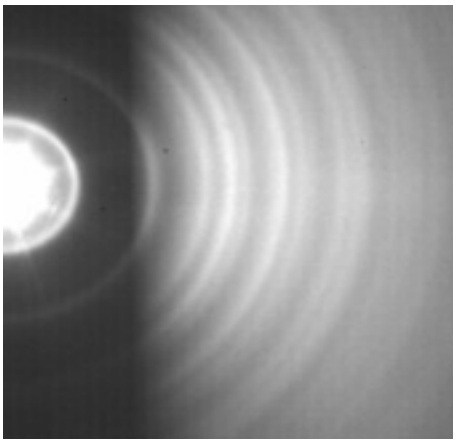

Figure 3-6. RHEED image showing a ring pattern indicating a disordered surface [37].

An electron energy-loss spectroscopy (EELS) map of C distribution in an as-grown sample has been performed. There are two reasons to do that: (a) C represents a major component of precursor solutions and (b) because reducing conditions, otherwise required to protect metallic substrates, is not effective for the elimination of the organic fraction of the precursor solution. Figure 3-7 (a) is an EELS map of C distribution in the as-grown sample, superposed on an image of the microstructure of the mapped area.

The C concentration is proportional to the density of black dots. The image clearly shows that C impurities decorate grain boundaries and porosity.

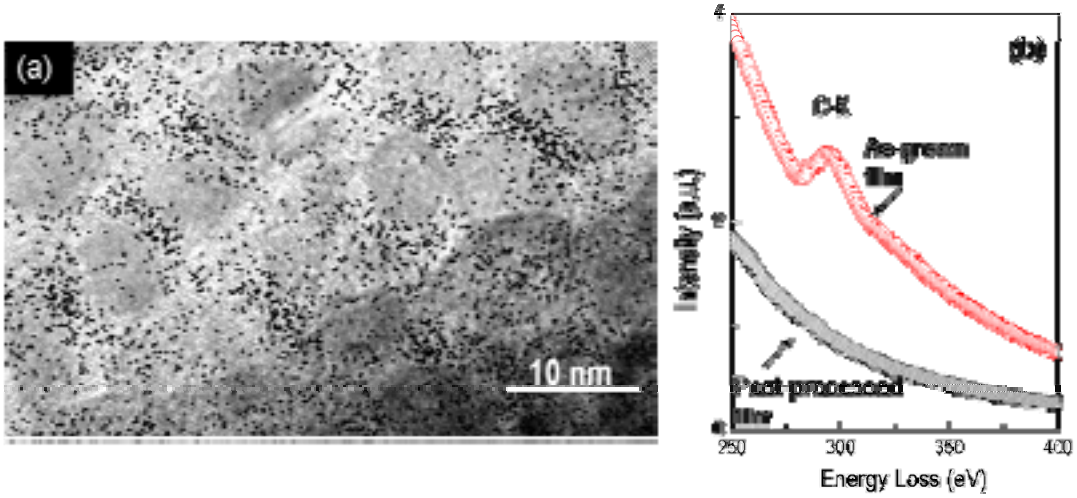

Figure 3-7. (a) EELS mapping of the C distribution trough the cross-sectional area of an as-grown CeO_2/YSZ film, superposed onto an image of the microstructure of the mapped area. (b) Comparison of EELS spectra obtained from as-grown film and post-processed one.

Figure 3-7(b) compares the EELS spectra obtained from an as-grown film and a post-processed one. As expected the carbon K (C-K) peak disappears after annealing under oxidizing atmospheric conditions (this point will be discussed below).

3.4 Residual stress

Diffraction averaged residual stresses were determined using the $\sin^2\psi$ method [33]. According to this model, the slope of a ε versus $\sin^2\psi$ plot is $(1+\nu)\sigma/E$, ε, ν and E being the strain, the Poisson's ratio and the Young's modulus, respectively, and ψ is the inclination of the crystallographic planes from which the lattice parameter is calculated, to the film normal. Values for ν and E are 0.311 and 181 GPa, respectively [42], from which the residual stress, σ, can be extracted. It is important to note that measurements were planed such that only the textured fraction of the films was scanned. The lattice parameter as a function of the inclination to the film normal, a(ψ), was calculated from different reflections according to the cubic symmetry of CeO_2. Between 5 and 10

reflections were used depending on the film thickness (thereof on diffracted intensity). A plot of the residual stress of the films as a function of film thickness, $\sigma(d)$, is presented in Figure 3-8 (a). The σ value corresponding to the thinnest film is affected by a large error as a result of the weak intensities of the reflections used in the calculation. However, the plot shows a clear trend towards decreasing the residual stress as the thickness is increased. The residual stress corresponding to a film submitted to post-processing at 1000ºC in air is also included as an empty square.

Figure 3-8 (b) is an example of strain versus $\sin^2\psi$ corresponding to a 50 nm-thick as-grown film. Having in mind that only the epitaxial fraction of crystallites has been sampled, the significance of the observed decrease of σ with increasing thickness is not straightforward. Theoretical analyses of relaxation in nanocrystalline films show that residual stresses can be effectively relieved by the formation of dislocation walls between nanocrystallites, and suggest a thickness dependence of its relaxation efficiency [43,44]. Tentatively, we can attribute the observed $\sigma(d)$ dependence to an increase of the thickness of epitaxial material with increasing total thickness. In addition, a statistical contribution from the less textured and random fraction of material to the intensity scattered by epitaxial grains must be taken into account. However, this idea is in agreement with the $\Delta\phi$ dependence on film thickness, reported above (Figure 3-4 (b)). The decrease of $\Delta\phi$ with thickness indeed reflects an increase of the oriented or slightly misoriented fraction of grains above the first epitaxial layer, and for 80 nm films, the intensity scattered by this fraction of grains would dominate, thus masking the narrow peak associated to the first layer of strictly epitaxial grains (see Figure 3-4 (a)).

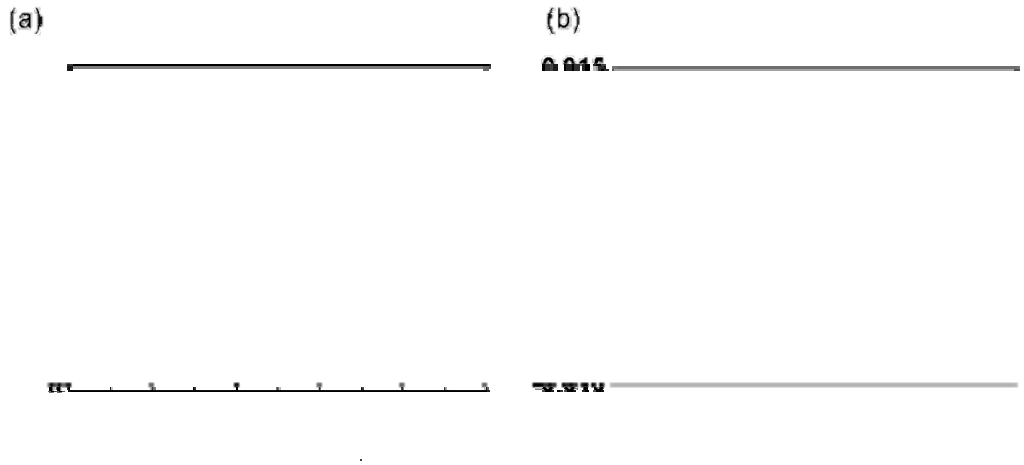

Figure 3-8. (a) Thickness dependence of the residual stress, σ, of an as-grown film. The σ value corresponding to a film submitted to post-processing at 1000 ºC in air is included as an empty square. (b) Strain versus $sin^2\psi$ plot corresponding to a 50 nm-thick as-grown film.

3.5 Effect of high temperature post-processing in oxidizing atmosphere on ceria films

Comparison of XRD $\theta/2\theta$ patterns (Figure 3-2) obtained before and after post-processing reveals as unique but significant difference a clear increase of the intensity of the (00*l*) peaks after annealing at 1000 ºC under oxidizing atmospheric conditions. Accompanying this evidence of increased film crystallinity, XTEM images of post processed films reveal a dramatic microstructural modification. Figure 3-9 (a) and Figure 3-9 (b) are low magnification XTEM images of a film post-processed at 1000ºC. Clearly, the granular microstructure has been evolved to a highly epitaxial crystalline film. It is worth noting that EELS spectra taken on post-processed films did not indicate any evidence of C impurities (see Figure 3-7 (b)). Therefore the microstructural transformation occurs simultaneously with the disappearance of C impurities from the bulk of the films. Figure 3-9 (c) is a characteristic <100> SAD pattern that includes YSZ, demonstrating the cube on cube epitaxial relationship between the whole film and the substrate.

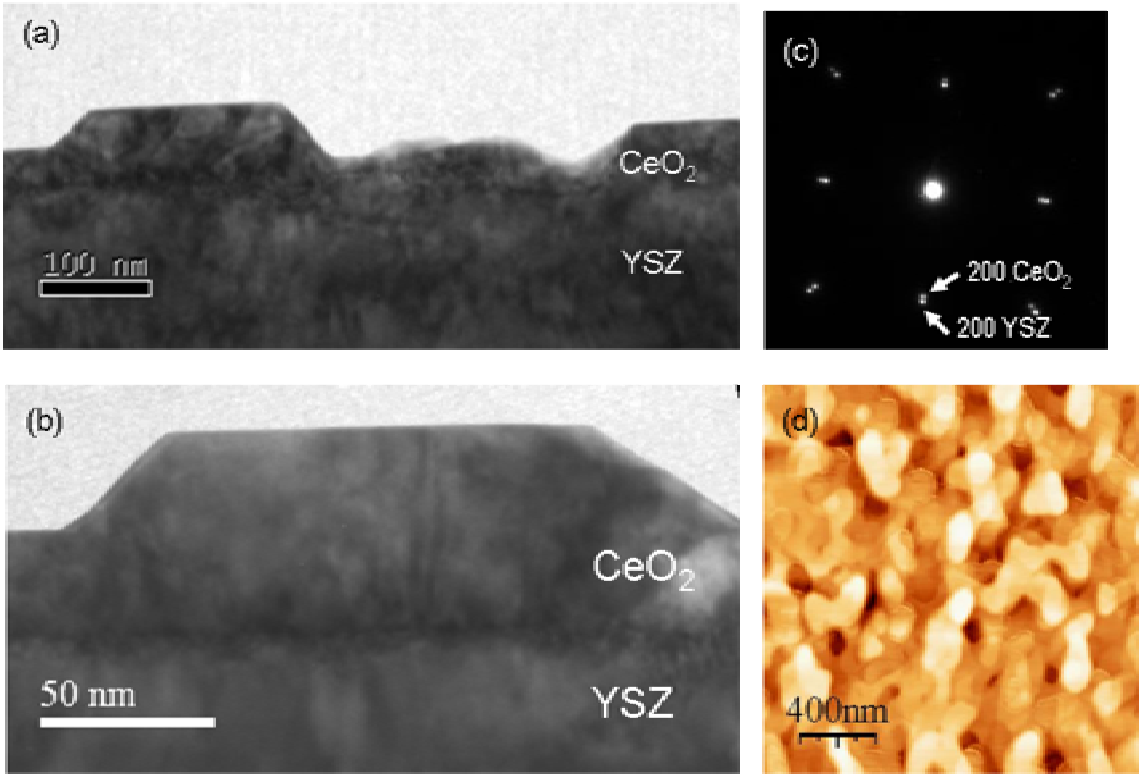

Figure 3-9. (a) and (b) low magnification XTEM images of a CeO_2/YSZ film post-processed at 1000 ºC under oxidizing conditions, viewed along the <100> direction. (c) Corresponding SAD pattern. (d) AFM image exhibiting a terraced surface in agreement with XTEM images.

Furthermore, the images show that at variance with as-grown films, here the surface has developed a terraced topography terminated by polar (001) planes. It has been reported that polar surfaces can be stabilized via substantial reconstruction [45]. In particular, it has been experimentally shown for CeO_2 on $SrTiO_3$, that the (001) planes can be stabilized with ½ monolayer of oxygen terminating the surface [46], i.e., surface polarity can be avoided by surface reconstruction with oxygen. Therefore, in the light of these findings it is not surprising that post processing in oxidizing conditions results in the stabilization of (001) planes of CeO_2. Ledges making an angle of 45º to the film normal are also observed in the XTEM image, which according to the <100> viewing direction may correspond either to the {111} or {011} planes. According to computer simulations {111} and {011} correspond to the first and second most probable crystallographic planes of CeO_2 [47]. Similar faceting has been reported for other CeO_2 films deposited by rf magnetron sputtering [48]. An important result, in view of the application of such films as buffer layers, is that the surface disorder of the films is suppressed by post-processing, as indicated by the ordered array of spots appearing in the RHEED pattern (Figure 3-10). Figure 3-9 (d) is an AFM image exhibiting a terraced

surface in accordance with the XTEM image shown in Figure 3-9 (a) and (b). Despite the surface morphology evolution evidenced in Figure 3-9 (a), (b) and (d), the rms roughness is 3.2 nm, similar to that corresponding to as-grown films. In fact, the AFM image of Figure 3-9(d) evidences a strong tendency towards the formation of facetted hillocks. Such hillocks result from a sintering process involving an intense reorientation and faceting of top most grains in as-grown films.

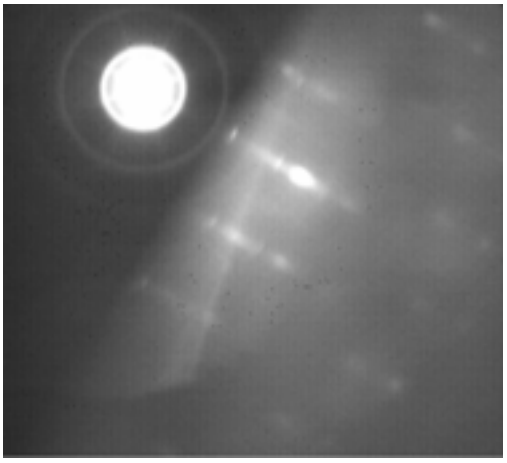

Figure 3-10. RHEED image exhibiting a spot-like pattern indicating an ordered surface [37].

3.5.1 Summing-up

In the introduction we said that the main goal is to grow by CSD a cap layer for YBCO. In this first part we investigated the microstructure of CSD-CeO_2 films deposited from an acetic acid solvent on (001)-oriented YSZ substrates, grown under reducing atmospheric conditions. Then the grain growth behavior was analyzed and correlated with the observed microstructure and surface roughness. Finally, the effects of an oxidizing atmosphere on the microstructure and surface development were addressed.

Crystallization of CeO_2 under the reducing atmospheric conditions of Ar/5%H_2 results in a nanometric granular microstructure with a high concentration of C impurities decorating grain boundaries and interstitial cavities, which unexpectedly prevails after high temperature annealing. Post processing in oxidizing conditions

removes C impurities and promotes grain growth resulting in a fully epitaxial film, as well as stabilizes the otherwise energetically prohibitive polar (001) planes.

Keeping in mind the need to avoid substrate oxidation another way to grow a CeO_2 epitaxial film is required.

3.6 Effect of Gd^{3+} in CeO_2 films grown in Ar/5% H_2

The elimination of grain boundaries in the initial polycrystalline film is the apparent driving force for the epitaxial grain growth. Grain boundaries move as a consequence of many individual atomic jumps across the boundary. Thus, accepting that the impurities in grain boundaries, resulting mainly from precursor chemicals, block the movement of oxygen ions and cations through the grain boundary, it becomes clear that we need to increase the cation and anion diffusion. Chen and coworkers have investigated the effects of dopants on the grain boundary mobility of polycrystalline CeO_2 [49,50]. They asserted that the Gd dopant provides free oxygen vacancies to the host cations thus enhancing the grain boundary mobility.

3.6.1 Types of defects and effect of dopants

When CeO_2 is reduced to CeO_{2-x} defects are formed in the form of Ce^{3+}, which in the Kröger-Vink notation is written as Ce'_{Ce} as the Ce^{3+} has one negative charge compared to the normal lattice. These substitutional negative defects are balanced either by some Ce^{3+} going on interstitial sites as $Ce_i^{\cdots}$ or by oxygen vacancies, $V_O^{\cdot\cdot}$:

Shottky defect $\quad null \xrightarrow{\Delta G_S} V_{Ce}'''' + 2V_O^{\cdot\cdot}$ $\quad$ Eq. 3-1

Frenkel defect $\quad null \xrightarrow{\Delta G_F} V_{Ce}'''' + Ce_i^{\cdots\cdot}$ $\quad$ Eq. 3-2

Kröger-Vink notation

A standard notation used for the description of defects in ceramics materials is the Kröger-Vink notation, in which a defect is described in three parts. The main body of the notation identifies whether the defect is a vacancy "V", or an ion such as "Ce". The subscript denotes the site that the defect occupies, either the normal atom sites of the host lattice or an interstitial site "i". The superscript identifies the effective charge (or relative charge) of the defect relative to the perfect crystal lattice. For this part of the notation, dots (·) represent positive effective charges, dashes (′) represent negative charge, and x's are sometimes used to show neutrality.

Self-diffusion studies in non-stoichiometric CeO_2 shows that the behavior is consistent with the oxygen vacancies model [51,52]. So, it is generally agreed that the main compensating defects in CeO_{2-x} are oxygen vacancies.

Thus, the process of ceria reduction may be written as

$$O_O + 2Ce_{Ce} \rightarrow \frac{1}{2}O_2(gas) + V_O^{\cdot\cdot} + 2Ce_{Ce}^{'} \qquad \text{Eq. 3-3}$$

Within the limits of stability of the oxide (i.e., before decomposition or a transition to a different phase occurs [53]), a large population of charge-compensating V_o (oxygen vacancies) may already exist in undoped CeO_2. This property is the basis of several technological applications of CeO_2, such as catalytic supports (for automotive exhaust) [54,55] and high temperature electrodes [56,57].

Oxide vacancies may also be introduced by doping with oxides of metals with lower valences, e.g. by dissolution of CaO or Gd_2O_3:

$$CaO = Ca_{Ce}^{''} + V_O^{\cdot\cdot} + O_O \qquad \text{Eq. 3-4}$$

$$Gd_2O_3 = 2Gd_{Ce}^{'} + V_O^{\cdot\cdot} + 3O_O \qquad \text{Eq. 3-5}$$

Eq. 3-1 may also take place in doped ceria, and doping will naturally affect the equilibrium of reaction Eq. 3-1 by changing the concentration oxide vacancies and by decreasing the concentration of Ce_{Ce}.

Assuming no interaction between the various defects (which is valid in low concentrations) the law of mass action is valid. Applied on Eq.3-3 this gives:

$$\left[V_{\ddot{O}}\right]\left[Ce'_{Ce}\right]^2 PO_2^{1/2} = \text{constant} \qquad \text{Eq. 3-6}$$

as the concentrations of O_O and Ce_{Ce} are about constant. In the case of undoped ceria $\left[V_{\ddot{O}}\right] = x$ and $\left[Ce'_{Ce}\right] = 2x$. Insertion in Eq. 3-5 and rearrangement gives:

$$x = \text{constant}\, PO_2^{-1/6} \qquad \text{Eq. 3-7}$$

Chen and co-workers proved that the grain boundary mobility in undoped ceria was higher in less oxidizing atmospheres (e.g., 2% O_2) than in more oxidizing ones (e.g., 100% O_2). This implies that an increase in reduced cerium concentration, $[Ce^{3+}]$, or better, in oxygen vacancies concentration, $[V_o]$, also increases grain boundary mobility.

They also studied theoretically the grain boundary mobility of CeO_2 in the intrinsic regime. Considering that cation diffusion is rate-limiting and that it occurs by an interstitial mechanism, they found that the mobility depended on oxygen vacancies concentration [49]:

$$M_{\text{int}rinsic} \propto D^{gb}_{Ce_i}\left[V_{\ddot{O}}\right]^2 \frac{K_F}{K_S}\exp\left[-\frac{\Delta G_F - \Delta G_S}{KT}\right] \propto \left[V_{\ddot{O}}\right]^2 \qquad \text{Eq. 3-8}$$

where $D^{gb}_{Ce_i}$ is the self-diffusivity of Ce_i along a grain boundary. For pure CeO_2, $[V_o^{\cdot\cdot}]$ is determined by redox reaction (Eq. 3-3). Chen et al reported that, among several trivalent cations, the minimum activation energy and highest grain boundary mobility corresponded to Gd-doped CeO_2 [50]. Gd^{3+} is a trivalent cation that increases the oxygen vacancies (Eq. 3-5) and at the same time its ionic radius (1,05 Å) is similar to that of Ce^{3+} (1,07 Å). As it will be shown below, the effect of Gadolinium on grain boundary mobility of CeO_2 depends on dopant concentration and growth conditions.

3.6.2 Structural characterization of CeO_2 films doped with Gadolinium

A wide range of Gd concentration and temperatures have been investigated and the optimal results were obtained with ~10% Gd concentration grown at 900 ºC [38].

Figure 3-11 shows selected surface morphologies to demonstrate their dependence with Gd content and temperature. At low (1%) and at high (20%) Gd concentration AFM images show granular surfaces, Figure 3-11 (a) and (c) respectively, while at 10% Gd AFM image, Figure 3-11 (b), exhibits a terraced surface, similar to the surface morphology exhibited by the sample post processed under oxidizing conditions (see Figure 3-9 (d)). These results appear to follow the trend of Chen and co-workers data, in the sense that at the lowest percentage of Gd concentration (1%) there are not enough oxygen vacancies to enhance cation diffusion and boost the grain growth, while at the highest dopant concentration (20%) the solute drag mechanism suppresses grain boundary mobility, leading to a microstructure characterized by small and misoriented grains in both cases. As in the case of undoped ceria, AFM images of 1% and 20% of Gd-doped ceria support the view of a texture gradient, i.e. a well aligned slab of material in contact with the substrate, and a superposed less textured crystallites nucleated on top of it (see Figure 3-2 and Figure 3-5).

According to the temperature dependence, careful inspection of the AFM image of the sample with 10% Gd grown at 750 ºC, Figure 3-11 (d), shows a granular morphology with differences in grain size. The presence of large grains (up to 200 nm of diameter) suggests that the grain boundary mobility has been enhanced, compared with standard undoped ceria films, but it is still far from the terraced surface seen in Figure 3-11 (b). Wang et al [58] studied the reduction of 10 and 20 % Gd_2O_3 doped CeO_2 over a temperature range from 700 to 1100ºC and they stated that at equal oxygen partial pressure the number of oxygen vacancies increase with temperature. Furthermore, in any material defects increase with temperature, so in undoped CeO_2 at lower temperature it should be a lower concentration of oxygen vacancies [24,59]. The result in all cases is a decrease in grain boundary mobility.

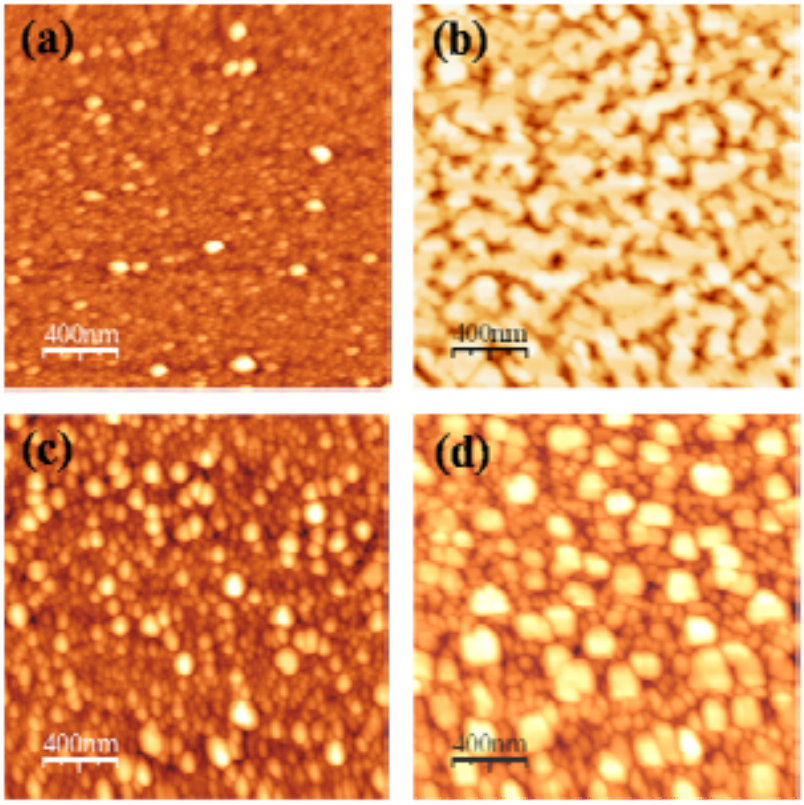

Figure 3-11. AFM images of Gd-doped CeO_2 films grown in Ar/5%H_2: (a) 1% Gd at 900ºC, (b) 10% Gd at 900ºC, (c) 20% Gd at 900ºC and (d) 10% Gd at 750 ºC [38].

It is worth noting that the lowest rms roughness among them belongs to the sample with 10% Gd grown at 900 ºC, Figure 3-11 (b), which exhibits terraced surface and a roughness value of 4.7 nm, while samples with rounded granular surfaces have similar roughness, ~7 nm, Figure 3-11 (a), (c) and (d). As far as the application of CeO_2 films as buffer layers in coated conductor architectures is concerned, the control of their granularity and surface topography becomes essential. Surface roughness affects the quality of the YBCO films. It is well known that the CeO_2-YBCO interphase is prone to react leading to the undesired formation $BaCeO_3$ [36]. Therefore, a higher surface roughness is likely to enhance the interphase reactivity due to the resulting increased interphase area. As it will be seen below, the impossibility of getting lower roughness values leads ceria to react with YBCO.

Comparison of XRD $\theta/2\theta$ patterns obtained from ceria films with 10% of Gd content grown at 750 and 900ºC under reducing atmospheres, shown in Figure 3-12,

exhibits a clear increase of the intensity of the (00*l*) peaks with temperature, thus indicating an increase of the epitaxial fraction of material.

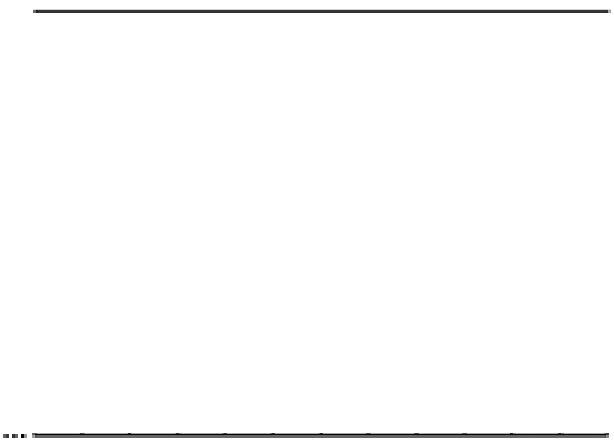

Figure 3-12. $\theta/2\theta$ XRD patterns of 10% Gd-doped ceria films grown at 750 ºC, in red, and at 900ºC, in blue, under reducing atmosphere [38]. (Broad features below 2θ = 30º, at $2\theta \approx$40º, and $2\theta \approx$ 50º, are instrumental artifacts.)

XTEM images of a Gd-doped ceria film grown at 900 ºC confirm such microstructural and morphological modification. Figure 3-13 (a) and (b) is a low magnification XTEM image of a Gd-doped ceria film grown at 900 ºC, viewed along <100>. Figure 3-13 (c) is a characteristic <100> SAD pattern that includes YSZ, demonstrating the cube on cube epitaxial relationship between the whole film and the substrate. XTEM images exhibiting a flat surface are in accordance with the AFM image shown in Figure 3-11 (b). As in the case of post-processed ceria under oxidizing conditions it presents ledges making an angle of 45º to the film normal that may correspond either to the {111} or {011} planes. At the same time the surface has developed a terraced topography terminated by the polar (001) planes, although it does not reach the perfection of the former, being present remnant granularity.

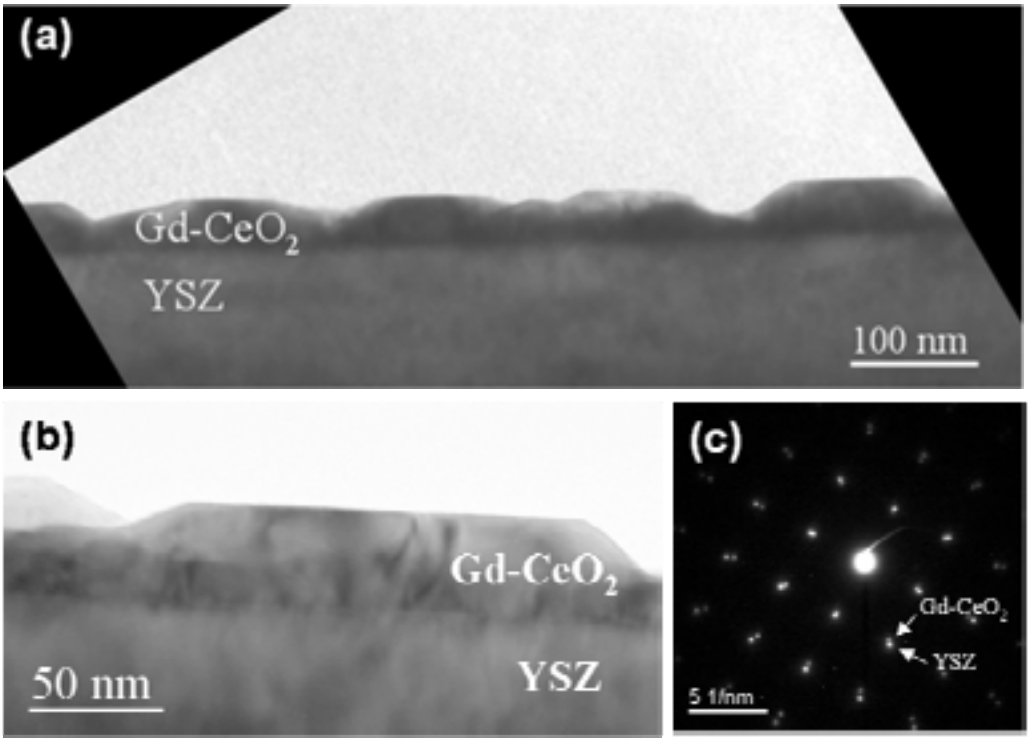

Figure 3-13. (a) and (b) low magnification XTEM images of a Gd-doped CeO_2/YSZ grown at 900 ºC under reducing conditions, viewed along the <100> direction. (c) Corresponding SAD pattern.

The ordered array of spots appearing in the RHEED pattern, Figure 3-14, demonstrates the surface reconstruction, consistent with the TEM images shown above. That is an important result, in view of the application of such films as buffer layers, i.e., the surface disorder of the films is suppressed by the Gd doping.

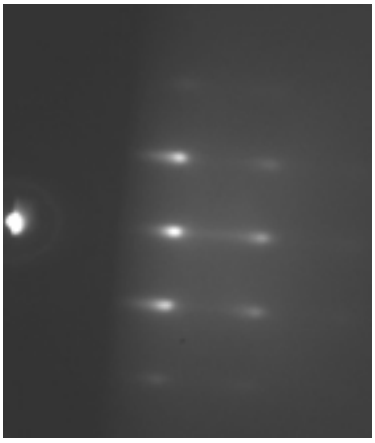

Figure 3-14. RHEED image of a Gd-doped CeO_2/YSZ grown at 900 ºC under reducing conditions exhibiting a spot-like pattern indicating an ordered surface [38].

A closer approximation to the Gd-doped ceria film shows that the film is still partly granular. Figure 3-15, a HRTEM image of the film, shows a misoriented grain embedded into the Gd-CeO_2 film. More misoriented grains were found, with sizes comprised between 10 and 20 nm. Neither of those grains nucleated on the substrate.

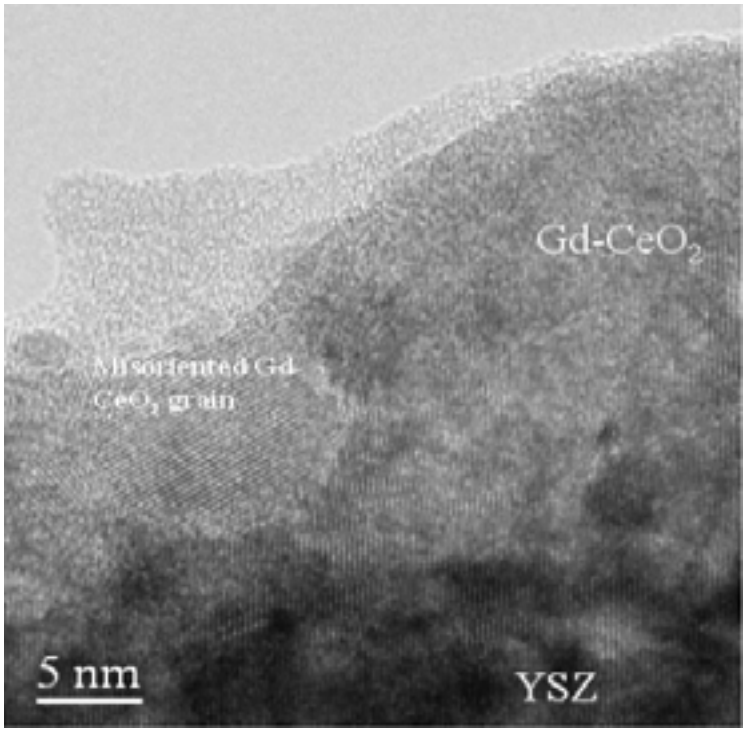

Figure 3-15. High-resolution XTEM image of Gd-doped CeO_2/YSZ film viewed along the <100> direction.

Figure 3-16 (a) shows an impingement of two (00*l*)-oriented grains. This result led us to carry out an EELS analysis of the film, confirming the existence of C at the grain boundary and at the same time its absence in the bulk of the film. Figure 3-16 (b) compares the EELS spectra obtained at different zones, at the grain boundary and at the bulk, exhibiting a prominent C-K peak only in the first zone.

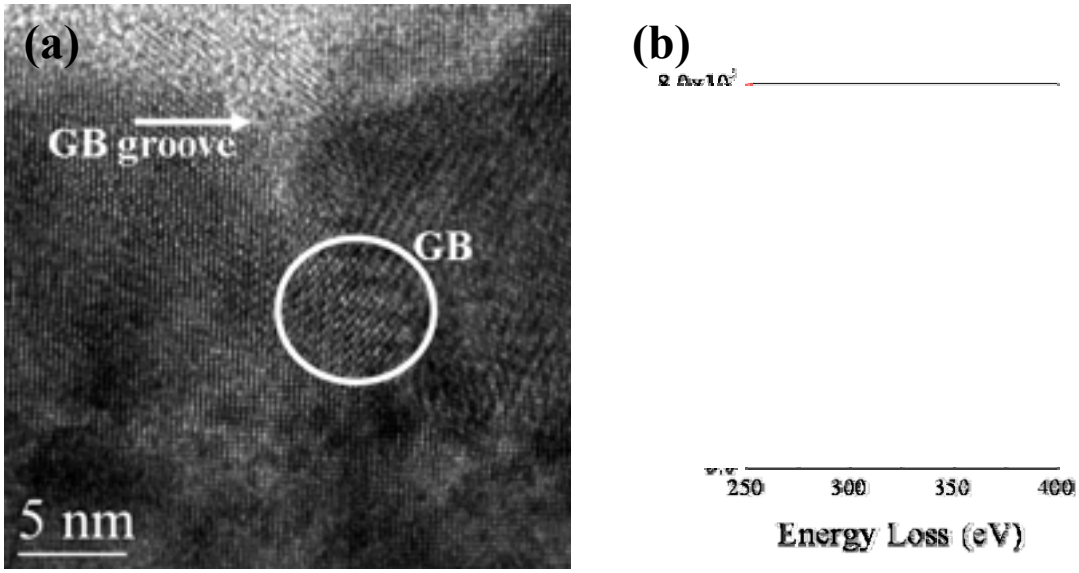

Figure 3-16. (a) High-resolution XTEM image of Gd-doped CeO_2/YSZ film viewed along the <100> direction showing a grain boundary. (b) Comparison of EELS spectra obtained from Gd-doped CeO_2/YSZ film at the grain boundary and in the bulk.

This result shows that the Gd-doped ceria layer growth under reducing atmosphere still contains some C impurities that remain attached to grain boundaries and tend to become concentrated at boundary intersections as grain growth proceeds, as has already been reported by other authors [60,61].

3.7 Conclusions

CSD derived films grow under a large undercooling (recall that CeO_2 melting point is 1600ºC) promoting homogeneous and heterogeneous nucleation simultaneously. Heterogeneously nucleated grains exhibit a cube on cube epitaxial relationship with the substrate, while texture is rapidly lost towards the surface of the films. Such a texture gradient manifests in ϕ-scans by a composite line shape consisting of the superposition of a narrow peak and a wider one associated with the epitaxial grains and the average texture of less-aligned grains lying above the formers, respectively. The residual stress of the textured fraction of nanocrystallites nucleated at the interface is rapidly decreased with increasing total film thickness, suggesting an increase of the thickness of epitaxial material. We showed that films grown in a

reducing Ar/5%H_2 atmosphere are inherently granular as a result of a grain growth inhibition mechanisms induced by grain boundary poisoning with C impurities. Supporting this mechanism, the activation energy for grain boundary motion, Q, determined for these films is significantly higher than that calculated for the growth of CeO_2 nanocrystalline bulk ceramics in a clean environment [39]. In this way, secondary or abnormal growth of epitaxial grains through the porous non-textured nanocrystalline matrix, which would lead to a dense epitaxial film, is impeded. In this granular regime, surface nanocrystallites are randomly oriented, and surface roughness is entirely governed by grain size effects.

The granular regime is suppressed by thermal post-processing at 1000ºC under oxidizing atmospheric conditions. The transformation of the granular microstructure to a dense epitaxial one is accompanied by the elimination of C impurities from the grain boundaries and remnant porosity via oxidation. Upon this volume transformation, the granular surface morphology evolves to a terraced one terminated by (001) planes. In this regime, the surface roughness is governed by the formation of facetted hillocks bounded by {111} and (001) planes. After a 4 h anneal at 1000ºC in static air, rms values are ~ 3 nm.

We have shown that there is another route to generate highly oriented CeO_2 thin films with uniform microstructure, i.e. by doping ceria with Gd. The Gd dopant provides free oxygen vacancies to the host cations thus enhancing the grain boundary mobility. The effect of Gd on grain boundary mobility of CeO_2 depends on the concentration and growth conditions. The optimal result was obtained by ~10% Gd concentration grown at 900 ºC under Ar/5%H_2 atmosphere, it is worthwhile to note that it meets our particular experimental constrain, i.e. to process ceria under reducing atmospheric conditions to avoid undesirable substrate oxidation.

In a pure system, grain boundary migration requires matter transport only over a distance comparable to the interatomic spacing (atomic jumps across the plane of the boundary). However, when impurities that interact with the boundary are present, boundary migration requires either boundary breakaway from impurities or impurities moving along with the migrating boundary. Impurity drag requires matter transport over the same distance as the boundary translation. It is this drag effect that commonly leads to lower boundary mobilities in systems with impurities as compared with the impurity free case.

In particular, in undoped CeO_2 the boundary blocking mechanism is related to the carbon present in the precursor and settling the grain boundaries. The same mechanism acts in doped ceria at high concentration of Gd (20 % in our case), in this case the solute drag also suppresses grain boundary mobility, whereas an optimal content of Gadolinium (10 %) provides charge-compensating oxygen vacancies that enhance grain boundary mobility. So, to induce the desired variations in microstructure one could attack the removal of carbon processing the sample under an oxidizing atmosphere or doping ceria with an optimal content of Gadolinium. But, even when a complete microstructure reconstruction is accomplished, different results, linked to different mass transport diffusivity, also appear. Actually, once the carbon impurities are removed in undoped ceria through a post-processing under an oxidizing atmosphere, the boundary mobility is limited by atom transfer across the boundaries, i.e. intrinsic mobility regime, while in the optimal doped ceria film the rate of boundary migration is determined to a large extent by the diffusivity of the carbon impurities, which is usually slower than intrinsic mobility [24]. This might lead to an accumulation of C in the structural core and/or the vicinity of grain boundaries. Indeed the 10% Gd-doped ceria film is still partly granular, and it still contents C in the grain boundaries. So, our results suggest that to generate (00l)-oriented ceria, the elimination of carbon through a post-processing under an oxidizing atmosphere is more effective than to dope ceria with Gd.

B. Microstructural study of a CSD-derived YBCO film deposited on a Gd-CeO_2 buffered YSZ substrate

3.8 YBCO deposition on Gd-CeO_2

As said before, the *raison d'être* of CeO_2 thin film is the fabrication of YBCO-coated conductors. A thirty-nanometer textured Gd-CeO_2 cap layer has been successfully grown on an YSZ substrate [37,38]. This section focuses on YBCO layer grown on Gd-CeO_2-buffered YSZ substrates as a model system.

The sample studied had a $J_c > 10^6$ A/cm^2 at 77 K. Characterization of the film and its texture was performed using X-ray diffraction. Cross-sectional structure and interface were examined by transmission electron microscopy.

3.8.1 Sample Characterization

The XRD $\theta/2\theta$ scan of the YBCO film grown on Gd-CeO_2/YSZ is shown in Figure 3-17. Only the (00*l*) YBCO reflections were observed. Peaks from the substrate, buffer layer, and reaction product, such as peaks (002) and (004) YSZ and (002) and (004) CeO_2, and peaks of (110) and (002) reflections associated with the reaction product $BaCeO_3$ were also observed. Indeed, the peaks of $BaCeO_3$ are slightly shifted to lower 2θ values, which suggest a solid solution containing Gd. In any case, this phase will be referred to as BCO. No other reflections for YBCO were detected. The reaction between YBCO and CeO_2 yields some excess of Y and Cu, forming secondary phases. Impurity phase reflections (indicated by *) can also be seen, which could be indexed as CuO or $Y_2Cu_2O_5$, being their most intense peaks hidden by BCO and substrate ones. Nevertheless, there is a good nucleation and epigrowth of the YBCO film on Gd-CeO_2 buffered YSZ–single crystal substrate. The out-of-plane and in plane textures of YBCO films were further investigated by ω-scan and ϕ-scan. The FWHM of the (005) ω-scan and (103) ϕ-scan are 0.85º and 1.5º, respectively.

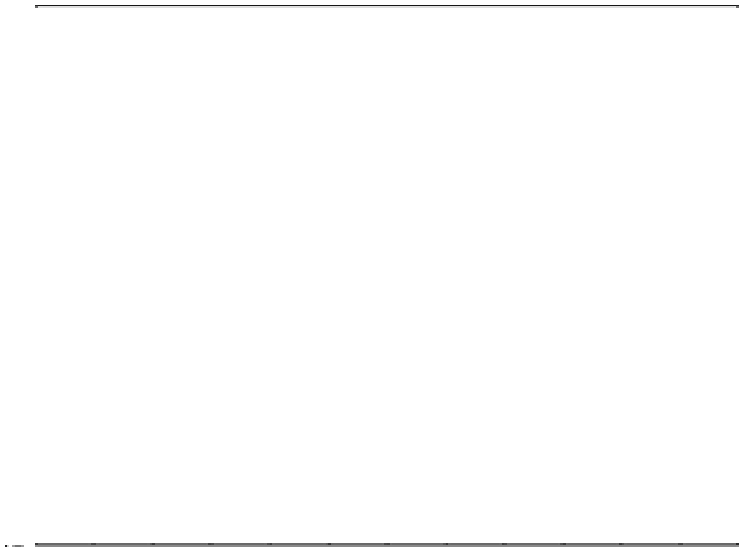

Figure 3-17. X-ray $\theta/2\theta$ reflections of YBCO film on Gd-CeO_2-buffered YSZ substrate. Despite reaction between YBCO and Gd-CeO_2, it reveals a proper c-oriented YBCO layer.

Figure 3-18 is a low magnification XTEM image viewed along the <100> direction showing the interfaces of YBCO/Gd-CeO_2/YSZ. There is clear evidence that the Gd-CeO_2 buffer layer has been replaced by BCO. Despite the presence of BCO at the interface, the XTEM image shows a well-textured YBCO film. BCO resembles a near single crystal exhibiting clean boundaries with the YBCO film and YSZ substrate, with a thickness of ~ 30 nm, just the same thickness that the Gd-CeO_2 film had.

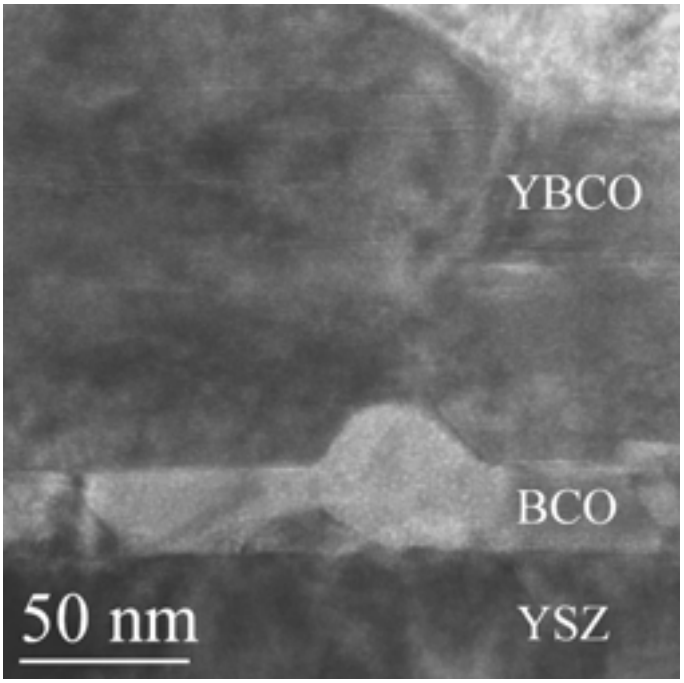

Figure 3-18. Low magnification XTEM image viewed along the <100> direction showing the interfaces of YBCO/GD-CeO_2/YSZ.

Figure 3-19 (a) and (b) shows a SAD pattern along the <110> YBCO direction taken in the vicinity of the interface of YBCO/BCO and a cross-sectional HRTEM image viewed along the <110> YBCO direction, respectively. The epitaxial relation between YBCO and BCO is (1-10) BCO//(00l) YBCO and [110] BCO// [110] YBCO. The SAD pattern, Figure 3-19 (a), shows the substantial mismatch (12%) between both layers. Nevertheless, YBCO film presents no distortion due to the presence of BCO, indeed, it is noticeable the ability of YBCO to adapt itself to BCO, having such large mismatch, which suggest that reaction between YBCO and BCO takes place after the nucleation and growth of YBCO. An HRTEM image, Figure 3-19 (b), make evident the development of a stacking faults array, indicated by arrows, which might be the YBCO mechanism to overcome BCO steps.

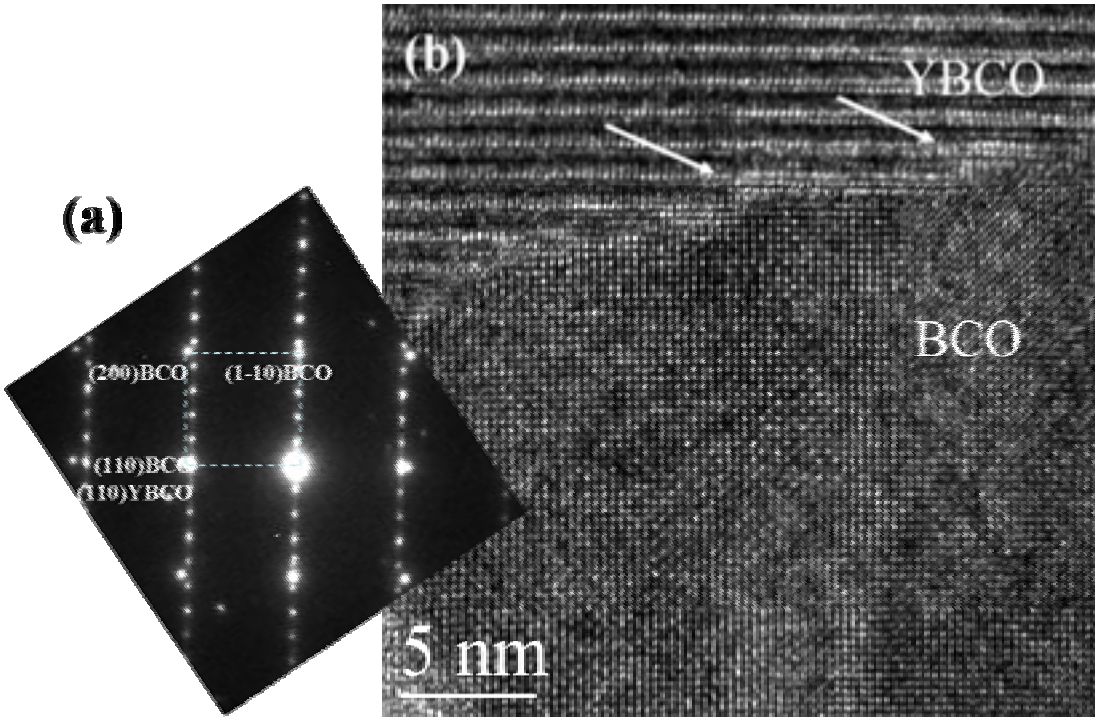

Figure 3-19. (a) SAD pattern showing the discrepancy of lattice parameters between YBCO and BCO. (b) HRTEM image viewed along the <110> direction showing YBCO-BCO interface.

3.8.2 Study of a sample quenched from 770 ºC

Although there are evidences that BCO appears after the YBCO nucleation and growth, a sample quenched from 770 ºC was prepared in order to clarify it. Figure 3-20 is a low magnification XTEM image viewed along the <110> direction of such sample. The image shows a 100 nm-thick YBCO and an almost completely transformed Gd-CeO_2 into BCO. FFT of high resolution images (not shown) revealed that the difference in contrast of the BCO layer is due to (1-10) and (200) orientations (seen before in the $\theta/2\theta$ scan, Figure 3-17).

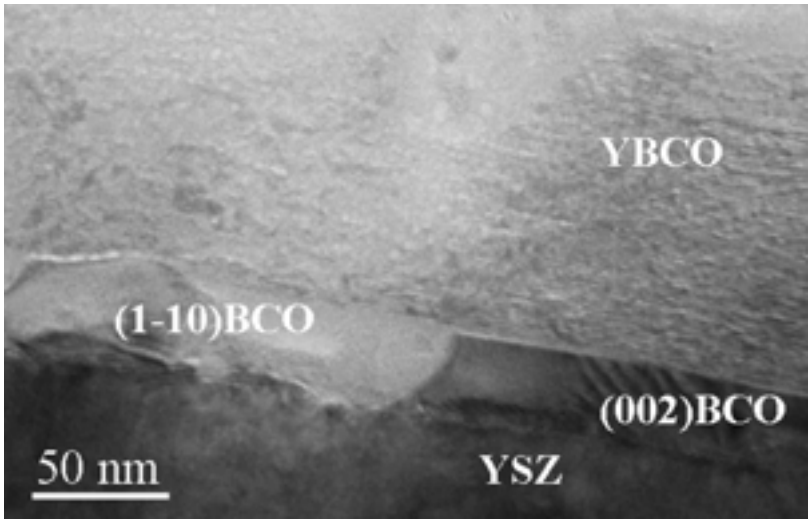

Figure 3-20. Low magnification XTEM image viewed along the <110> direction showing the interfaces of YBCO/BCO/YSZ. YBCO is perfectly c-oriented while BCO exhibits two different orientations.

High resolution images of the interfaces of YBCO/BCO/YSZ reveal that still remain some Gd-CeO_2 grains on the substrate. Figure 3-21 is an example of such HRTEM images where an epitaxial grain of Gd-CeO_2 is embedded into the BCO matrix, having a thickness of ~10 nm.

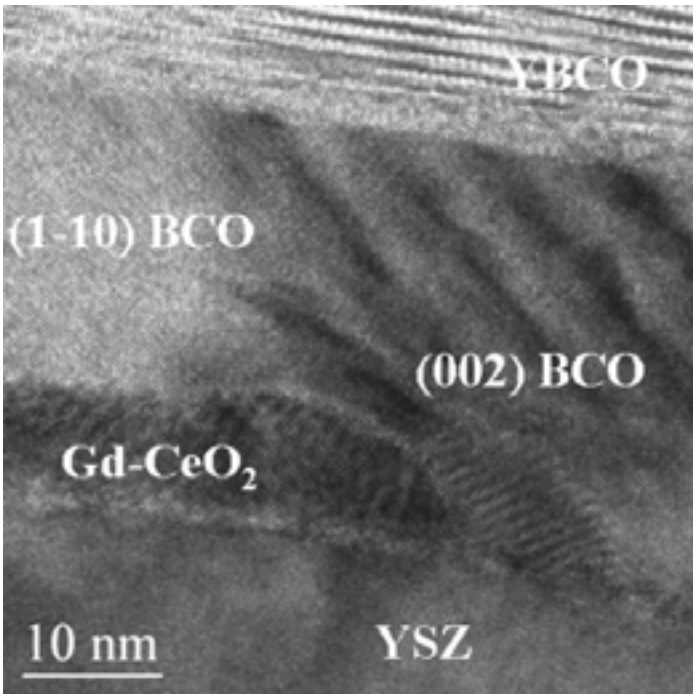

Figure 3-21. HRTEM image viewed along the <110> direction showing the interfaces of YBCO/BCO/YSZ. A Gd-CeO_2 grain on YSZ substrate still remains embedded within the BCO matrix.

3.9 Conclusions

It was observed that MOD-derived CeO_2 under reducing atmospheres promoted the trapping of carbon impurities at the ceria grain boundaries (see Figure 3-7 (a)). These impurities inhibit the ceria (001) epitaxial development, resulting in randomly oriented grains at the surface (seen in Figure 3-5 (b)), preventing any further YBCO epitaxial growth. By doping ceria with 10% Gd ,an almost fully epitaxial layer can be achieved, with the terraced surfaces seen above, Figure 3-13 (a). In spite of the overall roughness of the Gd-doped ceria (~4.7 nm), governed by the formation of facetted hillocks, its terraced surface with atomically flat areas corresponding to (001) planes, provided suitable sites for YBCO nucleation and growth.

Massive transformation of the Gd-ceria buffer to (Gd)$BaCeO_3$ is observed all along the interface without any evidence of YBCO deterioration, which in turn, results not from the reaction between the precursor and Gd-CeO_2 but between YBCO and Gd-CeO_2 during the heating.

A superconducting TFA-derived YBCO film with a J_c (77 K) up to 10^6 A/cm^2 was achieved on top of the MOD-derived Gd-CeO_2 buffer layer.

CHAPTER 4
GROWTH MECHANISM OF TFA-YBCO

Chapter preview

The heteroepitaxial growth of $YBa_2Cu_3O_{7-x}$ (YBCO) films prepared by the trifluoracetate route (MOD-TFA) has been characterized by TEM/EELS and X-Ray diffraction of specimens quenched from various temperatures. We find that the precursor, a nanostructured film, undergoes strong phase segregation during the heating. Our results make evident that the nucleation of YBCO takes place exclusively at the interface with the substrate and is assisted by long range diffusion within a Ba-oxyfluoride matrix rather than interphase reaction among the different phases, resulting in different scenarios for the conversion of the precursor to YBCO.

4.1 Introduction

Growth of YBCO films by metal-organic decomposition (MOD) using trifluoroacetate (TFA) precursors solutions is attracting much interest owing to its great potential for cost-effective production of high performance superconductor tapes. However, although several groups already have reported high critical currents in TFA derived YBCO [62,63], the growth mechanism is not yet understood in detail. Therefore, a fundamental basis for the control and further optimization of the materials properties is still lacking. Growth of films is carried in two steps: The organic precursor is decomposed in a pyrolysis step, yielding a partly amorphous and nanocrystalline mixture which is reacted in a subsequent firing step. Understanding the conversion mechanism to fully reacted YBCO requires detailed knowledge on the reaction path.

In an early work, Gupta et al [20] only recognized broad BaF_2 peaks in $\theta/2\theta$ scans of a pyrolyzed film. This result is in agreement with TEM observations which revealed that at this stage films consist of BaF_2 nanoparticles (10-20 nm) embedded in an amorphous matrix consisting of Cu and Y oxides [64]. More insights into the detailed composition of these films were gathered by ICP analysis and using a fluorine selective electrode [65]. Unexpectedly, this study revealed that the F/Ba ratio follows a wide trajectory, starting at F/Ba = 2.7 in the as-pyrolyzed material, and ending at a value of 1.5 at 700 ºC. This suggest that Y is also present as a fluoride forming solid solution with Ba [65]. Those authors also observed that the concentration of F varies with temperature, which is consistent with phase diagram studies that show that the equilibrium Y content of BYF decreases with temperature [66]. Since the time required for the complete decomposition of the TFA precursor does not depend on the thickness, it was suggested that TFA decomposition takes place throughout the volume of the film and at the interface with equal probability.

Such observations suggest that the reaction path to YBCO may be more complex than the basic approximate reaction [67]:

$$2BaF_2(s) + 2CuO(s) + 1/2Y_2Cu_2O_5(s) + 2H_2O(g) = YBa_2Cu_3O_{6.5}(s) + 4HF(g) \quad \text{Eq. 4-1}$$

in particular regarding the form of Y species. This reaction, Eq. 4-1, involves intermediate steps, such as the reaction $BaF_2 + H_2O = BaO + 2HF$, or the formation of $Y_2Cu_2O_5$, that can be influenced by the topological details of the precursor phase

association. Actually, various forms of the overall reaction have been proposed in the literature, but there is evidence that the reaction path to the final epitaxial YBCO film is, however, complex. The growth rate of YBCO is governed by the synthesis temperature, PH_2O and total pressure [68,69,70], and it has been demonstrated that the careful adjustment of the process parameters is essential to control the microstructure and therefore the critical current of the films [71].

Various studies of quenched samples showed the complex reaction path. Early investigations showed that YBCO nucleates exclusively on the LAO substrate at temperatures comprised between 720 and 770 ºC under 250 ppm O_2. X-ray diffraction $\theta/2\theta$ scans of samples quenched at 720 ºC revealed BaF_2, $BaCuO_2$ and CuO, while at 770ºC, showed the same phase association, with reduced intensity, plus c-oriented YBCO covering the whole substrate interface as indicated by TEM observations [67]. Those authors also identified one phase as inclusion, $Y_2Cu_2O_5$. Samples quenched at 795 ºC did not exhibit significant differences regarding microstructure and phase association, compared with that quenched from 770ºC. The high perfection of the YBCO layer, almost free of grain boundaries, led those authors to suggest the existence of a liquid phase assisting the growth mechanism. Latter, a detailed TEM study of quenched YBCO samples prepared by the co-evaporation technique [72] on STO substrates, showed that a heteroepitaxial (111) oriented fluorite-type (as BaF_2) oxy-fluoride containing Y, Ba, F and O, constitute the preferential nucleation sites, in a way that the fluorite structure is converted to YBCO such that its (111) planes become the (001) ones of the YBCO film. Those authors also observed a ~7 nm thick amorphous layer with a composition similar to that of the YBCO phase, that considered to correspond to a liquid phase at 735 ºC. The occurrence of a liquid phase in the co-evaporation process has been suggested by other authors [73] to occur below 800 ºC, and that its formation is favored by increasing [F]. The occurrence of a liquid phase suggested by the above authors is supported by phase equilibrium studies in the system Ba,Y,Cu,O,F [74] which demonstrated melting at ~600 ºC for F rich compositions at low PO_2.

Further insights into the phase evolution prior to the growth of YBCO were provided by Yoshizumi et al [65], signaling that at 400ºC the [F]/[Ba] ratio is 2.7 and decreases with temperature. This result, along with the observation that the lattice parameter of the fluoride phase, nominally BaF_2, varies with temperature between 5.92 Å at 400 ºC and 6.2 Å at 550 ºC (6.2 Å is the lattice parameter of the BaF_2 fluorite), led

those authors to conclude that at low temperature the fluoride phase consists of a solid solution $(Y,Ba)F_x$, that becomes enriched in Ba as the temperature is increased until the pure BaF_2 phase is achieved at ~550 ºC. The observed behavior is in agreement with phase equilibrium studies in the $BaF_2 - YF_3$ system [66]. Therefore, in a first stage the $(Ba,Y)F_x$ solid solution would decompose into BaF_2, Y_2O_3 and Y(OH), before the formation of BaO.

Turning back to the growth rate of the YBCO film, it has been reported that the growth rate does not depend on the thickness of the film [69]. Therefore the elimination of HF gas through the surface of the film is the rate limiting factor, rather than the diffusion of H_2O and HF through the growing film. Such behavior is supported by the observation that the growth rate is proportional to $PH_2O^{1/2}$, which under local equilibrium, according to reaction (1), varies with PHF. Alternatively, it has been proposed that the growth rate is limited by the mass transfer through a stagnant gaseous layer located on top of the precursor surface [75]. As a microstructural consequence of this thermodynamic behaviour, it appears that partially reacted films may exhibit marked variations of the extent of the conversion process with the position on the substrate. Furthermore, given the complexity of the precursor evolution, presumably there is not a unique microstructural scenario for the nucleation and growth of YBCO, in contrast with views provided by previous reports on transmission electron microscopy studies of partially reacted samples. With the aim to provide an overall appreciation of the conversion process, the present chapter addresses both the pahse evolution within the precursor, prior the YBCO nucleation, and the nucleation mechanism of YBCO.

4.2 Experimental procedure

TFA solutions were prepared following the procedure presented in the chapter 3. YBCO commercial powder was dissolved in a stoichiometric quantity of trifluoroacetic anhydride and a small quantity of trifluoroacetic acid (used as catalyst) in acetone. The resulting solution was refined by evaporation under vacuum to yield a glassy green residue. This residue was then dissolved in sufficient methanol to give a final anhydrous solution with an ion metal concentration of 1.5 mol/l. The gel films were deposited onto 5x5 mm (00l)-oriented $LaAlO_3$ (LAO) single-crystal substrates by spin coating.

Substrates were cleaned in successive ultrasonic baths in acetone and methyl alcohol, followed by a final drying step in pure N_2 gas. Spin coating was performed at approximately 6000 rpm for 2 min using an acceleration time of 1 second. The coating was performed at ambient temperature in the range of 20-22 ºC and relative humidity in the range of 19-24 %. The atmosphere was controlled in order to minimize as much as possible water contamination.

The standard growth process consists in three stages of heat treatment which are: first a low temperature calcinations, a pyrolysis step, which is carried out under a wet oxygen atmosphere, in order to avoid any sublimation of $Cu(TFA)_2$. This stage favours the burning of the organic content of the precursor. Secondly, a high temperature (795 ºC) firing step in an atmospheric mixture of N_2, O_2 (0.02 kPa) and H_2O (P_{H2O} = 0.6 kPa) under a gas flow of $2.03 \cdot 10^{-2}$ m/s to form the $YBa_2Cu_3O_{7-x}$ phase. Finally, films are oxygenated at 450 ºC under a flow of O_2 for 3.5h to reach the superconducting phase, Figure 4-1.

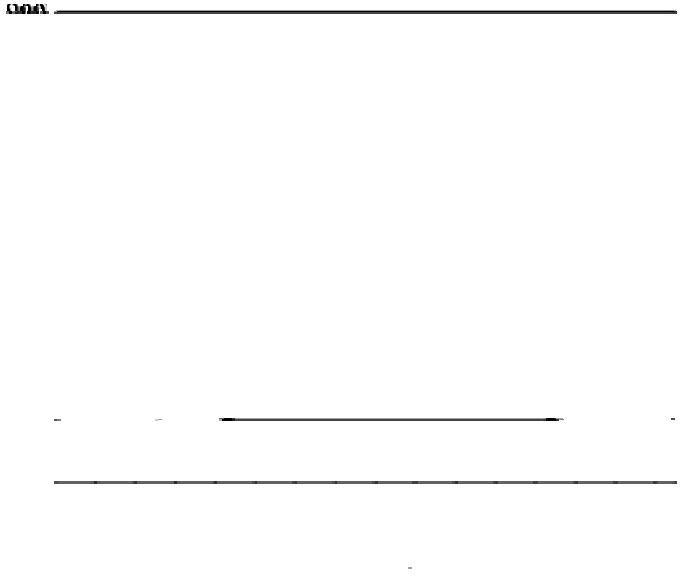

Figure 4-1. Scheme of the ramp of firing step of the growth process.

Pyrolyzed films were placed in a furnace and quenched immediately after reaching the target temperatures. XRD analysis was performed on precursor and quenched samples to obtain information on the phase content of the films and to characterize their texture of the films.

4.3 Phase evolution in the precursor film

Figure 4-2 shows a series of θ-2θ scans of precursor films quenched from different temperatures. After the pyrolysis, the patterns exhibit only broad features, consistent with the nanocrystalline nature of the films, which were identified as $Ba_{1-x}Y_xF_{2+x}$ (BYF) [66] and CuO. The present data does not allow to univocally ruling out the presence of Y_2O_3. The most intense reflection of Y_2O_3, the (222) one, appears around 2θ~29º, and therefore would be masked by the (002) BYF reflection. Since Y_2O_3 is an active Raman compound, the samples were further characterized using μ-Raman spectroscopy [76]. No signatures of Y_2O_3 were found in the pyrolyzed films, thus suggesting that after the pyrolysis, at least a large fraction of the Y content in the precursor film is integrated in the BYF solid solution. The extension of this solid solution is limited, being x = 0.35 the Y richest composition compatible with the fluorite structure [66]. This composition corresponds to a Y/Ba atomic ratio of 0.54, close to that introduced in the precursor solution. Therefore, from a thermodynamic standpoint, the BYF solid solution can accommodate the initial Y/Ba ratio. The BYF lattice parameter, estimated from θ-2θ scans is 6.04 Å, corresponding to x = 0.28, i.e., Y/Ba=0.38 and according to the nominal stoichiometry, F/Ba=2.4 in reasonable good agreement with the value 2.7 estimated by Yoshizumi et al from selective electrode measurements [65]. In the estimation of the Y concentration in the BYF solid solution, we have neglected the influence of oxygen on the lattice parameters. Owing, on the one hand, to the similarity between the ionic radius of oxygen and fluorine anions in a tetrahedral environment (0.124 nm and 0.117 nm, respectively [77]), and the dissimilarity between those corresponding to Ba^{2+} and Y^{3+} in octahedral coordination (0.149 nm and 0.104 nm, respectively [77]), a partial substitution of F by O should have, to a first approximation, only little influence on the variation of the lattice constants.

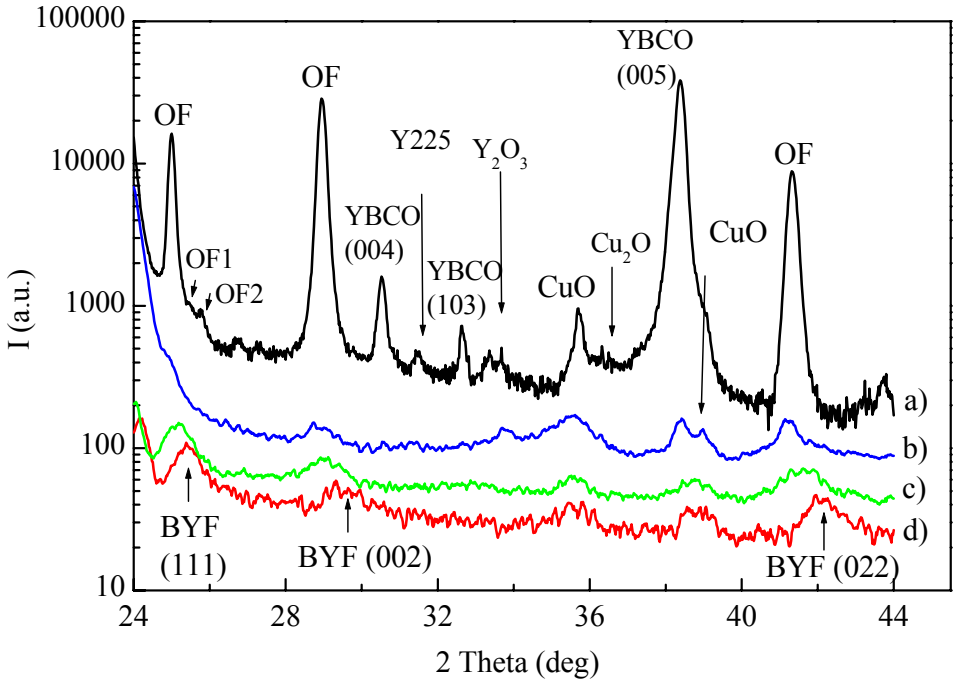

Figure 4-2. X-Ray diffraction patterns of films a) quenched from 795 ºC, b) quenched from 700 ºC, c) quenched from 600 ºC and d) as-pyrolyzed. Y225, OF and BYF stand for $Y_2Cu_2O_5$, oxyfluoride and $Ba_{1-x}Y_xF_{2+x}$, respectively. OF1 corresponds to the (030) reflection of the ordered oxyfluoride, and OF2 is associated with a Y enriched BYF solid solution found around growing YBCO islands (see the text).

Therefore, although most of the Y present in the pyrolyzed film is contained in the BYF solid solution, some amount of free Y_2O_3 may be present, which probably remains silent to XRD and μ-Raman spectra due to its nanocrystalline or even amorphous nature [76]. Samples quenched from 795 ºC exhibit sharp (00*l*) YBCO reflections (in addition to the (103) one, indicative of a small fraction of disoriented YBCO), as well as unreacted BaF_2, BYF, $Y_2Cu_2O_5$, Y_2O_3 and CuO (Figure 4-2). The origin of the two peaks appearing at 2θ~25.5º and ~25.8º (indicated by OF1 and OF2), is discussed below.

Figure 4-3 (a) is a low magnification XTEM image, corresponding to a pyrolyzed 800 nm thick film. The speckled contrast is due to CuO nanoparticles, shown at a higher magnification in the inset. Figure 4-3 (b) shows the corresponding selected-area electron diffraction pattern, which in agreement with the analysis of θ-2θ scans reported in the preceding paragraph, can be indexed with the BYF and CuO phases.

In agreement with phase diagram studies [66], Figure 4-2 shows that increasing the temperature the Y content of the BYF solid solution decreases. Simultaneously, the intensity corresponding to BaF_2 and Y_2O_3 increases, while part of that Y_2O_3 eventually reacts with CuO yielding $Y_2Cu_2O_5$. EELS analyses of a sample quenched from 795ºC, indicate that the fluoride phase contains oxygen, while the peak corresponding to F is systematically very weak (Figure 4-4). However, as reported by other authors [67], the F peak is weakened as a result of F loss during e-beam irradiation in the microscope and therefore intensity ratios cannot be used to quantify the degree of oxidation. At higher energy losses, the EELS spectrum also exhibits weak signatures of remnant Y (see inset). In the following this phase will be referred to as oxyfluoride (OF), while acronym BYF will be used for the $Ba_{1-x}Y_xF_{2+x}$ solid solution regardless its degree of oxidation.

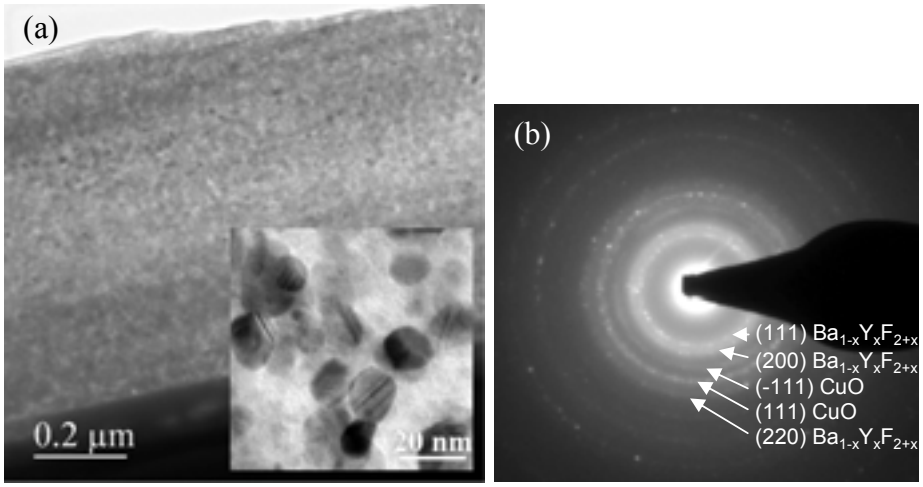

Figure 4-3. (a) Low-magnification XTEM image of an as-pyrolyzed film. The precursor forms a homogeneous, 800 nm-thick film, nanostructured and partially amorphous fluoride matrix of composition $Ba_{1-x}Y_xF_{2+x}$ (see the text), with embedded CuO nanoparticles. Inset is a higher magnification XTEM image to illustrate the size and shape of the CuO particles. (b) Corresponding selected-area diffraction pattern.

The observed phase evolution agrees with the trajectory of the F/Ba ratio previous to YBCO nucleation, reported by Yoshizumi et al [65]. According to these authors, the F/Ba ratio evolves from 2.7 at 350 ºC to 1.5 at 700 ºC, F/Ba=2 (corresponding to BaF_2) being achieved at 550 ºC. For F/Ba > 2, this behavior is explained by the formation of the BYF solid solution and the temperature dependence of the Y solid solubility in BaF_2. In order to explain the trajectory between ratios 1.7

and 2, Yoshizumi at al suggest the expected reaction $BaF_2+H_2O \rightarrow BaO+2HF(g)$. Strikingly, however, in agreement with previous reports by other authors [67,78,72], we have not detected significant fingerprints of BaO. Though this is attributed by Yoshizumi et al. to an hypothetical nanocrystalline or amorphous nature of the BaO phase, the lack of any TEM evidence for the occurrence of BaO, together with the abundance of the OF phase, strongly points that the reaction $BaF_2+H_2O \rightarrow BaO+2HF(g)$ does not occur to a significant extent during the conversion to YBCO, in contrast with that originally expected. These considerations are, moreover, in agreement with the diffusive topotactic character of the YBCO conversion mechanism, where YBCO is formed as a result of the insertion and replacement of chemical species in the fluorite structure, resulting in a severe structural modification, as opposed to the simpler chemical reaction between grains in direct physical contact. Therefore, the drop of the F/Ba ratio below 2 is to be associated with the replacement of F by O in the fluorite structure, in agreement with the strong oxygen signal appearing in the EELS spectrum Figure 4-4.

Figure 4-4. EELS spectrum obtained from the oxyfluoride (OF) matrix in a sample quenched from 795 ºC. Inset shows a higher energy region to check the occurrence of Y.

The behavior discussed in the preceding paragraph emphasizes the role played by the fluorite-type matrix (either fluoride or oxyfluoride) as a solvent, i.e., its ability to accommodate important compositional variations. It has been reported that the melting point (T_m) of the fluoride phase is strongly sensitive to the Y and O content. In particular, T_m drops down within the 500 ºC – 600 ºC range in the BaF_2-CuO-Y(O,F)

region, corresponding to F/Ba > 2 [79,74,80]. This observation has led to argue that the growth of YBCO is assisted by the formation of a partial melt. However, as discussed above, low melting point F/Ba > 2 compositions would appear below ~550 ºC, and there is no evidence that the experimental temperature profile crosses T_m at any stage. The unique microstructural feature that would support partial melting is the occurrence of an amorphous layer, a few nanometers thick and composition similar to YBCO, at the precursor – YBCO interface [72]. Indeed, melting at the growth front might result from the development of concentration gradients favoring low melting point compositions ahead of the growth front, but such an amorphous layer has not been detected in the present investigation and has only occasionally been reported in the literature. On the other hand, as far as the bulk OF matrix is concerned, see Figure 4-5 (a) and (b), it is interesting to note that its nanostructured character is deduced from extended occurrence of Moiré contrasts, indicative of the superposition of nanometric structurally coherent domains, and lattice contrast variations, rather than the identification of grain boundaries in high resolution XTEM images. Most strikingly, the orientation of the "apparent crystallites" building such nanostructured framework is kept unchanged through several tens, even a few hundred, nanometers, thus suggesting that XTEM images in fact constitute snapshots of a rapidly varying microstructure evolved from an epitaxial configuration. The resulting mosaicity is then likely to result from the accommodation of internal stresses associated with the chemical modifications induced first, by the intrinsic phase stability behavior of the BYF solid solution and secondly by diffusive processes assisting the YBCO conversion. Note that a partial melting would at least induce amorphization at grain boundaries of such a mosaic substructure, thus emphasizing the subboundary network, which is not observed. Therefore, though very likely the OF precursor is submitted at temperatures close to T_m, thus enhancing diffusive processes, no definitive traces of partial melting have been found in the present study.

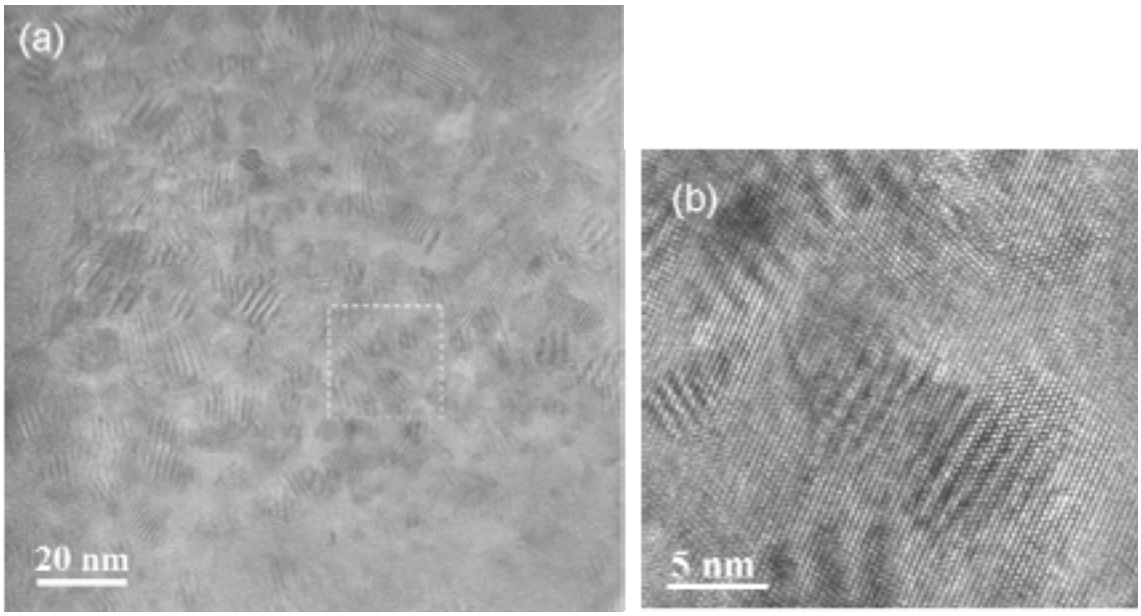

Figure 4-5. (a) High resolution XTEM image of the OF matrix quenched from 795ºC showing a significant variation of the degree of crystallization and (b) magnification of squared zone of the OF matrix.

4.4 Segregation of phases

Elemental distribution maps of films quenched from different temperatures were obtained by x-ray energy-dispersive analysis using a STEM imaging mode. Spatial cation distributions reveal that the complex phase evolution discussed in the preceding section is accompanied by a strong cationic segregation. Figure 4-6 (a), (b) and (c) show the cross-section Y, Ba and Cu maps corresponding to samples quenched from 600ºC, 700ºC and 795ºC, respectively. It can be observed that Cu develops a concentration gradient perpendicular to the interface, exhibiting higher values towards the upper part of the film, while Y and Ba show an inverse trend. As the temperature is raised, the overall cation distribution is progressively homogenized, though short scale heterogeneities appear at 700ºC as result of grain growth (Figure 4-6 (b)). In fact, at 700 ºC first fingerprints of YBCO (00*l*) reflections appear in XRD patterns (Figure 4-2). Such heterogeneities grow in size up to ~200nm when the temperature reaches 795ºC (Figure 4-6 (c)). A striking feature of Figure 4-6 (c) is the close correspondence between the Cu and Y maps. Such a striking correspondence, along with the absence of Ba in the Y-Cu rich areas, points to the formation of Y225 within the OF matrix. Significantly, in this area, mappings do no show any evidence of YBCO formation,

which suggests the existence of a thermal window within which the nucleation of Y225 and YBCO are competitive processes.

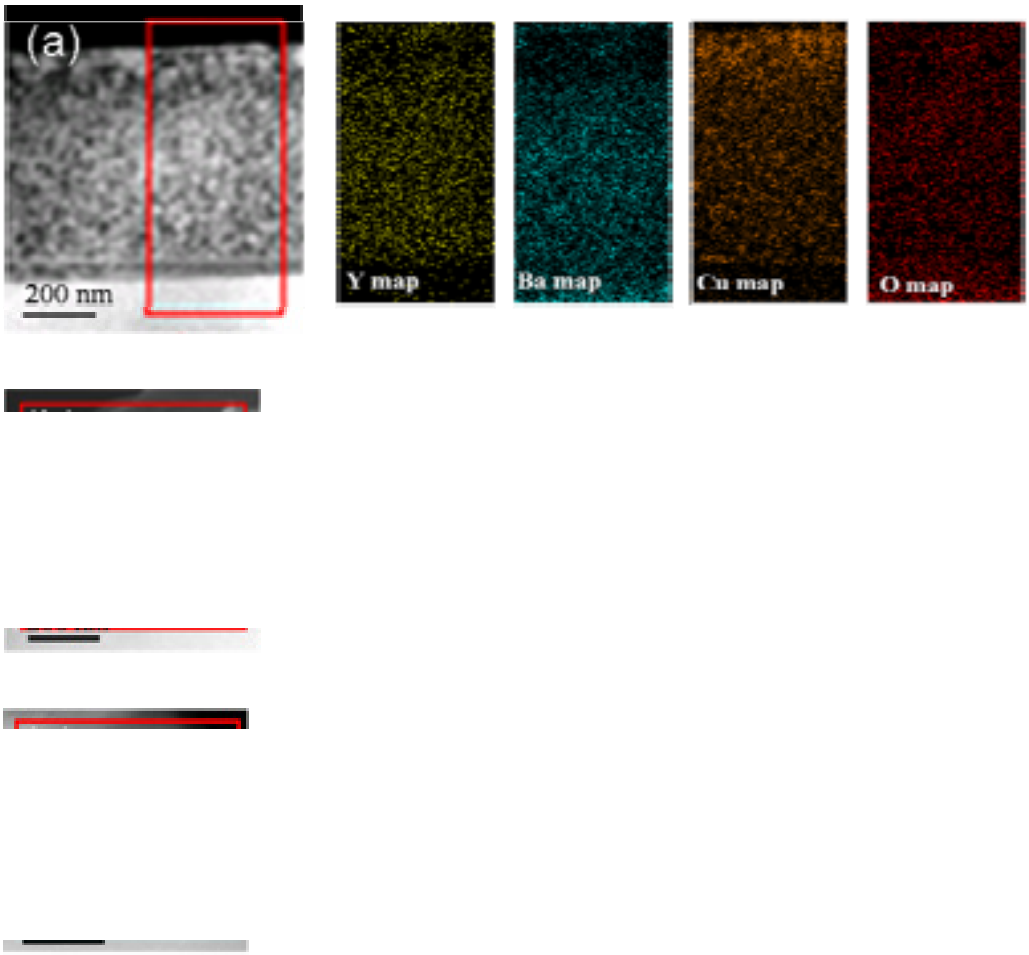

Figure 4-6. Cross sectional STEM EDAX Cu, Ba, Y and O elemental maps of samples quenched from 600ºC (a), 700ºC (b) and 795ºC (c).

Figure 4-7 is a low-magnification XTEM image of the film quenched from 795ºC, viewed along the [100]LAO direction. In order to get a rough view of the distribution of phases, results of EELS analyses performed at some points of the cross section, are indicated in the image. In agreement with EDX mapping, Figure 4-7 reveals phase segregation while the vertical Cu gradient has disappeared. As reported by other authors, YBCO islands are shown to nucleate exclusively on the substrate surface, preferentially with their c-axis perpendicular to it. An a-axis-oriented YBCO nucleated on top of a c-oriented island grain reaching the film surface, can also be observed. The film exhibits at this stage of the growth process, approximately half of the precursor film thickness, i.e. 450 nm, while after the complete process the film thickness will

further reduce down to 300 nm. Therefore, such a-axis grains will outcrop on the flat c-axis oriented surface. Overall, the image reveals that at 795 ºC the OF phase constitutes a homogeneous matrix containing, Y225, CuO and Y_2O_3 grains, besides YBCO.

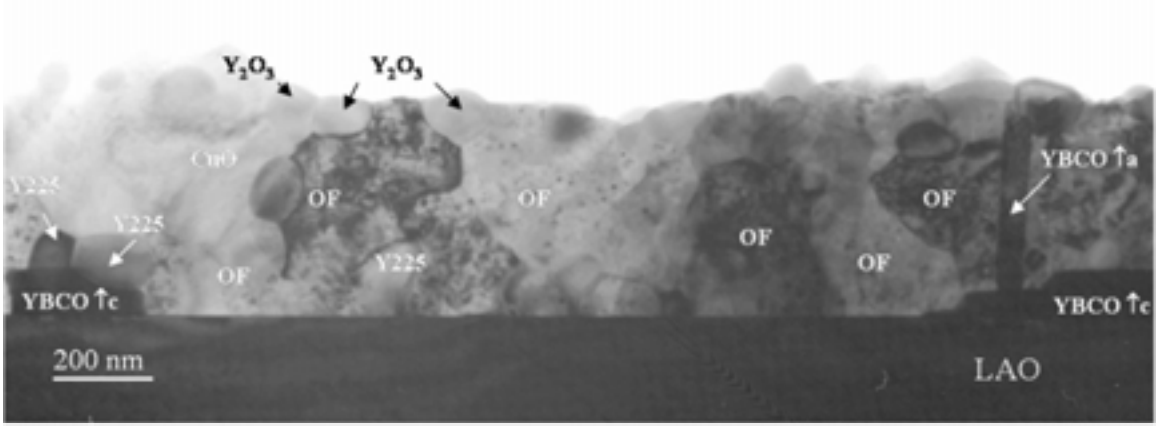

Figure 4-7. Low-magnification XTEM image of the film quenched from 795 ºC observed from [100]LAO. Phases identified from EELS analyses performed at some points of the specimen are indicated. c-axis oriented YBCO islands with a thickness of 80 - 90 nm are observed. An a-axis oriented YBCO grain is also shown on top of an island.

Careful inspection of the XRD pattern of the 795 ºC sample in Figure 4-2, also exhibits a shoulder between the CuO and (005)YBCO peaks, that can be attributed to Cu_2O. A careful observation of Cu-O rich areas in XTEM images, Figure 4-8 (a), signaled the coexistence of two phases, one exhibiting nanocrystalline features and another one exhibiting well developed grains. EELS spectra obtained from the nanocrystalline and grain like phases, shown in Figure 4-8 (b), exhibit distinctive features characteristic of Cu_2O for the nanocrystalline phase and CuO for the grain-like phase. In particular, that corresponding to Cu_2O can be distinguished by a slight shift towards higher energy losses. This microstructure clearly indicates that under the present conditions, CuO is the stable form of Cu-oxide and grows at the expenses of Cu_2O. According to an investigation of e-beam co-evaporated films, this transformation takes place up to 500 ºC to 700 ºC [80]. However it is worthy to note that, in agreement with reports on the TFA process by other authors [67,64], in the course of the present investigation we have found that the dominant form of Cu-O is CuO throughout the whole process, the pyrolysis step required in the TFA route favors the formation of CuO. The Cu_2O-CuO boundary is close to 700 ºC at the growth conditions ($pO_2 \sim 2\times10^{-4}$ atm) and therefore the observation of Cu_2O might be attributed to a partial reduction of CuO during heating to the growth temperature (795 ºC) [81].

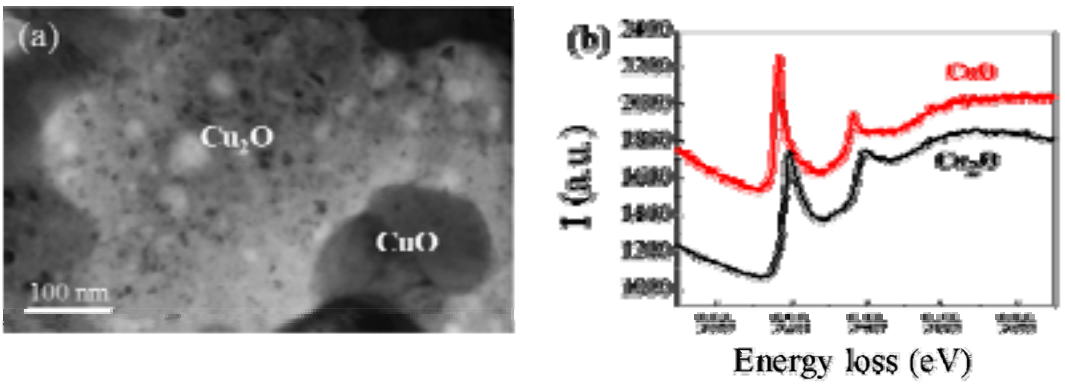

Figure 4-8. (a) Low-magnification XTEM image of the film quenched from 795 ºC showing regions nanocrystalline and grain-like regions of a Cu-O rich area. (b) EELS spectra obtained from both, nanocrystalline and grain-like, areas revealing the L-Cu peaks of Cu_2O and CuO, respectively.

Turning to the issue of YBCO versus Y225 competitive growth, let us focus back to Figure 4-7. There is a YBCO island located close to the left hand edge of the image, which supports two Y225 grains on its top. Note that the growth of the island is clearly impeded by the two grains, particularly, that located on the right hand side. High temperature in-situ XRD experiments of e-beam evaporated precursor films have revealed that the Y_2O_3+2CuO→ $Y_2Cu_2O_5$ reaction takes place at ~700 ºC [80], thus indicating that $Y_2Cu_2O_5$ and YBCO nucleate at very close temperatures. Our observations, in fact reveal that the nucleation and growth of YBCO is assisted by long range diffusion within a Ba-oxyfluoride matrix rather than interphase reaction among the different phases. Hence, the conversion of the precursor to YBCO does not necessarily require the formation of Y225, but its formation, though unavoidable under the present conditions, may even slow down the kinetics of the transformation to YBCO, with important implications from the industrial production point of view. Interestingly, Wong-Ng et al reported for the e-beam co-evaporation process, that YBCO films can be obtained without the formation of Y225 when (BaF_2+YF_3+Cu) precursors are used [80]. Though in that particular case the reaction was incomplete at the end of a standard process, this finding, demonstrates that the microstructural scenario for the conversion to YBCO can be dramatically modified through a proper choice of the precursor materials. This is an interesting extreme deserving further attention.

As a further manifestation of phase segregation we consider here the ordering of the OF phase. High resolution XTEM images of the OF matrix featured fingerprints of

atomic ordering, either within nanometric domains embedded in the OF (Figure 4-5 (a) and Figure 4-5 (b)), or within larger domains surrounding heteroepitaxial YBCO islands, as shown below. Figure 4-9 is a high resolution electron micrograph showing such an ordered domain (arrowed in the figure), characterized by a triple $d_{(111)}$ spacing of the corresponding OF phase. The formation of this phase is important because it has been suggested to constitute a template for the topotactic nucleation and growth of YBCO [72]. Previous reports suggest that there is not a unique way to order the OF phase, and it is likely that a series of related OF-based superstructures exists [80]. Among these, that reported by Wong-Ng et al has lattice parameters a = 0.74nm, b = 1.05nm, and c = 0.43nm (in this setting, the [010] direction of the superstructure is taken along the [111] direction of the OF fluorite-type structure). Note that the $d_{(111)}$ spacing of the fluorite structure is tripled as result of ordering. Thus, the peak marked as OF1 in Figure 4-2, appearing at $2\theta \sim 25.5^{\circ}$, can tentatively be attributed to the (030) peak of the ordered OF.

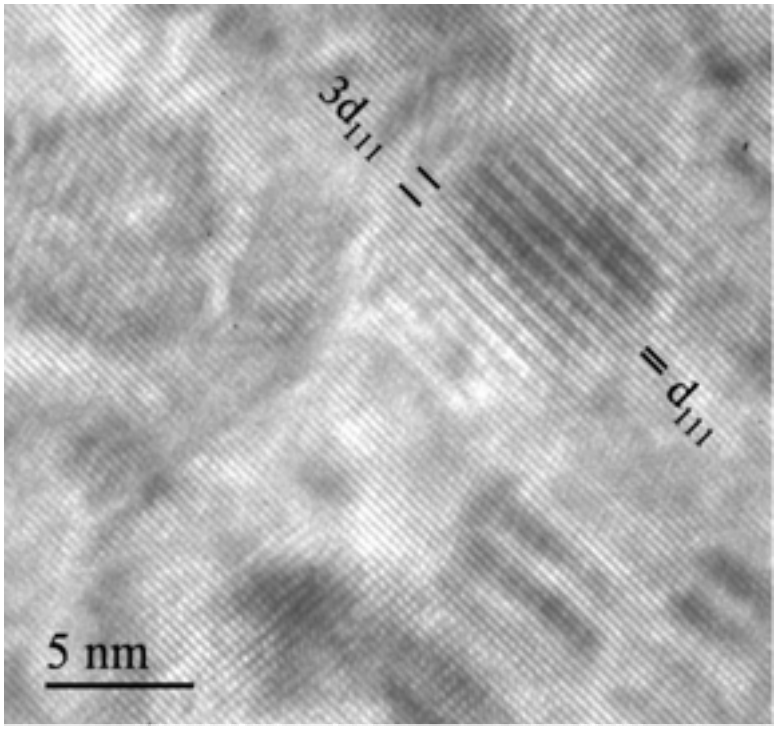

Figure 4-9. High resolution XTEM image evidencing atomic ordering within a nanometric domain embedded in the OF matrix. The signaled domain exhibits a tripled $d_{(111)}$ spacing.

4.5 Texture of precursor phases, nucleation and growth mechanism of YBCO

As discussed above, the BYF solid solution evolves to the OF type phase on heating up to the growth temperature at 795 ºC. During this process, Y_2O_3 forms which can either nucleate within the bulk OF phase, or heteroepitaxially on the substrate surface. Figure 4-10 is a high resolution XTEM image, viewed along the <100>LAO direction, showing a heteroepitaxially nucleated ~3 unit cell YBCO island embedded in a Y_2O_3 matrix. The epitaxial relation between the Y_2O_3 and the LAO substrate is $(111)Y_2O_3//(001)LAO$, $[-12-1]Y_2O_3//[100]LAO$.

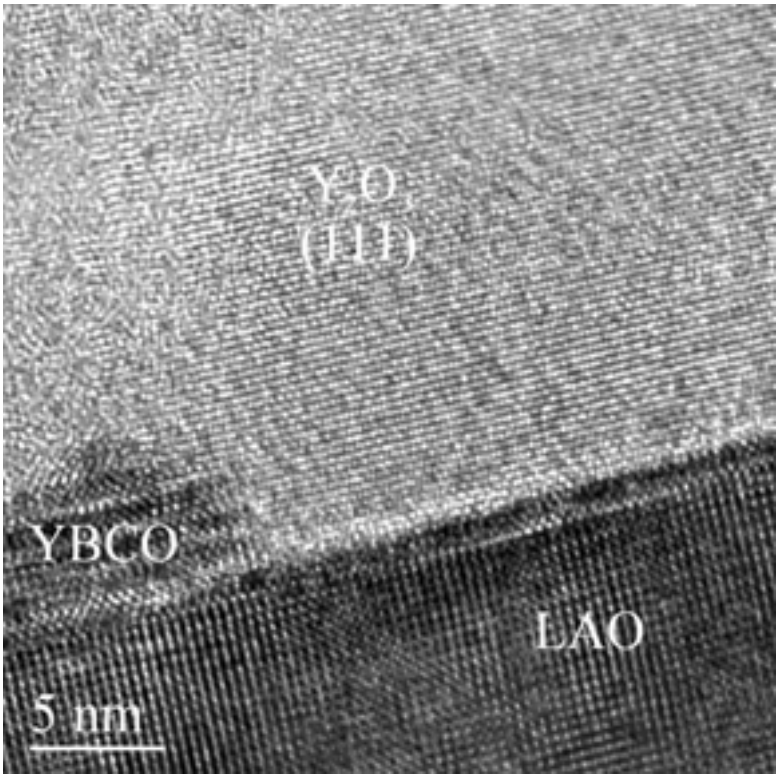

Figure 4-10. High resolution XTEM image of a YBCO nucleus embedded in a (111) oriented Y_2O_3.

In order to obtain an average picture of the texture of the fluoride phase in a sample quenched from 795 ºC, a pole-figure was recorded for a 2θ value of 41.1º, which corresponds to the (202) reflection of the OF phase and the (111) reflection of the LAO substrate. The resulting pole-figure, shown in Figure 4-11 (a) exhibits the four

equivalent {111} LAO poles at an inclination, χ = 54.7º, providing the in-plane orientation of the substrate for reference. Decreasing the inclination to the substrate normal, one first finds, at χ = 45º, four poles corresponding to the {202} planes of the (001) oriented OF (hereafter denoted as {202}OF$^{<001>}$). These poles appear superposed to a ring of intensity which tells that a significant fraction of (001) oriented OF exhibits uniaxial texture. The coincidence in azimuth (ϕ) between the {202} poles of the in-plane aligned fraction of the OF phase and the {111}poles of LAO, is consistent with an epitaxial orientation relationship given by: (001)OF$^{<001>}$//(001)LAO, [110]OF$^{<001>}$//[100]LAO. This orientation corresponds to the minimum mismatch strain ε. At room temperature, taking a_{OF} = 0.62 nm, this gives ε ~13%. Finally, the pole-figure shows a series of intensity maxima distributed on a ring located at χ ~35º. These maxima correspond to the {220}-type poles associated with the (111) oriented OF. Careful inspection reveals that the maxima are not randomly distributed, but most of them are located at the vertices of four equilateral triangles rotated 30º one to each other. In order to understand the in-plane orientation which is derived from this pole arrangement, Figure 4-11 (b) shows the stereographic projection of the {100}LAO and {220}OF poles along the [001]LAO and [111]OF directions, respectively. In the cubic system, there are 12 {110} equivalent planes or poles: 3 are inclined 35º to [111], their inverse counterparts (not shown), and 6 poles lying on the equator, separated 60º to each other. The latter 6 ones, therefore, define 3 equivalent matching directions on the interface plane (Figure 4-11 (b)). Comparison of Figure 4-11 (a) and (b) reveals that the four triangles identified in the pole-figure, correspond to six ways to align <110>OF with <100>LAO (or equivalently <100>OF with <110>LAO) on the interface plane, namely: [-110]OF, [-101]OF and [01-1]OF can align either with [100]LAO or [010]LAO. Note that a 180º rotation leaves the configuration unchanged, hence triangles 1 and 3, and 2 and 4, as indicated in Figure 4-11 (a), correspond to equivalent orientations. On the other hand, each triangle may correspond to 3 different in-plane orientations each obtained through a 120º rotation around the substrate normal. The six non-equivalent in-plane orientations are then obtained considering the three different possible orientations each associated with two independent triangles (e.g. 1 and 2).

Figure 4-11. (a) Pole-figure corresponding to the (202) OF and (111) LAO reflections, and (b) Stereographic projection of the {100}LAO and {220}OF poles, viewed along the [001]LAO and [111]OF directions, respectively.

As a result of the ternary symmetry of the [111] projection, each in-plane orientation only satisfies lattice matching along one direction, and therefore, owing to interfacial energy considerations, (111) oriented OF nuclei would be less favoured than (001) oriented ones (which carry two orthogonal <110> matching directions). This considerations would explain the strong tendency of the fluoride phase to nucleate with (001)-type orientation, as signaled by the prominent (002) peak observed in Figure 4-2. An estimation of the volume percentage of (111) oriented OF using θ–2θ scan intensities, assuming only (111) and (001) type orientations, in fact yields only 15%. As commented at the beginning of this section, XTEM observations have revealed the occurrence of (111) oriented Y_2O_3 (Figure 4-10). Therefore, very likely, we have overestimated the intensity of the (002) OF reflection as a result of its overlap with the (222) Y_2O_3 one. However, the observation of other, non heterogeneously nucleated, Y_2O_3 particles far from the interface, suggests that this contribution is small. Anyway, the derived value of 15vol% for (111)-OF, is indicative of a dominant population of (001) oriented OF. Figure 4-12 is a high resolution XTEM image showing a (001) oriented heteroepitaxial BYF growing on the (001)LAO surface, this marked texture of the fluoride phase might result from the strong tendency for its heteroepitaxial nucleation on the LAO (001) surface.

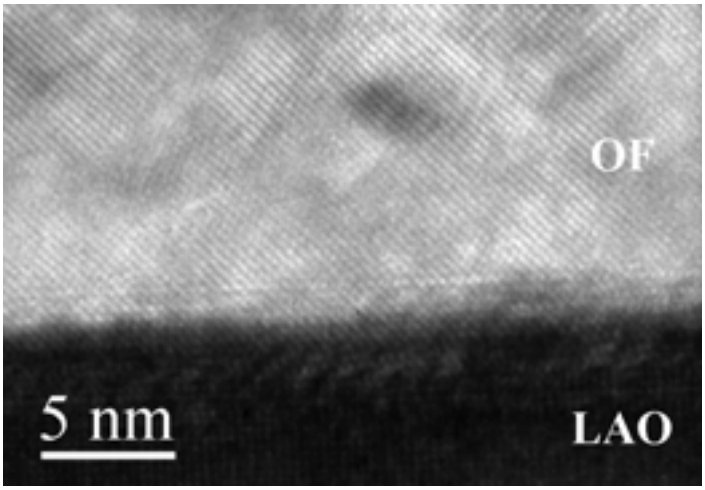

Figure 4-12. High resolution XTEM image of the (001) oriented OF matrix quenched from 795ºC.

As shown in the previous section, the OF phase is prone to develop ordered structures, which main fingerprint is the tripling of the (111) spacing of the basic fluorite structure. It has been argued that such a superstructure has a templating effect on the nucleation of YBCO, in such a way that, owing to the similarity 3d(111)OF ~ d(001)YBCO, the YBCO nuclei grow c-axis oriented on a (111) oriented OF matrix. The correspondence between both structures is clearly illustrated by the high resolution electron micrograph shown in Figure 4-13. The image shows in detail the growth front of a (001) oriented YBCO island expanding through a (111) oriented fluoride region. Note that the OF phase is ordered, such that its (111) spacing triples that of the corresponding basic fluorite structure, being almost identical to the (001) spacing of the growing YBCO island. From a topological point of view, ordering constitutes a particularly favourable situation for the growth of (001) oriented YBCO through the (111) oriented OF phase.

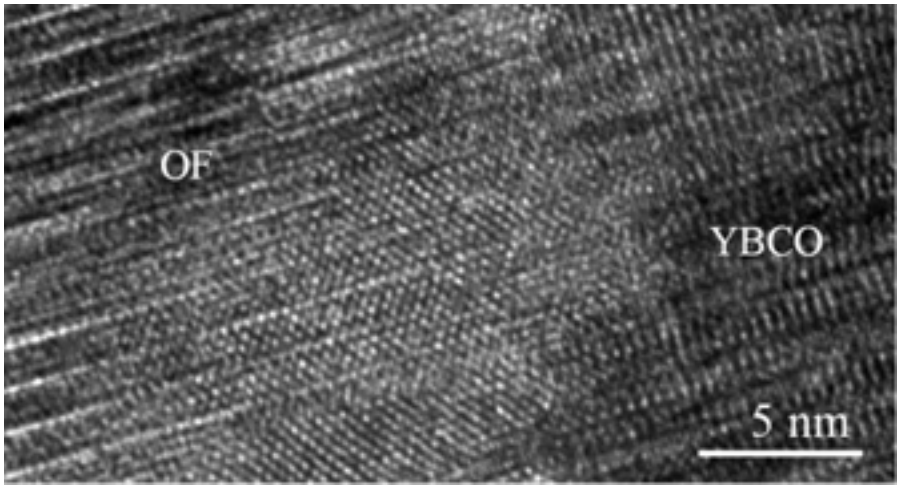

Figure 4-13. High resolution XTEM image of the growth front of YBCO within (111) oriented OF exhibiting a $3d_{(111)}$ superstructure.

Other observations, however, show that not always the (001) oriented growth of YBCO is assisted by the OF superstructure. As an example of this situation, Figure 4-14 (a) and (b) are a high resolution XTEM images of a (001) oriented YBCO island expanding through the (111) oriented OF matrix, but in this case the OF phase does not exhibit superstructure fingerprints.

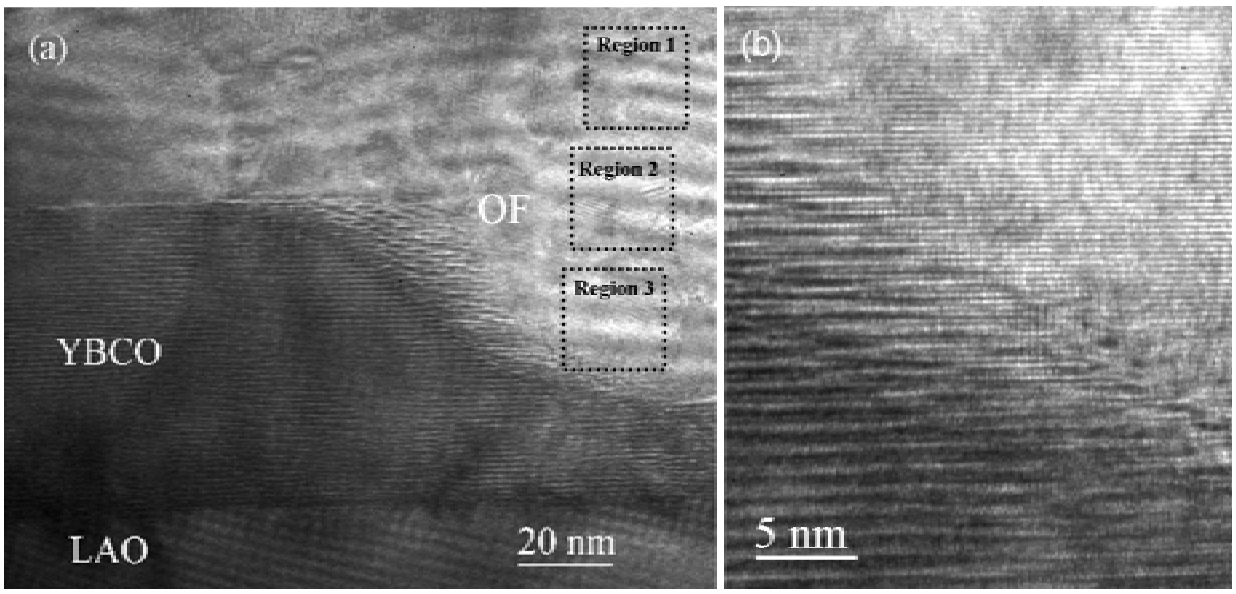

Figure 4-14. (a) High resolution XTEM image of the growth front of YBCO within (111) oriented OF. Boxed areas correspond to regions used for FFT analysis of lattice parameters. (b) Magnification of the growth front.

These results, in fact demonstrate that almost full (001) oriented YBCO films are obtained from precursors exhibiting a percentage of (111) oriented OF significantly

smaller than that corresponding to the final fraction of (001) orientated YBCO, thus questioning even the relevance of (111) oriented OF for the nucleation and growth of (001) oriented YBCO, regardless the development of the OF superstructure. In fact TFA derived YBCO has always been found to nucleate on the buried substrate surface, either $SrTiO_3$ [72] or LAO [67]. Therefore, the orientation of the first YBCO nuclei is very likely to be determined by the orientation of the substrate surface rather than the orientation of the OF matrix. This view is, however, not contradictory with the appreciation that the growth of c-axis oriented YBCO is favoured within the (111) oriented OF. Such areas very likely provide selective low barrier nucleation sites for YBCO on the buried substrate surface. Growth of such islands beyond the boundary of (111) oriented OF regions can then take place through the conversion to YBCO in a different scenario, like for instance (001) oriented OF or eventually other phases nucleated on the substrate surface, such as (111) oriented Y_2O_3 (Figure 4-10).

Turning back to Figure 4-14, this image was also used to measure the lattice parameters of the OF phase around the growing YBCO, by analyzing the FFT spectra obtained at different points of the image, as indicated by boxes. The size of the boxed areas is equivalent to the size of the transformed region. The lattice parameter obtained from region 1, at ~45 nm from the interface, a = 0.620 nm, corresponds to the OF phase identified in the XRD patterns. However, there is a marked decrease of the fluorite cell dimensions towards the interface: at region 2 the lattice parameter is 0.602 nm, and drops down to 0.595 nm at the interface (region 3). Such a variation of the lattice parameter around the YBCO growing island very likely reflects a concentration gradient ahead of the YBCO-OF interface. It is interesting to note that the latter value corresponds to the higher Y concentration compatible with the fluorite type solution [66], thus suggesting a Y concentration gradient ahead of the growth front. The weak diffraction peak marked by OF2 in Figure 4-2 would then correspond to a lattice parameter of 0.597 nm, and can therefore be associated to this Y-enriched fluoride adjacent to the growth front of YBCO islands. Anyway, the present results suggest that the growth rate of the YBCO island is limited by the rate of incorporation of Y rather than by diffusion through the OF matrix. On the other hand, in the course of the present investigation we have not detected any evidence of liquid layer formation adjacent to the growth front, thus indicating that the growth process appears to take place exclusively in the solid state.

4.6 Conclusions

Since pyrolyzed films are typically amorphous or quasi-amorphous, film crystallization in solution-derived thin films occurs by a nucleation-and-growth process. The theoretical description for nucleation and growth processes in solution derived films is similar to those concerning the transformation of a gel into a glass, where an amorphous solid is transformed into a crystal material, discussed in chapter 2.

After the pyrolysis, simultaneously with the disappearance of the organic content, crystallizes a BYF matrix with embedded CuO nanoparticles. Upon heating, the microstructural evolution of the precursor is driven by the reduction of the solid solubility of Y in the BYF solid solution. Thus, Y is released in the form of Y_2O_3 which can react with CuO to form $Y_2Cu_2O_5$. According to a previous report this reaction occurs at ~700 ºC [80], i.e., close to the YBCO nucleation temperature. At 795 ºC, EELS analyses of the matrix reveal a significant oxygen content and only a weak signal of Y. This compositional evolution agrees with the previously reported F/Ba ratio trajectory, determined from fluorine selective electrode measurements [65]. No traces of BaO are detected at any stage of the process, thus reinforcing the view that YBCO forms by a diffusive topotactic-like mechanism within the OF matrix. Although there are reports indicating that the observed compositional trajectory crosses low melting point regions [80,65], we have not found any conclusive microstructural evidence supporting the formation of partial melts during the process.

Besides the evolution of the fluoride/oxyfluoride type matrix, the microstructural evolution of the precursor film is characterized by coarsening of the CuO particles and the formation of $Y_2Cu_2O_5$ in the bulk matrix. In particular, the formation of this latter oxide is particularly relevant because it occurs at temperatures very close to the epitaxial nucleation of YBCO, and therefore both processes may constitute competitive phenomena thereof affecting the kinetics of the conversion process.

As indicated by early studies [72,82], the present work supports that (111) oriented OF domains provide low barrier nucleation sites on the buried substrate surface. Surprisingly, however, such regions only represent about 15% of the total OF matrix. It is not clear, at present, whether under operating supersaturation conditions, initial nucleation of YBCO is restricted to such regions or, on the contrary, the supersaturation is too large to make nucleation sensitive to barrier differences associated with the different environments found on the substrate surface. In this context,

anomalously large distances between nuclei found in this system (see Figure 4-7) would support a preferential affinity for the nucleation on low barrier (111) oriented OF domains. This is a major issue with implications on the grain boundary quality and distribution which deserves further attention.

CHAPTER 5
STRUCTURAL DEFECTS IN TFA-YBCO THIN FILMS

Chapter preview

This chapter aims to present a description of structural defects occurring within TFA-YBCO films. Transmission electron microscopy is the essential microstructural tool to identify and evaluate the microstructural defects that might act as *natural* pinning centres, as well as for the pinning centres artificially introduced (seen in the next chapter). The TEM study of a TFA-YBCO thin film shows that large grains of YBCO (several times the film thickness), which contains a variety of defects, such as stacking faults, twist boundaries and dislocations, mainly in basal plane.

5.1 Introduction

The high supercurrent carrying capacity of YBCO is a consequence of the pinning of flux lines by *particular* crystal defects. Assuming a single vortex core pinning mechanism, the basic requirement to enhance pinning is that the gradient of the superconducting order parameter at the defect-YBCO matrix interface should be as sharp as possible [83]. Hence, nanoscale variations of the superconducting properties are positive in the case of point and line defects, because the interaction between vortices and these microstructural defects (with the superconducting properties strongly suppressed) may act as vortex pinning centers and stabilizes vortices against motion, and therefore enhance the critical current density.

Depending on the shape and the dimensions of the microstructural defect, defects may act as point-like, linear-like or surface-like pinning centers:

- Point-like pinning centers, when the defect has dimensions of the order of the coherence length ($\xi_c \approx 0.3$ nm and $\xi_{ab} \approx 2$ nm for YBCO [1]). Consequently, the region where the defect is present will have suppressed superconducting properties and will act as a point-like pinning center.

- Linear-like pinning centers, when one of the dimensions of the defect (parallel to the vortex) is larger than the coherence length while the other two are of the order of ξ. The vortex will, therefore, be pinned over a large length.

- Surface-like pinning centers, when two of the dimensions of the defect (parallel to the vortex) are larger than the coherence length while the other one is of the order of ξ. In that case, the effectiveness of a planar defect will depend on the motion of the vortices due to the Lorentz force. Planar defects could be strong pinning sites when the vortices were pushed against the surface, while they could act as *channels* for easy vortices motion when the Lorentz force is directed along their surface plane.

Obviously, defects that confine a longer section of vortex core should provide better pinning. The effectiveness of linear (out of plane) flux pinning centers in YBCO has been demonstrated by creating amorphous ion tracks by heavy ion irradiation [84]. However, there are still several microstructure issues related to high-Tc YBCO superconductors we need to address. The fundamental crystal and electronic structure of YBCO superconductor has a marked two dimensional behaviour which in turn determines their structural anisotropy and superconducting properties. Such anisotropy

also affects crystallographic defects evolution, for example the difficulty to create correlated defects as dislocations perpendicular to CuO_2 layers. Dislocations are the closest natural defects to ion tracks, but dislocations in YBCO belong to the glide systems [100](001), [010](001) and <110>(001), i.e. they are confined in the basal plane [85]. Besides, during the tetragonal-to-orthorhombic phase transition upon cooling down, (110) and (-110) twins form, and upon sample oxygenation Y248-type stacking faults develop parallel to the (001) plane by the insertion of an extra CuO_x atomic layer. All of them, dislocations, twin boundaries and stacking faults are good candidates due to their extended and correlated characters. Of course, all of them are capable to influence vortex pinning in YBCO films either acting as point-like or linear-like depending on the direction of both the applied magnetic field and the Lorentz force.

Most of the microstructural studies and their physical properties correlation on the YBCO superconductor are related to melt-textured composites, while most of the counterpart studies related to YBCO thin films have been addressed to films deposited by vacuum deposition techniques such as PLD and sputtering [86,87,88]. Gerber and co-workers [89] and Hawley and co-workers [90] observed a high density of growth spirals at the surface of YBCO films. Furthermore, experiments on miscut [91] and bicrystal [92] substrates indicated the importance of the dislocation pinning in films. However, sketchy microstructural studies have been done of TFA-YBCO thin films, and it is well known that the relevant microstructural features described above appear during the YBCO conversion. Precursor coating, pyrolysis of the organic components and YBCO nucleation and growth are the basic steps of the TFA process. Although these are separate processes, each step is dependent on the preceding steps in order to successfully fabricate a high-quality film. Therefore an understanding of each process separately will yield a better control of the sample's microstructure and therefore its properties. Our group has reported several studies on the possible influence of the first three steps (from the precursor synthesis to pyrolysis step) on the resulting critical current density J_c [93,94], while the chapter 4 of the present thesis addressed the precursor decomposition and microstructural evolution of the sample annealing: the precursor film, after the pyrolysis, consisted of a partly amorphous nanocrystalline matrix of $Ba_{1-x}Y_xF_{2+x}$ and CuO. Upon heating, such a precursor underwent a strong phase segregation. Our results made evident that the nucleation of YBCO toke place exclusively at the interface with the substrate, within a fluoride phase. YBCO islands grow faster laterally and coalesce still within the oxyfluoride matrix. Consequently, that

process induced the development and evolution of specific defects, which could interact along the thermal evolution of the sample yielding to particular and complex microstructure. As we will see forth, YBCO films grown by the TFA process are highly textured, with a layered structure which suggests a laminar growth. These large grains of YBCO (several times the film thickness) contrast with the columnar microstructure of YBCO films deposited by vacuum deposition techniques such as PLD [95].

First of all, in the present chapter we will go over the theory of the diffraction contrast analysis of defects for a better understanding of TEM images and their implications. Secondly, we address the physical properties of YBCO thin films by means of angular transport measurements by the *physical properties team* of our laboratory. Finally, we go through detailed TEM observations of the defect structure in TFA-YBCO thin films and its origin, which may lead to a better understanding of the physical properties measured on such TFA-YBCO films.

5.2 Diffraction contrast analysis of defects [26]

In TEM imaging, when the beam transmitted directly through the specimen is selected, a bright-field image is displayed, whereas when one of the diffracted beams is chosen, a dark-field image is observed. In both cases the contrast analysis of defects is based on the **g·b** criterion which requires two beam conditions.

A TEM image simply reveals the variation in intensity of the selected electron beam as it leaves the specimen. In the theory of this diffraction contrast, it is usually assumed for simplicity that the intensity variation across the bottom surface of the specimen may be obtained by considering the specimen to consist of narrow columns (a few nm wide) with axes parallel to the beam: the electron intensity does not vary across a narrow column and is independent of neighbouring columns. The final image is therefore an intensity map of the grid of columns. If the specimen is perfectly flat, uniformly thick and free of defects, the image is homogeneous with no variations in intensity. Image contrast only arises if variations in beam intensity occur from one part of the specimen to another. For example, if the specimen is sufficiently bent in one region to affect crystal planes which are close to the Bragg condition, strong variations in intensity can result. Dislocations and many other crystal defects bend crystal planes.

The effect of crystal defects on the image depends on the vector **u** by which atoms are displaced from their perfect lattice sites. In the column approximation, **u** within a column varies only with **z**, the coordinate along the column axis. Solutions of the equations for the electron intensities contain a factor **g.u**, or alternatively $\mathbf{g}\cdot d\mathbf{u}/dz$, which is not present for a perfect crystal [26]. Thus, diffraction conditions for which $\mathbf{g}\cdot\mathbf{u}$ (or $\mathbf{g}\cdot d\mathbf{u}/dz$) is zero will not lead to contrast in the image. The physical interpretation of these effects follows from the fact that $d\mathbf{u}/dz$ is the variation of displacements with depth and therefore measures the bending of atomic planes. If the reflecting planes normal to **g** are not bent by the defect, there is no change in diffracted intensity and the defect is invisible.

Certain planes near a dislocation are bent and the bending decreases with increasing distance from the dislocation. If these planes are bent into a strongly diffraction orientation, the intensity of the directly transmitted beam will be reduced (and that of the diffraction beam increased) in columns near the dislocation. The dislocation will appear as a dark line in the bright-field image (or as a bright line in a dark-field image).

The invisibility criterion is $\mathbf{g}\cdot\mathbf{u} = 0$. If we consider a screw dislocation, for example, planes parallel to the line remain flat, since **u** is parallel to **b**. Hence, when **g** is perpendicular to **b**, $\mathbf{g}\cdot\mathbf{u} = \mathbf{g}\cdot\mathbf{b} = 0$ and the invisibility criterion is satisfied. We just have to found two diffraction planes, $\mathbf{g_1}$ and $\mathbf{g_2}$ satisfying the invisibility criterion, therefore the Burgers vector has the direction $\mathbf{g_1} \times \mathbf{g_2}$. For an edge dislocation, all planes parallel to the line are bent, and **u** is non-zero in all directions perpendicular to the line. The criterion $\mathbf{g}\cdot\mathbf{u} = 0$, therefore, requires in this case that both $\mathbf{g}\cdot\mathbf{b}$ and $\mathbf{g}\cdot(\mathbf{b} \times \mathbf{t})$ be zero, where **t** is a vector along the line. It is satisfied when **g** is parallel to the line and, for only planes perpendicular to the line remain flat.

Stacking faults also form a characteristic image contrast in the TEM. A fault is produced by the displacement of the crystal above the fault plane by a vector **R** relative to the crystal. For columns passing through the fault, the stacking fault introduces a phase factor $2\pi\mathbf{g}\cdot\mathbf{R}$ into the main and diffracted beam amplitudes. Thus, when $\mathbf{g}\cdot\mathbf{R}$ is zero or an integer, no contrast is present and the fault is invisible.

5.3 Critical current measurements

Angular transport measurements enable to discriminate among defects dimensionality and therefore are unique in determining the effectiveness of the microstructural defects [96,97]. Investigations of the angular dependence of J_c made by our group provide insights into the pinning behavior of the TFA-YBCO films [35]. Any influence of defects on vortex pinning can be established by a J_c anomaly when H is aligned with the defects.

The layered structure of YBCO has a deep influence on its vortex dynamics. First, it generates an electronic mass anisotropy, defined as $\varepsilon^2 = m_{ab}/m_c$ and being $\varepsilon \sim 1/5\text{-}1/7$ in the case of YBCO [3], and consequently an anisotropy in the superconducting properties. In particular this makes the vortex energy per unit length to depend on the orientation, which in turn results in anisotropic pinning, even in the case of random defects that would otherwise produce isotropic defects. Second, due to the small coherence length along the c axis (ξ_c) as compared to the layer separation d ~ 1.2 nm, the amplitude of the order parameter is periodically modulated along the c direction, giving rise to *intrinsic pinning* when the vortices are near parallel to the ab planes.

Intrinsic pinning is an example of correlated pinning, analogues to that produced by extended and approximately parallel planar or linear structures, such as twin boundaries and screw and edge dislocations [84,86,87,98,99]. The fingerprint of correlated pinning in the critical current density (J_c) is a peak as a function of the orientation of the applied magnetic field, centered at the defect's orientation. Extended planar defects parallel to the ab planes, such as stacking faults or basal dislocations, also produce correlated pinning with the associated J_c peak centered at H // ab, as the intrinsic pinning peak is.

Figure 5-1 shows the angular dependent critical current density, J_c, for YBCO thin film deposited onto LAO substrate at 75 K under different magnetic fields ($\mu_0 H$), 1, 3 and 7 T. The geometry used is J // ab plane and keep H $\perp$ J (maximum Lorentz force) as it is shown in the inset. Notice that for H//ab a strong and sharp increase of J_c occurs in agreement with the anisotropy of the YBCO material. Additionally, for H//c an increase of J_c, though moderate, is also observed. While the main source of $J_c(\theta)$ is the anisotropy of the electronic mass in YBCO, also anisotropic pinning contributions

appear near H//ab and H//c [100]. Concerning the later pinning contributions, the main source of the peak at θ = 90º are the intrinsic pinning by the CuO_2 planes, in-plane dislocations and stacking faults. The peak centred at 0º is a sign of linear defects along c axis, bulk dislocations or twin boundaries. At intermediate angles, away from the preferred directions of the correlated defects, J_c is expected to be dominated by 3D-mass anisotropy and point defects. Notice that as the magnetic field increases, and the intrinsic pinning by CuO_2 pinning planes become more important, the ab peak of the J_c becomes sharper.

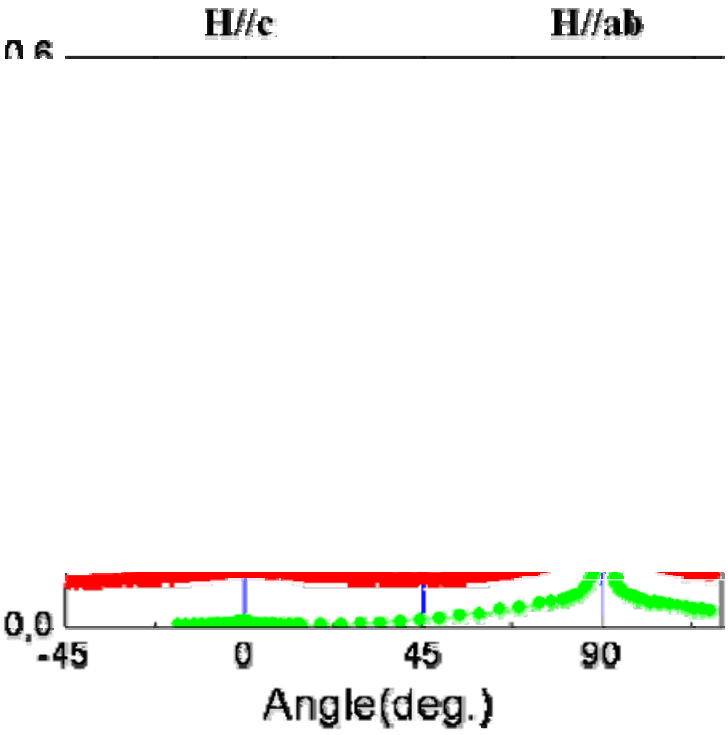

Figure 5-1. Transport critical current density, J_c, measured for a TFA-YBCO film as a function of θ at 75 K, for applied fields of $\mu_0 H$ = 1 T (in black, 3 T (in red) and 7 T (in green) [35].

When the applied magnetic field, $\mu_0 H$, reaches 7 T at 75 K the system is pretty close to the irreversibility line, which leads to a practically zero J_c. Figure 5-2 is an amplification of the J_c vs. θ curve at 7 T. Under such applied magnetic field, and for H//c, it can be observed that J_c is clearly dominated by correlated defects along the crystallographic c-axis of the film as can be seen from the shape of the curve. It is a strong evidence of a very strong pinning done by linear-like defects, such as

dislocations. At this field and temperature, around 30 degrees pinning is expected to be dominated by random defects, and as was said before, J_c becomes zero because we are close to the irreversibility field, but as the magnetic field gets more aligned with the extended defects along the c-axis i.e. around 0º, pinning becomes more correlated and dominates J_c, rising it to a non zero value. So at high magnetic fields and high temperatures the correlated pinning has pretty much importance [35].

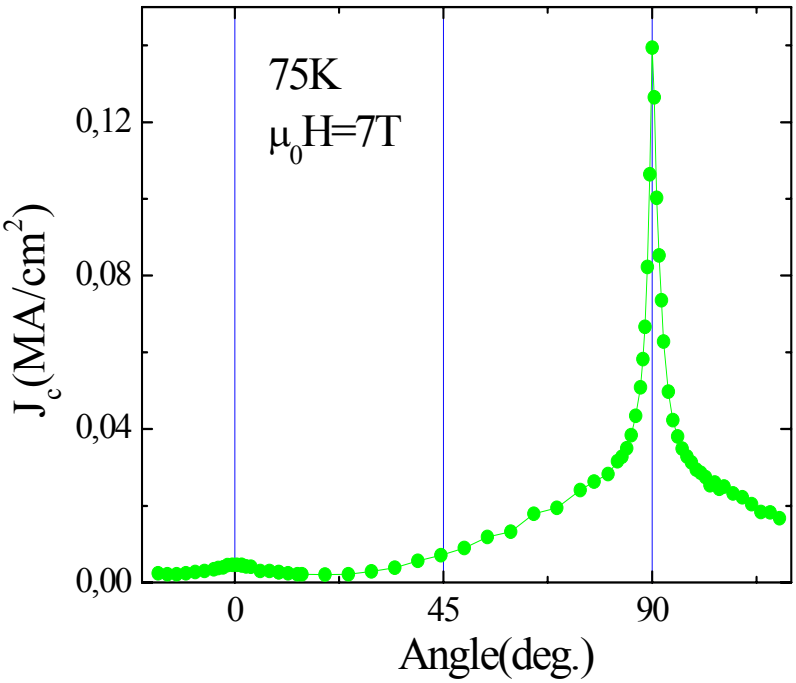

Figure 5-2. Transport critical current density, J_c, measured for a TFA-YBCO film as a function of θ at 75 K, for applied fields of $\mu_0 H$ = 7 T [35].

5.4 Extended defects in TFA derived YBCO: dislocations and stacking faults

We will analyze here the microstructure of an epitaxial TFA-YBCO thin film nominally 400 nm thick grown onto a (00*l*) LAO substrate. The standard growth process has already been described in the previous chapter. These settings result in a superconducting YBCO layer with J_c value of 4×10^6 Acm^{-2} at 77 K. An XRD analysis of the out-of-plane and in-plane textures of the superconducting film showed good alignment with FWHM values around 0.5º and 1.3º respectively.

5.4.1 Microstructure on the (00l) plane

Figure 5-3 shows a plan-view bright field image of the film taken near the [010] zone axis with (110) as the diffraction vector **g** = (110). As was said in the introduction, at lower temperatures, the oxygen in YBCO orders, forming an orthorhombic structure. The tetragonal-to-orthorhombic transition is accompanied by the formation of domains in order to relieve the spontaneous strains arising from the reduction of symmetry. Twin boundaries are then formed and oriented in order to maintain a strain compatibility between the adjacent domains, leading to two twin boundaries orientations, (110) and (-110). As a result, the [100] and [010] directions are exchanged across the twin boundaries such that the overall symmetry of the diffraction pattern remains tetragonal [101]. In YBCO twin domains are shaped in the form of lamellae parallel to their {110} twin boundaries.

With such diffraction vector, **g** = (110), one of the twin domain orientations should disappear, that perpendicular to **g**, as it can be seen in the left bottom part of Figure 5-3, where the (-110) oriented twin boundary is out of contrast. However, the diffraction condition is not strictly maintained in the entire imaged area, so perpendicular types of twin boundaries of each orientation, (110) and (-110), are visible. Twin boundaries are distributed in domains and are observed with a high density, being the distance between adjacent twin boundaries in the domains typically of ~50 nm. These average spacing is significantly smaller than the usual values in melt textured YBCO ceramics [102,103]. The twin boundary spacing reduction is consistent with the idea that the twin spacing is controlled by the dimension of YBCO grains [104], in this case, the thickness of the film.

Trickier seems to be the high density of twin intersections within a single grain observed in our samples. Actually, what it is not yet understood is what controls the occurrence of domains with {110} or {1-10} twin boundary orientations. This is an interesting issue because the size of domains exhibiting one single twin orientation determines the density of twin intersections, which may provide flux pinning centers, though their efficiency has not yet been elucidated. The presence of secondary phases as precipitates could provide strain inhomogeneities favouring a random nucleation of both types of twin orientation.

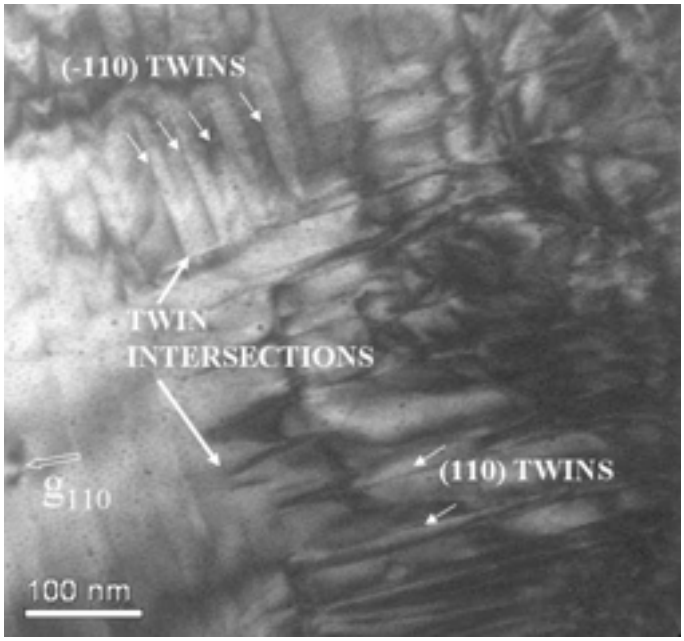

Figure 5-3. Plan-view bright field taken near the [001] zone axis with (110) as the diffraction vector.

Some regions of the previous image are obscured by a very strong strain contrast. The right part of the micrograph (Figure 5-3) exhibits a high concentration of dislocations, mostly lying on the basal plane. One would expect that the dislocations nucleate above the tetragonal-to-orthorhombic transition temperature (it will be discussed further on). This situation would correspond to an alternate orientation of the Burgers vector along [100] and [010]. Dislocations have a strong tendencyto be pinned by twin boundaries, as first described by Rabier and Denanot [85]. Figure 5-4 (a) is a (001) plan-view bright field image taken when the diffracting beam is **g** = (100). It can be seen in that image a set of parallel twin boundaries of only one type, and instead of this dense twin structure that might hinder the observation of dislocations, the image clearly shows basal dislocations (indicated by circles) exhibiting long segments pinned at twin boundaries. Figure 5-4 (b) is a schematic drawing of such basal dislocation. In Figure 5-4 (a) a disk-shaped staking fault (SF) is also indicated, which is oriented parallel to the plane of the foil; the resulting contrast is uniform.

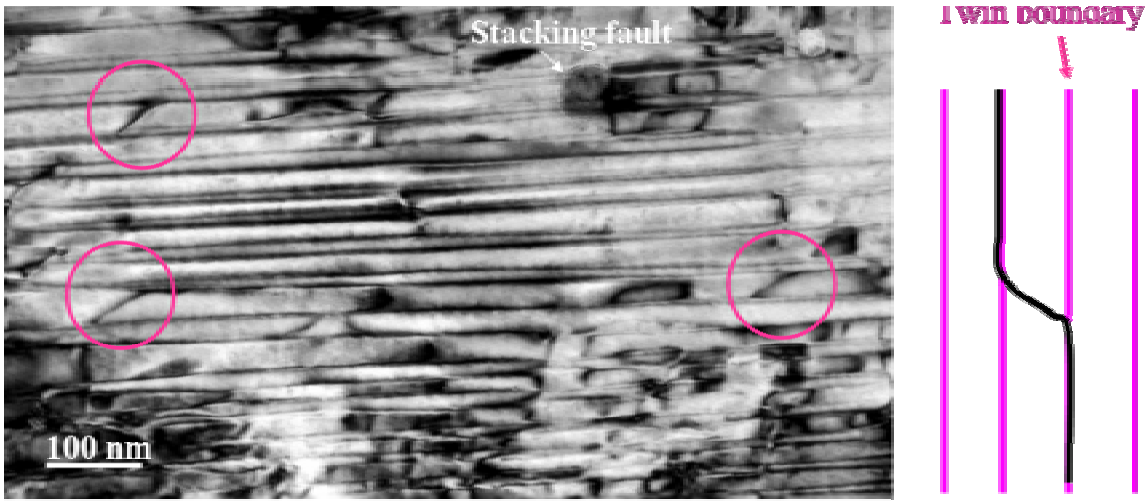

Figure 5-4. (a) Plan-view bright field image taken when the diffracting beam is **g** = (100). The arrow signals a stacking fault. Circles mark basal dislocations as are schematically drawn in (b). In that case, dislocations abandon pinning points.

Figure 5-5 shows a bright field image of the same region but with a different diffraction vector, **g** = (110). In this image the dislocation segment (marked with a square) displays oscillatory contrast indicating that it has climbed out of the basal plane. Therefore these dislocations are threading ones. They have a line direction close to [001] and therefore present a shorter projected length.

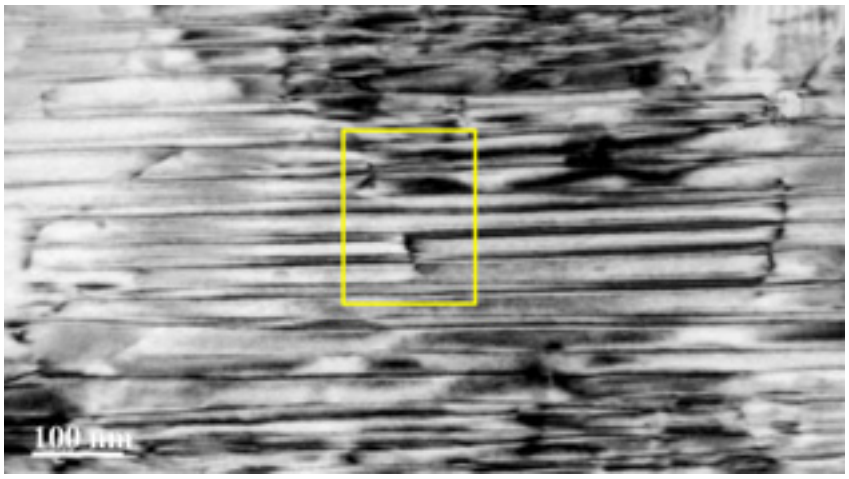

Figure 5-5. Plan-view bright field image taken when the diffracting beam is **g** = (110). Out-of plane dislocations are squared.

5.4.2 Microstructure on the (100) plane

Figure 5-6 shows a typical (100) cross-section bright-field TEM composite micrograph taken when the diffraction vector is **g** = (003). Overall the film has uniform thickness. TFA-YBCO films are characterized by laminar film morphologies due to their lateral growth. In that image the YBCO film presents abundant SF's. On the other hand, in-plane dislocations are in that case out of contrast (**g·b** = 0). Nevertheless, it is noticeable the horizontal inhomogeneous density of planar defects. Next to the faulted regions YBCO structure looks well-ordered and nearly defect-free over extended regions.

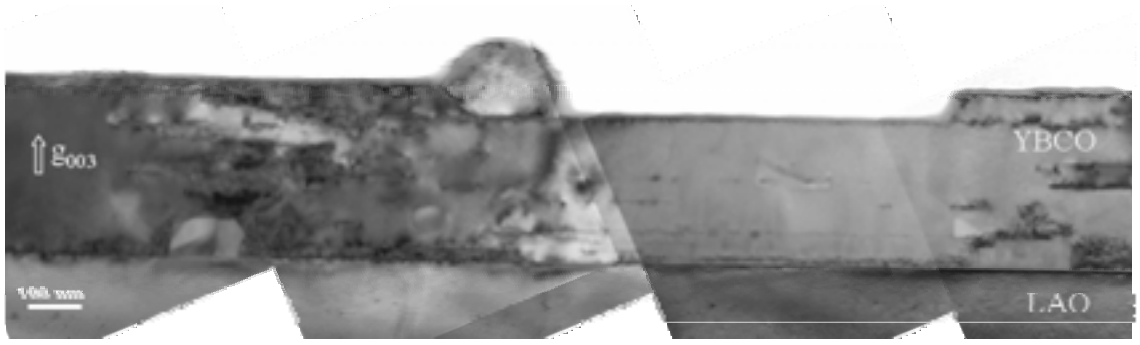

Figure 5-6. Cross-section bright-field TEM composite micrograph viewed along <100> of the YBCO film taken when the diffraction beam is **g** = (003).

The major defect structures seen in Figure 5-6 were stacking faults, but basal dislocations also appear when tilting the specimen properly. In Figure 5-7 (a) and (b), XTEM bright-field images taken with **g** = (200), in-plane dislocations appear as lines, while SF's exhibit a projected width, characterized by SF fringes. The images also show two examples of out of plane dislocations (large arrows) bowing on (100), with in-plane Burger's vector.

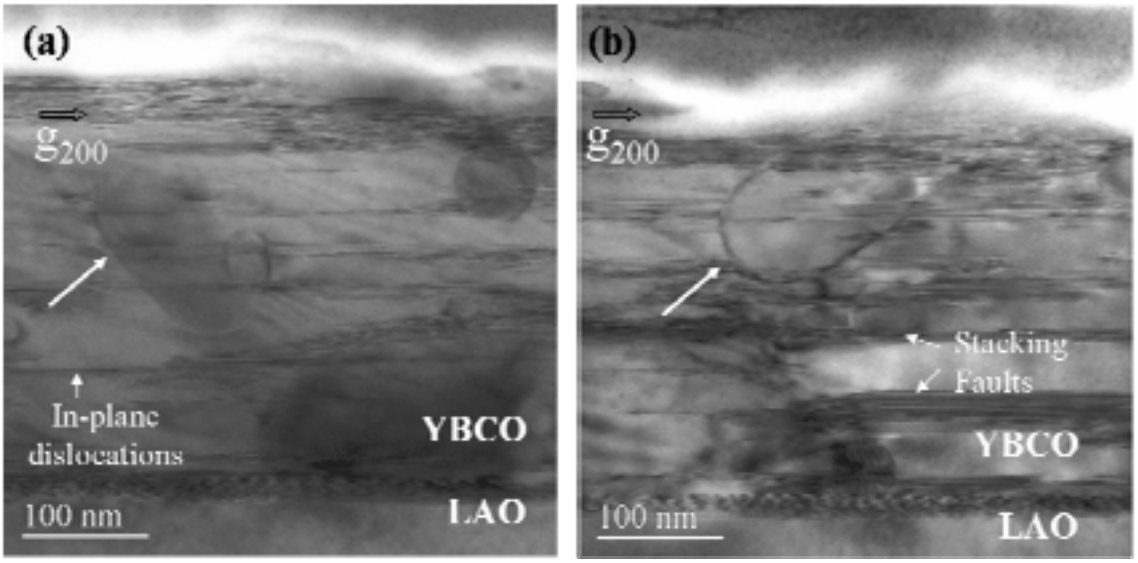

Figure 5-7. Pair of cross-sectional bright field images from different locations using as a diffraction vectors **g** = (200).

A stacking fault is a planar defect and, as its name implies, it is a local region in the crystal were the regular sequence has been interrupted. The most commonly observed stacking variation in the YBCO is an extra Cu-O chain layer which can form an ordered array resulting in the $Y_2Ba_4Cu_8O_{16}$ (Y248) or $Y_2Ba_2Cu_7O_{17}$ (Y247) phases [105], which are, in turn, superconducting phases with lower Tc's [106,107]. Figure 5-8 (a) is a high-resolution image of such fault structures (short arrows). Measurement of the unit cell height in the [001] direction of these layers shows that the addition of an extra Cu-O layer increased the c-axis parameter from 11.7 to 13.3 Å, matching the Y248 lattice parameter [108,105]. An isolated SF with a finite lateral extend is structurally analogous to a Frank loop, i.e., an extrinsic SF surrounded by a partial dislocation, Figure 5-8 (b). The displacement vector **R** of the Y248 SF and the Burgers vector of the dislocation are the same: $\pm 1/6\langle 301 \rangle$ [109].

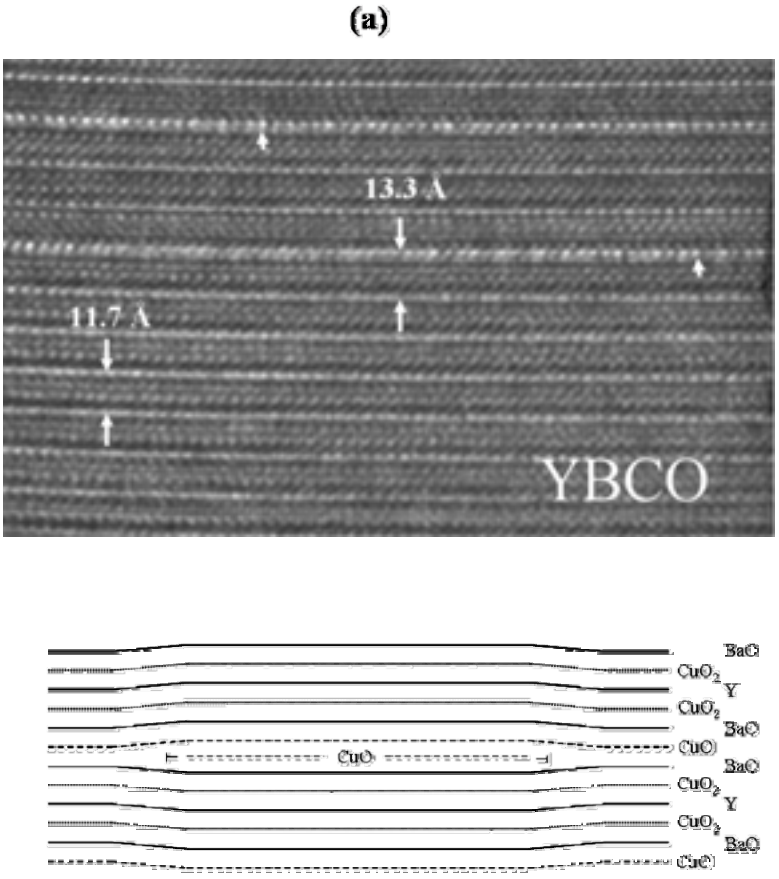

Figure 5-8. (a) High-resolution image of SF's within a YBCO film. The change in c-axis lattice constant from 11.7 to 13.3 Å indicates the intercalation of Y248 layer within the YBCO. (b) Schematic of a SF showing an extra CuO plane inserted between two unit cell layers of the YBCO structure; the fault boundary is a dislocation with Burgers vector [0,1/2,1/6] [109].

With a diffraction vector such as **g** = (-103), 1/6<301> SF's are invisible (since $2\pi\mathbf{g}\cdot\mathbf{R} = 0$). Figure 5-9 shows a XTEM bright-field image taken with **g** = (-103); all SF's are out of contrast, but residual contrast is nevertheless still observed, which in some cases might be associated with twin-boundary – SF intersections. As seen in planar view, Figure 5-3, twin spacing is ~ 50 nm.

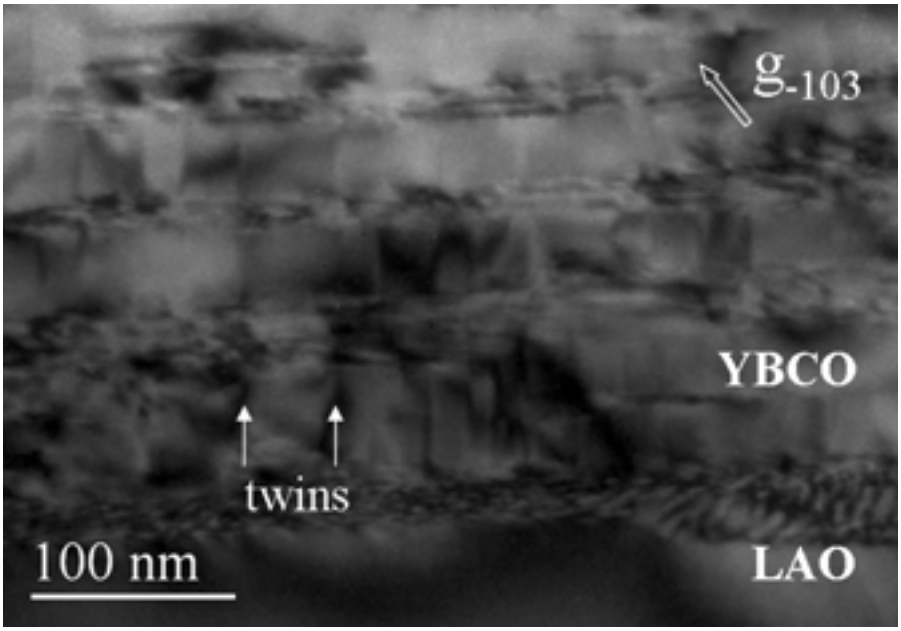

Figure 5-9. XTEM image taken with a diffraction vector **g** = (-103). In this condition SF's are out of contrast.

It is worth mentioning that another type of stacking fault is observed. Figure 5-10 (a) is a cross section HRTEM image taken close to the interface showing, indicated by small arrows, a large number of stacking faults with displacement vector [00*c*/3]. Such type of stacking faults have been reported previously in PLD deposited YBCO films on STO substrates [110]. Extra (Ba-CuO_x) or (Y-CuO) blocks are inserted in the matrix, increasing the c-axis parameter from 11.7 to 15.4 Å, whereas the Y248 SF meant a c-axis growth of 13.3 Å. The size of the faults is variable; near the interface they are larger than those appearing in the upper part of the image, and expand one above the other on every other unit cell (or (001) plane). Figure 5-10 (b) shows an image of the boxed area filtered with spots (*h* 0 *l*), with *h*=0,1 and *l*=0,1,2,3. The filtered image has been highly contrasted in order to emphasize the *c*-axis stacking sequence. Within the squared region, similar *c*[0,0,1/3] faults, but much shorter in length appear stacked along the c-axis. The extra layer is inserted in every unit cell thus generating strong strains which obscure this area in the raw image. Note the lateral overlapping of such faults would generate an inclusion of a distinct phase. Instead, the faults are very short and tend to arrange in a staircase mode, i.e. where one ends on one plane, another begins on the next plane. The present configurations suggest that the interaction of their

stress fields have inhibited their arrangement into a segregated distinct phase. Long faults as those observed close to the interface are probably formed by coalescence of shorter faults. However, the interaction between stress fields of stacking faults on adjacent planes prevents one to expand below another.

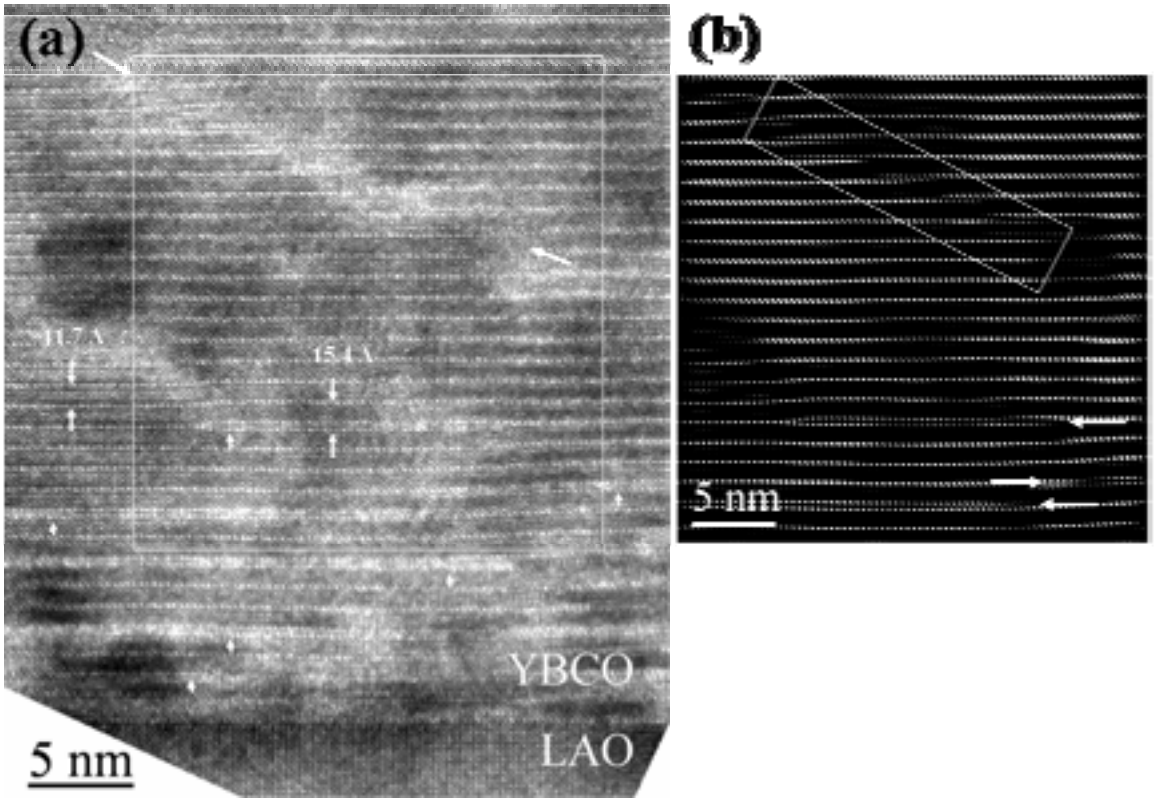

Figure 5-10. (a) High-resolution image of the new SF's structure within YBCO film near the substrate. The change in c-axis lattice constant from 11.7 to 15.4 Å, meaning a perovskite like layer is inserted within YBCO. (b) Filtered image of the (a) boxed area with spots (*h* 0 *l*), with *h*=0,1 and *l*=0,1,2,3.

As we will see further on, SF's may account for the high J_c and has strong influence on the angular dependence of transport J_c in YBCO thin films. Two types of extrinsic and non-stoichiometric SF's have been found in our samples, which are expected to be linked to both stress-related and chemical effects. The genesis of Y248 SF's is well-known and they are found to be a common defect in YBCO matrix [105]. As we will comment below, they are associated with the YBCO decomposition during the oxygenation process and it involves the incorporation of a CuO_x layer within the YBCO matrix [111]. Conversely, SF's resulting from the insertion of an extra

perovskite block are no specifically related to the oxygenation process, but most probably with local stoichiometric deviations.

The formation mechanism of these SF's is discussed on the basis of their observed distribution. Actually, Y248 SF's are inhomogeneously distributed in our TFA-YBCO thin films.

Although the growth of YBCO onto a single crystal yields a high-textured film with a $\Delta\phi = 1.3$ º, we can not overlook that during the growth process, growth fronts of different grains can merge, resulting in a stressed zone along the generated grain boundary [112]. The left-hand side of Figure 5-6 shows the transition from well-ordered region to a highly defective one. No grain boundaries are observed in that sample, but at the same time the density of stacking faults has been found to increase dramatically at particular places. Hence, clustering of stacking faults and dislocations at some regions could be interpreted as a mechanism by which the stress generated at the contact between grains is relieved. The situation may be analogue to the nucleation of SF's at grain boundaries and Y_2BaCuO_5-YBCO interphases in melt-textured materials [101,113]. In this case, however, YBCO nucleates exclusively epitaxailly at the interface, the misorientation between different grains is very small and upon recrystallization most of grain boundaries are likely disappear while the generation of the SF's prevail in the final microstructure because they are thermodynamically stable under the oxygenation conditions. In the previous chapter, chapter 5, we described the conversion of the precursor to YBCO. Our observations revealed that the growth of YBCO is mediated by a long range diffusion within the OF matrix, which also contains Y_2O_3, CuO and $Y_2Cu_2O_5$ grains. That scenario may yield isolated secondary phases inside the YBCO matrix and a non-stoichiometric area at the front growth. Those zones with copper enrichment may provide the excess of CuO needed for Y248 SF's formation. Besides the growth process, it is well known that the YBCO microstructure is modified during the last stage of the YBCO growth process, which consists of an oxygenation step at ~ 600 ºC under flowing oxygen and $P(O_2) = 1$ atm. Under these conditions, Y248 is more stable than the YBCO + CuO mixture. Indeed Y248 is stable below 850 ºC in a 1 atm O_2 [111]. Therefore, at places where the decomposition of the YBCO occurs, the CuO released is likely to diffuse into the YBCO structure forming double CuO layers (Y248). Howover, for temperatures and compositions where there is intimate intermixing of YBCO and Y248 nucleation and growth, it has been claimed

that strain considerations are likely to inhibit ordering of stacking faults into a separate phase [114].

In our samples, the extent of the Y248 SF along the (001) plane varies from few to more than 300 nm, see for instance Figure 5-6 and Figure 5-8 (a). The extent of the SF's might have important implications on the flux pinning; it will be discussed further on.

As was said before, in an image with a diffraction vector such as **g** = (003) all defects with b confined on the (001) plane are invisible. Figure 5-11 is an XTEM bright-field image taken with **g** = (003), in which the large arrow indicates a threading dislocation with **b** // **c**, presumably **b** = 1/3[001], which is energetically more favourable than **b** = [001]. Small arrows indicate SF's. As in Figure 5-8 (a), it shows how Y248 SF's bend the YBCO structure. Variations in the layering are best seen by sighting at a low angle along the fringe direction. (001) fringes in the vicinity of a dislocation are bent to accommodate the extra plane. For an isolated fault this indicates a localized state of compression above and below the fault. In addition, SF's seem to interact with other defects too. In Figure 5-11 it is clearly seen that most of SF's appear punctuated by strain centres indicating that they are intersected or interacting with other defects.

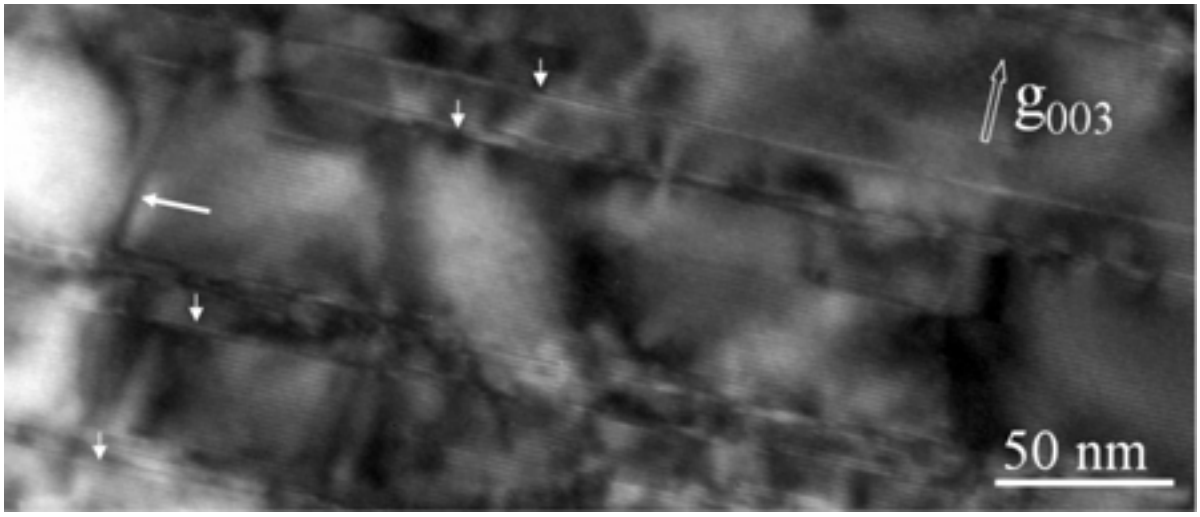

Figure 5-11. High magnification XTEM image taken with a diffraction vector **g** = (003). SF's are are signaled by small arrows, while the large arrow signals a threading dislocation.

Figure 5-12 (a) and (b) shows a pair of cross-sectional bright-field images taken of the same area with **g** = (200) and (003), respectively. The dominant defects are SF's, as well as basal dislocations. However, in Figure 5-12 (a) bent segments of misfit dislocations are seen as dark lines apparently in a direction normal to the substrate surface (indicated by small arrows). Recall that due to the specimen tilting these basal dislocations come into view threading the image. On the other hand, in Figure 5-12 (b) they are out of contrast and in accordance with the **g·b** criteria have Burgers vectors parallel to the film/substrate interface, must probably **b** = [100], [010] or <110>.

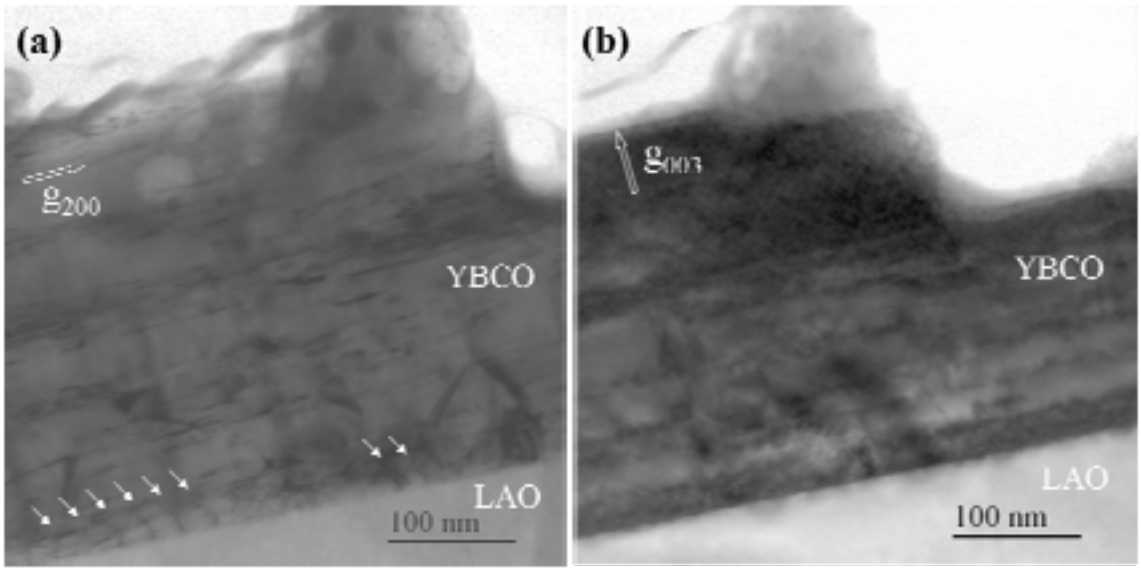

Figure 5-12. Pair of cross-sectional bright field images taken using different diffraction vectors: (a) **g** = (200) and (b) **g** = (003).

According to the classical model of mechanical stress relaxation, the formation of misfit dislocations in a growing film at some critical value of the film thickness gives rise to a partial relaxation of misfit stress between the substrate and the film. Threading dislocations, moving on their glide plane, leave behind an interface misfit dislocation. An edge dislocation with a Burgers vector parallel to the interface contributes to misfit relaxation [115]. Hence, considering a fully relaxed YBCO film, the average distance S between dislocations should be $S = b/\varepsilon$, where b is the Burgers vector of the dislocation and ε is the misfit strain. The contrast behaviour in Figure 5-12 is consistent with **b** = [100] or [110]. In the literature both types have been reported [85,116]. In particular, Jia and co-workers [116] pointed out the existence of two different dislocation

configurations depending on the types of interface (the relative position of the Cu cations with respect to the O sublattice across the interface should be considered). Independently, in our case the strain has a value of 0.017 and the shortest YBCO Burgers vector is ***a***[100], giving a theoretical distance between dislocation of 20 nm, which is close to the average value obtained from Figure 5-12 (a), ~24 nm.

Figure 5-13 is a low magnification XTEM image viewed along the <100> direction showing the YBCO/LAO interface. A large amount of SF's near the interface is clearly seen. Also visible is the contrast variation along the interface. The bright patches are separated 20-25 nm from each other, matching pretty well with the distance between dislocations calculated above. This periodical contrast variation corresponds to a misfit dislocation array, and their separation indicates that the YBCO film is fully relaxed.

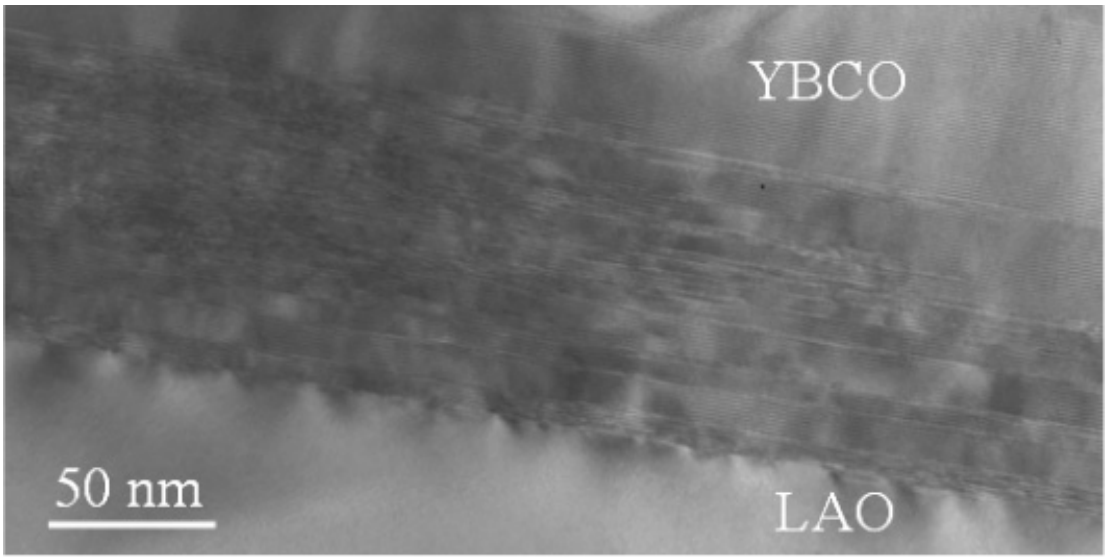

Figure 5-13. Low magnification XTEM image viewed along the <100> direction showing YBCO/LAO interface. Periodical bright patches point out a misfit dislocation array.

The generation of perfect dislocations in TFA-YBCO thin films is discussed in the next section, where three possible formation mechanisms are considered: inheritance of dislocations, creation of half-loops at the film surface and island edge nucleation mechanism.

5.4.3 Generation and evolution of perfect dislocations.

The lattice mismatch between substrate and film induces strain during the growth of YBCO films. Since the elastic strain energy increases with the film thickness, it is expected that this strain is relieved introducing dislocations at the interface above a critical thickness h_c [117]. If dislocations are present in the substrate on which the film is growing, then they grow naturally into the epitaxial film and reach the free surface of the film. This mechanism would yield so called *threading* dislocations. In Figure 5-14 the configuration of a strained layer on a substrate is considered: the biaxial stress in the film exerts forces on the threading dislocations and causes them to move on their slip plane. Thus the threading dislocation in the film bows out as it moves and leaves a misfit dislocation in its wake. However, in our studies on TFA-YBCO films no dislocations and no other defects were found in LAO substrates. Hence, misfit dislocations must be created by some other forms of dislocation nucleation. On the other hand, TEM observations confirmed that the film experienced island nucleation (see previous chapter). The nucleation of islands occurred during the heating. Dislocations could be generated by the creation of half-loops at the surface or near the edges of the islands. It has been suggested that dislocation half-loops created at the film surface glide towards the substrate-film interface to form strain relieving misfit dislocations [118,119]. However, the dislocation distribution presents a fundamental issue; dislocations in YBCO, as well as their dissociated configurations, are confined onto a prominent glide plane (001), even though dislocations lines out of this plane have been also found. Such dislocations either may have left the (001) easy glide plane by climb, or may move on secondary glide planes (100), (010) or {110}[101].This high anisotropy of dislocation configurations is consistent with the anisotropy of the crystal structure, the prominent glide plane corresponding to the largest lattice spacing.

Turning back to the process by which dislocations nucleate in thin films, a basic difficulty arises because very large local stress concentrations are required to overcome the dislocation nucleation barrier. Besides, for surface half-loop nucleation, the stress field must be large enough to expand the loop beyond its critical radius. For instance, thickness nonuniformities or ripples troughs between the islands become stress concentrators, and are thought to be points of dislocation nucleation, providing an explanation for dislocation nucleation in defect-free films [120,121,122]. In particular, Dam and co-workers asserted that in laser-ablated YBCO films dislocations would be

formed at first stages of the growth and close to the substrate/film interface in the form of half-loops at trenches between coherent (dislocation-free) islands. Dislocations would then extend to form misfit dislocations at the interface and persist all the way up to the film surface [86,123].

Chen et al [124] reported the formation of dislocations in $In_xGa_{1-x}As$ layers on a GaAs substrate by means of Frank partial dislocations nucleation at the island edges resulting in SF's that extend during further growth of the island. Similar type of dissociated misfit dislocations in perovskite films on LAO are reported in the literature [125,126,127].

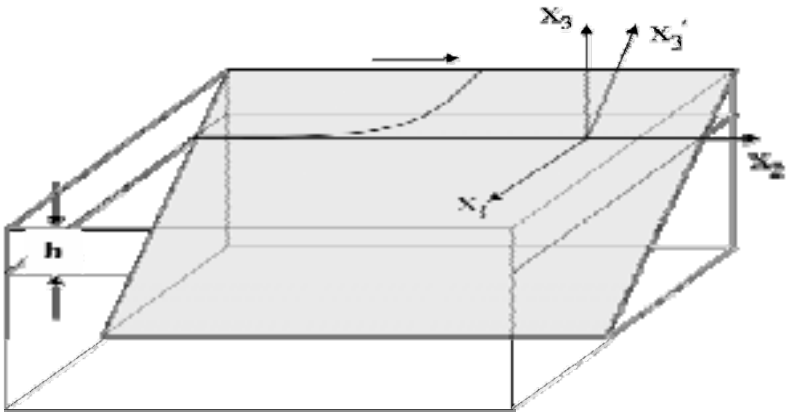

Figure 5-14. Schematic diagram of a threading dislocation progressing along its glide plane, the shaded x_2,x_3' plane, leaving behind an interface misfit dislocation along the x_2 axis. The threading dislocation encounters a stationary interface misfit dislocation lying along the x_1 axis. Modified from [128].

However, the particular nucleation and growth conditions of TFA derived YBCO may provide alternative mechanisms for the formation of perfect dislocations. In this case, the nucleation and growth is assisted by a topotactic transformation of the fluoride type OF phase (see chapter 5). It has been reported that in this scenario, the YBCO phase is formed from a transient cubic perovskite phase [82].Therefore, dislocation nucleated at the edges of such cubic perovskite islands could easily glide on the typical glide planes of the perovskite structure {101} [126,129,130]. In a c-axis oriented perovskite film, the energetically feasible form of the introduction of misfit dislocations is expected to be the glide of pure edge dislocations on {101} slip planes with Burgers vectors of type **a**⟨101⟩ [126,129,130]. The expansion (stages 1-4 in Figure 5-15) of the half-loop is then driven by the release of misfit strain energy by the

dislocation. As the loop radius grows to equal the layer thickness, it begins to form a length AB of misfit dislocation at the film-substrate interface. This misfit dislocation continues to grow until the ends of the dislocation encounter obstacles to further motion. The dislocation of type **a**⟨101⟩ can be dissociated into two interfacial dislocations with Burgers vectors of type **a**⟨100⟩. One would be an edge dislocation with a Burgers vector parallel to the interface and contributes to misfit relaxation. The other would be an edge dislocation with a Burgers vector perpendicular to the interface that does not contribute to misfit relaxation.

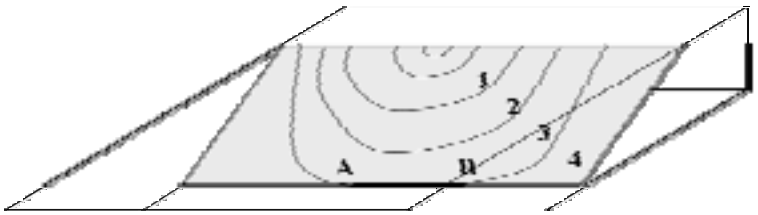

Figure 5-15. Schematics depicting the growth and evolution of a dislocation half-loop in a perovskite film. The growth of half-loops helps to relax the misfit strain. The threading dislocation portion of the half-loops does not contribute to strain relaxation.

The present results do not permit us to get deeper insights into this issue. However, the observation of fully relaxed films suggest that dislocations are introduced at a stage of film nucleation and growth where the anisotropy is not as pronounced as in the orthorhombic phase and glide planes different from (001) are active.

5.5 Implications for vortex pinning

The influence of structural defects found in TFA-YBCO thin films on the critical currents is a complex problem because it is difficult to isolate the effect of a single kind of defect on the experimental J_c. In fact, the mutual interactions between defects or their competing effects on the critical currents may hinder a unique identification of their corresponding relevance in the pinning process. Besides, it is far beyond the scope of this thesis to identify the nature and the effectiveness of every possible pinning site in

TFA-YBCO thin films. Our aim, in the present section, will be to briefly discuss the possible implication of the observed microstructure on the measured critical current density.

Twin boundaries are the most commonly observed defects in YBCO. The twin boundaries are shown to consist of thin (~1 nm) structurally disordered and oxygen-hole depleted regions [131]. Thus, the boundaries are likely to influence the values of J_c in these films. The effectiveness of twin boundaries as pinning centers when the Lorentz force cross the {110} planes was first demonstrated by magnetoresistance measurements [132], using single crystals in which the twin boundaries were uni-directionally oriented. These experiments showed that planar boundaries could be strong pinning sites when the flux lines were pushed against the boundaries, while they could act as *channels* for easy flux motion when the Lorentz force is directed along the boundary planes. Besides, our TFA-YBCO thin films present different twin orientation within YBCO grains, which leads a large number of crossing points that might represent a pinning center. However, the relevance of these defects in the critical currents of YBCO thin films has been found to be relatively small [133].

The numerous SF's observed and defect structures associated with them have dimensions which are appropriate for flux pinning. The SF's can be viewed as disk of additional non-superconducting material with diameters ranging from a few to ~ 300 nm. The dislocations bounding the stacking faults may also be considered as pinning centers. SF's constitute an excellent correlated defect in the <100> direction, thus acting as linear-like pinning center when the applied magnetic field (H) is parallel to ab-plane. However, as was said above, the effectiveness of a planar defect will depend on the motion of the vortices due to the Lorentz force. For H//c, pinning of the flux line would occur primarily at the circumferential region defined by the dislocation loop bounding the fault. The strength of pinning would depend on the pinned length of the flux line and in this case that may correspond to the extent of crystal lattice strain along the c direction, acting, as a result, as a point-like pinning center. These considerations indicate that the smaller the size of the SF, the larger its efficiency as flux pinning center [134]. Besides, it would be very appealing to investigate how the different defects around SF's interact among themselves. If we consider an area with a vertical clustering of SF's, such as observed in a previous section, the vortex will, therefore, be pinned over a large length in the c direction.

Due to their dimensionality (nearly one dimensional) dislocations seem to be ideal for magnetic-flux lines [86,123]. Indeed, experiments on miscut [91] and bicrystal [92] substrates indicated the importance of the dislocation pinning in films. Based on the measurement of the densities of the threading dislocations in PLD films and their correlation with J_c at low temperatures, it was claimed that these dislocations were the primary pinning center contributing to the high current densities in these films [86]. However, the nucleation and growth mechanisms for TFA-YBCO films are very different from those in PLD processed YBCO films; indeed, in YBCO, dislocations, as well as their dissociated configurations, are mostly confined onto a prominent glide plane, (001). Dislocations lining out of this plane are hardly encountered in our TEM studies, which could explain the different J_c versus H_c behavior between PLD and TFA processed YBCO films.

5.6 Conclusions

Thin films of the high-temperature superconductor YBCO exhibit both a large critical current ($4 \cdot 10^6$ Acm^{-2} at 77 K) and a dependence on magnetic field that point to the importance of strong vortex pinning along extended defects [86]. Such pinning centers are provided by structural defects within the superconductor, and are formed under non-equilibrium conditions during the film growth. Our present work has revealed that TFA-YBCO thin films present a very rich defect microstructure, both in the plane and out of the plane: twin boundaries, twin intersections, stacking faults, twin boundaries-stacking faults intersections, threading and basal dislocations.

It is well known that twin boundaries are intimately associated with orthorhombic YBCO; they are formed as the result of a tetragonal-to-orthorhombic structural phase transformation during the oxygenation process of YBCO. The twin spacing in TFA-YBCO thin films is significantly smaller than that found in melt-textured composites, which is consistent with the idea that the twin spacing is controlled by the dimension of YBCO grains. In addition, the two twin orientations are typically observed within the same grain.

SF's consisting of an extra Cu-O_x layer are also found to be common defects in the YBCO matrix but our results show that they are inhomogeneously distributed. The

observed clustering of Y248 SF's at some regions is interpreted as a mechanism with which to accommodate the stress built where the growth fronts of two islands meet. Furthermore, these zones are those which would allow the incorporation of Cu in excess from the Cu-rich precursor areas. Furthermore, another type of SF's has been found. It consist in the intercalation of a perovskite like layer, an extra (Ba-CuO_x) or (Y-CuO) block, in the YBCO structure. The genesis of such SF is not known and deserves more investigation.

The observation of fully relaxed films refers to the generation of misfit dislocations, which seem to be introduced at a stage of nucleation and growth where a less anisotropic transient cubic perovskite phase assist the early nucleation stage of YBCO.

Our TEM observations show that dislocations lining out of (001) plane are hardly encountered in our TEM studies, in contrast with PLD films [86].

CHAPTER 6
ARTIFICIAL DEFECTS IN TFA-YBCO THIN FILMS

Chapter Preview

The introduction of a secondary phase ($BaZrO_3$) into the superconducting TFA-YBCO matrix has increased the vortex pinning efficiency. TEM observations show that these $BaZrO_3$ nanoparticles are randomly distributed inside the YBCO matrix. Some of these nanoparticles nucleate directly at the interface with the substrate, exhibiting epitaxy, while those that nucleate into the bulk are mostly randomly oriented.

6.1 Introduction

Columnar defects introduced by irradiation with very energetic heavy ions are the most effective pinning centres for flux lines in YBCO superconductors. This correlated disorder has been shown to reduce vortex mobility and to increase the critical current density, J_c [84], but it is impractical for scaling-up due to its cost and because it yields a radioactive metallic substrate. The simulation of these defects is a promising approach. Up to now, there have been some recent developments in creating *in situ* pinning sites, i.e. tailored defects resulting from modifying the growth conditions of the films (as opposed to having a separate *ex situ* step such as heavy-ion irradiation). Examples of this include rare-earth doping [135], self-assembling of precipitates [136], and multilayering [137]. So far, however, the reported work deals mainly with PLD films, and there are no reports of this kind on films made by TFA processing. Such films are of interest as they could help to decrease production costs of coated conductors [14].

Our group has proved that chemical solution deposition is a suitable technique to fabricate very high J_c nanocomposites of YBCO and $BaZrO_3$ (BZO). The addition of BZO to YBCO has several advantages: (1) although it can grow heteroepitaxially with YBCO, it has a large mismatch (9%), so strain between phases could introduce defects. (2) It is a high-melting-temperature phase and hence its growth kinetics should be slow, leading to small particles. (3) Zr or ZrO_2 has not detrimental effect on the superconducting properties of YBCO [138].

In this chapter, after briefly presenting the variations in pinning properties induced by the addition of BZO nanoparticles to the YBCO, we address the microstructure of such nanocomposites.

6.2 Experimental procedure

The precursor solution has been modified before deposition [139]. The idea is quite simple, merely to add an excess of Ba and Zr salts. Besides, an excess of Y is added in order to compensate the formation of a solid solution between BZO and Y_2O_3 [140].

The solution preparation consisted of the dissolution of a small quantity (between 2 and 5 % in weight) of acetylacetonate of Zr, and an equivalent amount of $Ba(TFA)_2$ and $Y(TFA)_3$ in the standard precursor solution of trifluoracetates, resulting something like:

$$(1+y)Y(TFA)_3 + (2+x)\ Ba(TFA)_2 + 3\ Cu(TFA)_2 + x\ Zr(acetylacetonate)_4$$

This modified solution has been deposited by spin coating onto (00l)-STO substrate, and submitted to the standard growth process described in chapter 4.

The desired nanoparticles appear during growth as natural secondary phases. The optimization of this approach is still under investigation. Here, it will be reported our preliminary results.

The effect of BZO particles on YBCO thin films has been identified by TEM and Z-contrast STEM and X-ray analysis. Transport critical current densities were measured using the four-point probe method by other researchers in our group [35].

6.3 Critical current measurements

The critical current density, J_c, in the case of the YBCO+BZO film grown on STO substrate, has a value of ~ $6 \cdot 10^6$ Acm^{-2} at 77 K. The magnetic field dependence of the critical current density at 77 K of two TFA-YBCO nanocomposite films with a BZO nanoparticles (in red and in green) are shown in Figure 6-1. For comparison the results for a standard TFA-YBCO film grown (in black) in the same conditions are also plotted. These results evidenced the enhancement of the vortex pinning properties of the doped samples. The improvement of the J_c (H) in the whole range of measured fields is manifested in doped samples. For example, at 77 K and 1 T the current density has been improved by a factor of 6. Hence, the BZO addition has clearly increased the irreversibility filed, (H_{irr}(at 77 K) = 9 T).

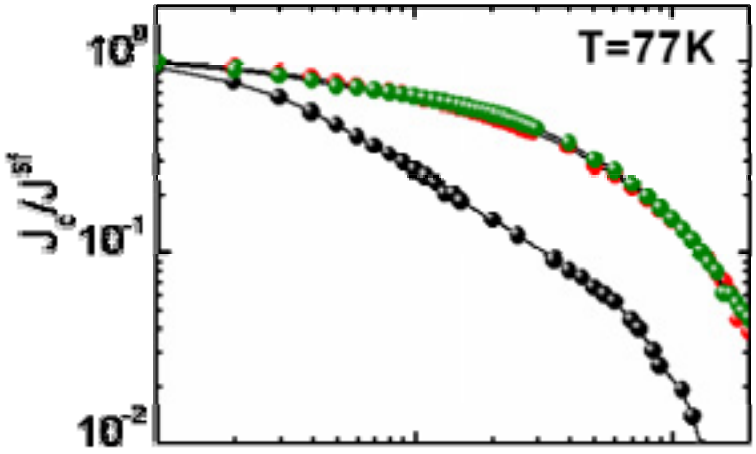

Figure 6-1. A log-log representation of the critical current density at 77 K versus magnetic field for an undoped TFA-film (black) and for two TFA-YBCO films with BZO nanoparticles (red and green).

Figure 6-2 shows the angular dependence of J_c measured in a field of 1 T at 77 K for two samples. An upwards shift in all the angular range is observed for YBCO+BZO compared with the pure YBCO, indicative of vortex pinning controlled by isotropic defects, i.e. an overall enhancement of J_c with a closely isotropic J_c curve is observed for YBCO+BZO film. Indeed, the contribution of anisotropic defects parallel to c-axis is not relevant, which is in contrast with physical growth methods [141,136]. The scarcely existence of any peak for orientations about the direction of the c-axis shows that there is no correlation or preferential direction for the pinning or, therefore, of the pinning defects themselves. The previous result is important for applications of coated conductors, because the magnetic field will rarely be constrained to a single orientation.

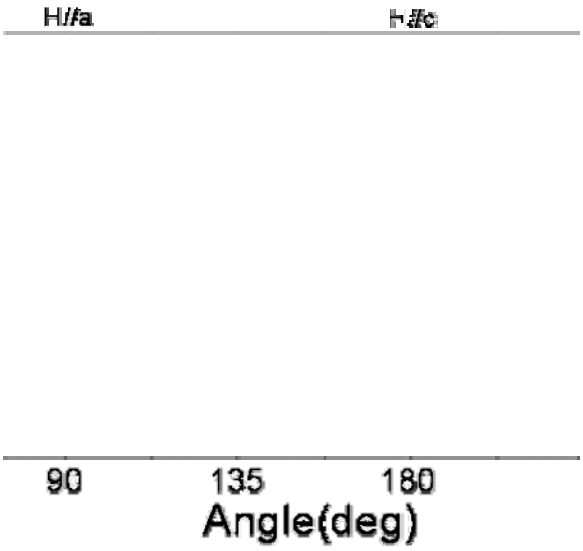

Figure 6-2. Transport current density, J_c, measured for a standard TFA-YBCO film (in green) and for a TFA-YBCO-BZO film as a function of θ at 77 K, for applied field of $\mu_0 H = 1$ T (in red).

6.4 Microstructure analysis results

In this section, we address the study of the microstructure of such a nanocomposite film onto a STO substrate. It represents the first attempt to elucidate the role of BZO nanoparticles in the enhancement of the vortex pinning properties of the doped samples.

Figure 6-3 (a) shows a conventional θ-2θ scan of a BZO added YBCO film deposited on STO, showing intense YBCO (00*l*) peaks indicating that the YBCO film has a strong c-axis texture, plus an additional peak centered around $2\theta = 42.7º$, which is consistent with the (200)BZO. The breadth and position of this second peak suggest that BZO forms a solid solution with Y, which has been already reported in the literature [140]. Nevertheless, it will be referred to as BZO, despite of its possible Y content. Careful inspection of the XRD pattern also reveals a broad peak at a 2θ value of 29.9º which corresponds to the BZO (101) reflection, Figure 6-3 (b). As we will see below this reflection might be considered as a random fraction of BZO particles.

Figure 6-3. (a) $\theta/2\theta$ XRD pattern of YBCO and BZO particles on STO. (b) Amplification of the $\theta/2\theta$ XRD pattern of YBCO and BZO particles on STO.

In order to obtain an average picture of the texture of the BZO phase, a pole-figure was recorded for a 2θ value of 29.9º, which corresponds to the (101) reflection of the BZO. The resulting pole-figure, shown in Figure 6-4, exhibits four equivalent {101}BZO poles at inclination of χ = 45º. These poles appear superposed to a ring of intensity that could be attributed to a fiber texture fraction. Nevertheless, this is a consequence of taking a small interval of χ-scanning angle. Hence, this result must not be considered a fiber texture fraction but a disordered fraction of BZO.

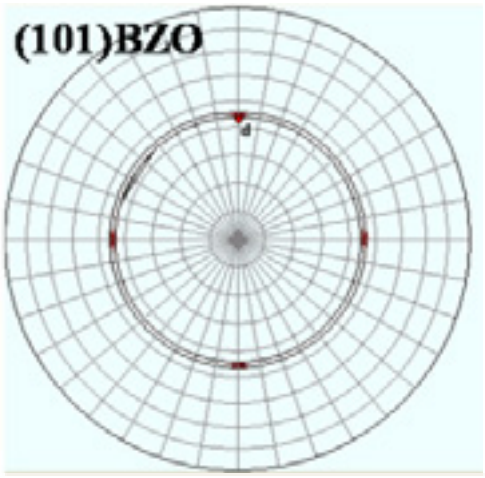

Figure 6-4. Pole-figure corresponding to the (101) BZO reflection.

TEM analysis reveals that BZO nanodots are found uniformly distributed within the 250 nm-thick YBCO matrix and onto the substrate surface, as observed in the low resolution TEM image, shown in Figure 6-5. The image was taken with the sample slightly tilted in order to better visualize the BZO particles. We would like to accurately discern the size and distribution of BZO into the YBCO matrix. However, we note that TEM images provide a two-dimensional section of particles embedded through-out the three-dimensional foil volume, and so the three-dimensional distribution of particles is not yet precisely known. Nevertheless, the measured two-dimensional number density of nanoparticles in Figure 6-5 is ~2.2×10^{10} particles/cm^2. It can also be observed that BZO nanodots are mainly round-shaped, being variable in size (10 -30 nm) and separated by about 20-100 nm.

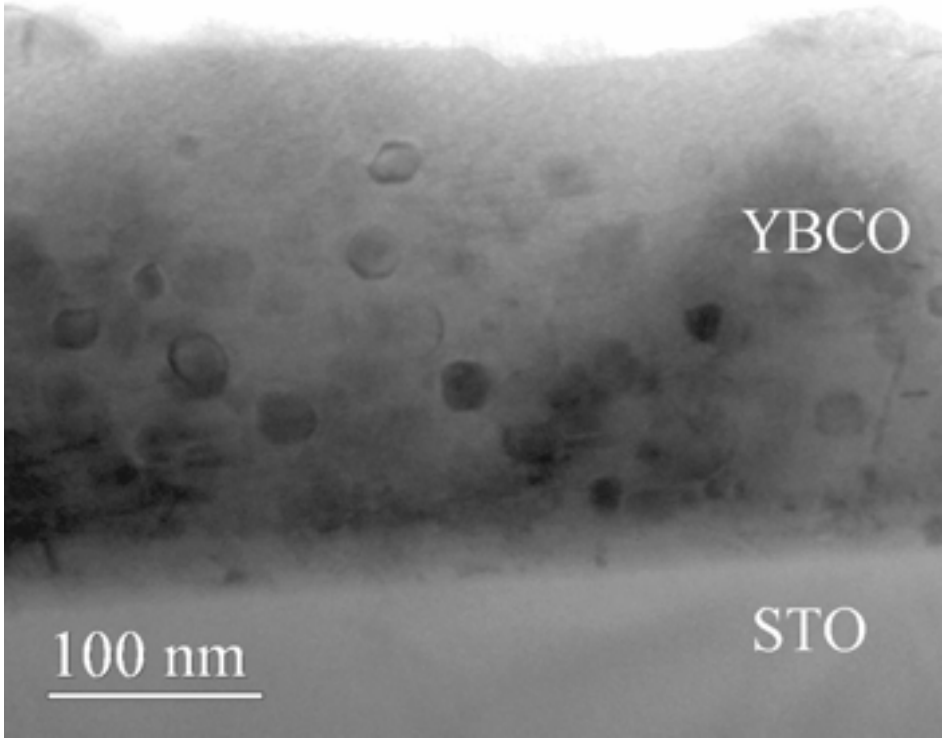

Figure 6-5. XTEM image viewed along the <100> direction of YBCO+BZO film. Nanoparticles are clearly discernible, with sizes ranging between 10-30 nm.

The particle size was also estimated from x-ray diffraction 2θ-scans using the Scherrer formula, $t = 0.9\lambda/(\Delta\theta\cos\theta_B)$, which relates $\Delta\theta$, the FWHM of the diffraction peak at $2\theta_B$, with the average size t of the particles [33]. This yields sizes of 14 nm and

26 nm for (200) and (110) reflections respectively, which are consistent with those found from TEM studies.

In the previous image, Figure 6-5, due to the tilt of the foil, the number of particles onto the substrate was not easily appreciated. Z-contrast imaging allows us to discern the distribution of BZO particles within the YBCO matrix and those at the film/substrate interface. The *Z*-contrast image is formed by collecting the electrons scattered out to high angles on a high-angle annular dark field (HAADF) detector. The underlying physical principle is that high *Z* atoms scatter to higher angles more strongly than lighter atoms. In the limit of Rutherford scattering, this goes as Z^2, so the contrast in the image will also vary approximately as Z^2. Thus, for Z-contrast imaging technique, the lighter atomic elements show up darker, while the heavier elements show an enhanced (brighter) contrast. The atomic number of Y, Ba, Cu and Zr are 39, 56, 29, and 40 respectively. Hence, the BZO nanoparticles exhibit brighter contrast. Furthermore, in our diffraction conditions, the BF image shows the Y248 SF's brighter than the Z-contrast image, which shows them up darker. Figure 6-6 (a) and (b) are cross sectional low magnification STEM bright field (BF) and Z-contrast images viewed along the <100> direction from the YBCO+BZO film, respectively. It is important to remark that nanocomposite films present a uniform distribution of the Y248 SF's as a dominant microstructural feature, besides the BZO nanoparticles, contrasting with the standard TFA-YBCO thin films, where the Y248 SF's were found inhomogeneously distributed. Hence, it suggests that their presence and uniform distribution are related to BZO nanoparticles. The formation of such Y248 SF's will be discussed further on.

It is also remarkable the large number of BZO particles grown onto the substrate surface, which do not seem to have any detrimental effect in the crystalline quality of YBCO. The measured two-dimensional number density of nanoparticles in Figure 6-6 coincides with the previous results, as well as the average size of the BZO nanoparticles.

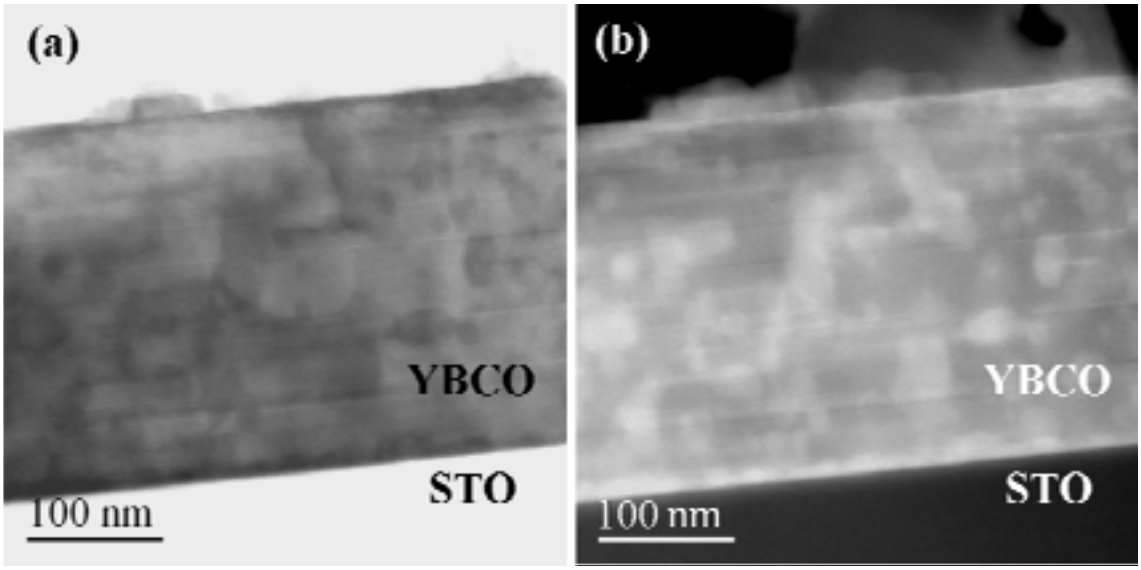

Figure 6-6. (a) and (b) cross-section bright field and Z-contrast STEM image taken along <100> direction, respectively.

It is noteworthy the long bright streaks shown and identified by arrows in Figure 6-7, which is an amplification image of the Z-contrast image Figure 6-6 (b). These streaks have been found mainly lying on the ab-planes, which might indicate the formation of Zr-rich perovskite blocks inserted in the YBCO matrix, namely $BaZrO_x$, preferably along the [100] directions. Indeed, similar extra perovskite blocks have already reported in the previous chapter. These structural defects may be introduced during growth and their directional selective segregation may be attributed to the anisotropic growth rate of YBCO in a/b-direction [68]. In addition, in some cases these streaks run near Y248 SF's. Thought the choice of BZO partially resulted from the fact that several researchers established the chemical inertia of this material towards a YBCO-Y_2BaCuO_5 melt composition [142,143,138], the precise influence of BZO on the growth of YBCO thin films is still lacking and deserves a further investigation.

In this figure, Figure 6-7, besides the BZO nanoparticles themselves, extended changing contrast areas are observed, which would be a sign of strain fields in the YBCO lattice around the particles.

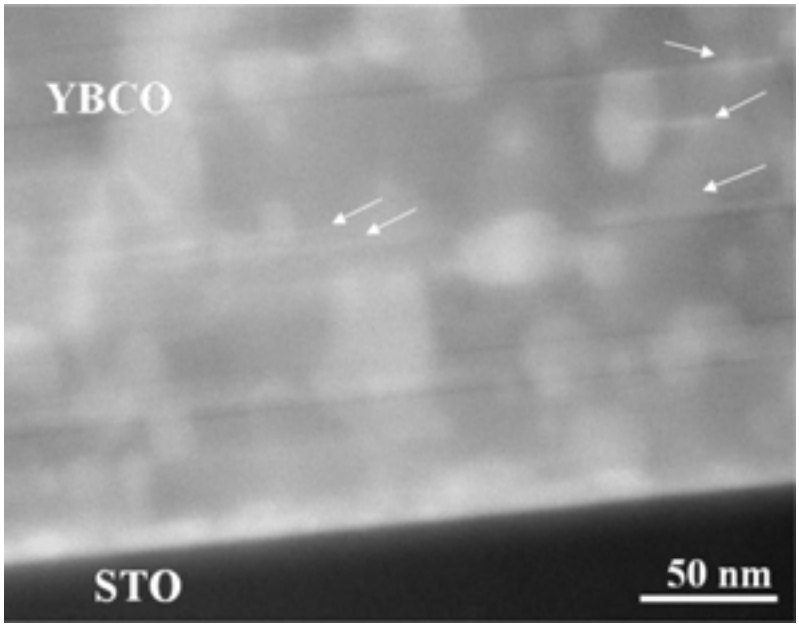

Figure 6-7. Z-contrast STEM image taken along <100> direction. The long bright streaks are identified by arrows.

Turning back to the issue concerning the orientation of BZO particles, TEM observations confirmed that the BZO had indeed grown in the form of nanodots and that part of them were coherent with the YBCO matrix and part not. Concerning those coherent with YBCO orientation, two HRTEM images viewed along the <100> direction showing the YBCO/STO interface, Figure 6-8 (a) and (b), are presented. They show BZO particles onto the substrate surface having different morphology and size, ranging from 10 to 15 nm. Figure 6-8 (a) shows a BZO particle with the *c*-axis parallel to the YBCO and STO *c*-axes, while the [100] axis of BZO lies parallel to the YBCO *a* or *b* directions, as clearly seen in the FFT of the same area (Figure 6-8 (a) inset). In Figure 6-8 (b), the BZO particle does not wet the substrate and presents a slight misalignment.

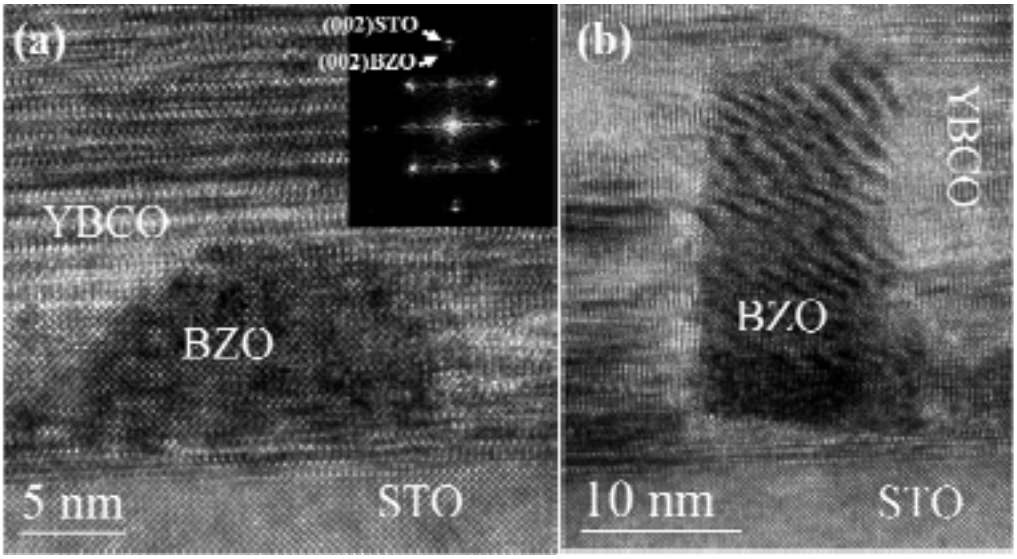

Figure 6-8. Cross-section high resolution images of an YBCO+BZO/STO interface. (a) Rounded BZO particle showing a perfect alignment with YBCO and STO. Inset: FFT of this are. (b) Rectangular BZO particle.

Occasionally, c-aligned extended defects emanate from BZO particles. Figure 6-9 is a HRTEM image taken at the YBCO/STO interface. The image reveals extended defect along c-axis coming from the BZO particle and threading the YBCO matrix. The extended defect exists only up to a length of about 20 nm, indicating that such threading defect may run out of the plane of the foil.

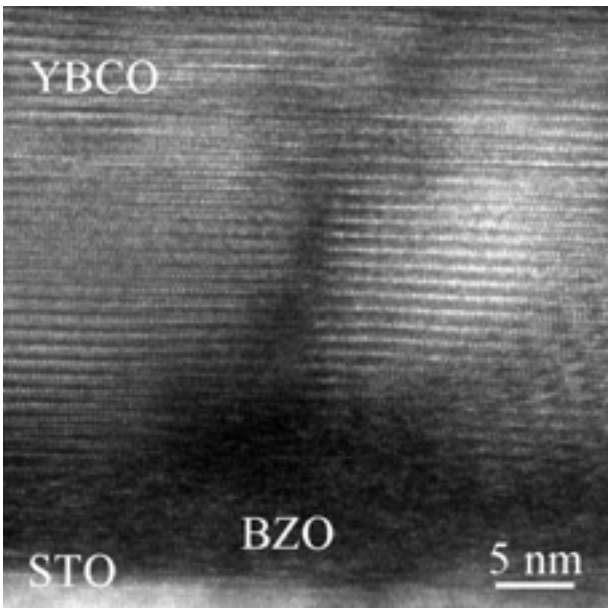

Figure 6-9. High resolution TEM image showing a c-aligned extended defect coming from the BZO nanoparticle.

The cube-on-cube relationship is only maintained near the YBCO/STO interface, while within the bulk BZO nanodots do not exhibit a clear alignment with YBCO. A HRTEM image from the bulk viewed along <100> direction, Figure 6-10 (a) shows a misoriented BZO grain embedded in the YBCO matrix. The inset presents the FFT obtained from the BZO particle and the adjacent area. The BZO {110} reflections have been marked with circles while the YBCO (001) peak has been signaled with a white arrow, showing that BZO {110} reflections are not coherent with YBCO. Figure 6-10 (b) is an EELS spectra obtained from the nanodot exhibiting the M-Zr peak. More misoriented grains were found, and their size was variable, ranging between 10 and 30 nm, as was stated above.

Figure 6-10 (a) reveals a strongly disturbed YBCO lattice around BZO nanodots, with large number of staking disorder generated around them. The periodicity of the CuO planes (visible as bright lines) are frequently interrupted, shifted vertically or even slightly bent.

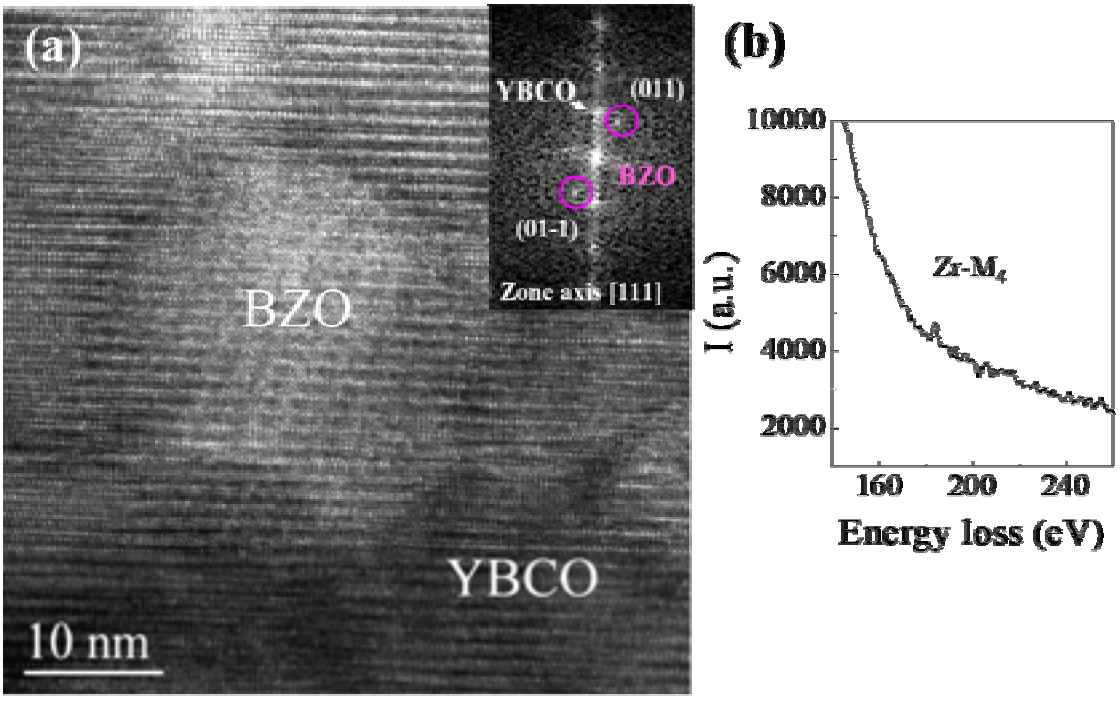

Figure 6-10. (a) High resolution TEM image showing a non-coherent BZO nanoparticle. Inset: FFT of the same area. (b) EELS spectra obtained from BZO nanodot revealing the M-Zr peak.

As was discussed previously, the TEM sample preparation of such thin films plays a critical role. The ion beam used for milling might be quite aggressive in its attack on the sample, introducing artifacts. Figure 6-11 (a) and (b) shows HRTEM image of a BZO particle and its corresponding FFT, respectively. That BZO nanodot is surrounded by a YBCO matrix full of defects, in contrast with the previous HRTEM image, Figure 6-10 (a).

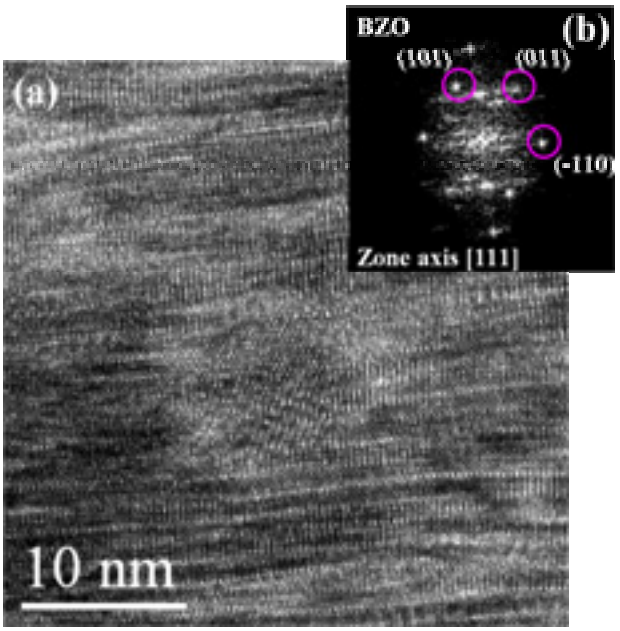

Figure 6-11. (a) High resolution TEM image showing a non-coherent BZO nanoparticle. Inset: FFT of the same area. (b) Corresponding FFT.

Occasionally, the coalescence of BZO particles is observed, but their density is much reduced as compared to the isolated ones. Figure 6-12 shows a XTEM image of two coalesced BZO nanoparticles, roughly ellipticcal in shape, embedded within a defective YBCO matrix, which is in turn distorted and bended. Both BZO nanoparticles are not coherent neither with YBCO nor between themselves. The zone enclosed by the BZO particles and the dashed lines appears to be highly defective, much more than outside this region. This might suggest that BZO nanoparticles were nucleated within the precursor matrix before the YBCO formation.

Actually, to uncover the mechanism by which these BZO nanoparticles are formed, we must address the YBCO growth process. The presence of water vapour at sufficiently high temperature causes the decomposition of the oxyfluoride, which allows the nucleation of both YBCO and BZO phases. The temperature required for conversion

exceeds 700 ºC. Actually, the thermal processing conditions used to grow these samples are the most favorable ones to grow an epitaxial YBCO film; at the same time, due to the large undercooling they promote the bulk and the heterogeneous nucleation of BZO simultaneously. Those grains that nucleate near the interface become epitaxial, while those that nucleate within the YBCO precursor are randomly oriented. In addition, it is well known that the critical radius r* is the same for both homogeneous and heterogeneous nucleation. However, due to the shape factor, the volume of a critical nucleus can be significantly smaller, which may explain the difference in size of BZO particles nucleated onto the substrate and those nucleated within the bulk [112]. Although the growth process at 795 ºC can induce the grain growth, the subsequent rapid growth of YBCO might avoid the Ostwald ripening of BZO particles, which may explain the homogeneous size distribution of the BZO naoparticles within the YBCO matrix.

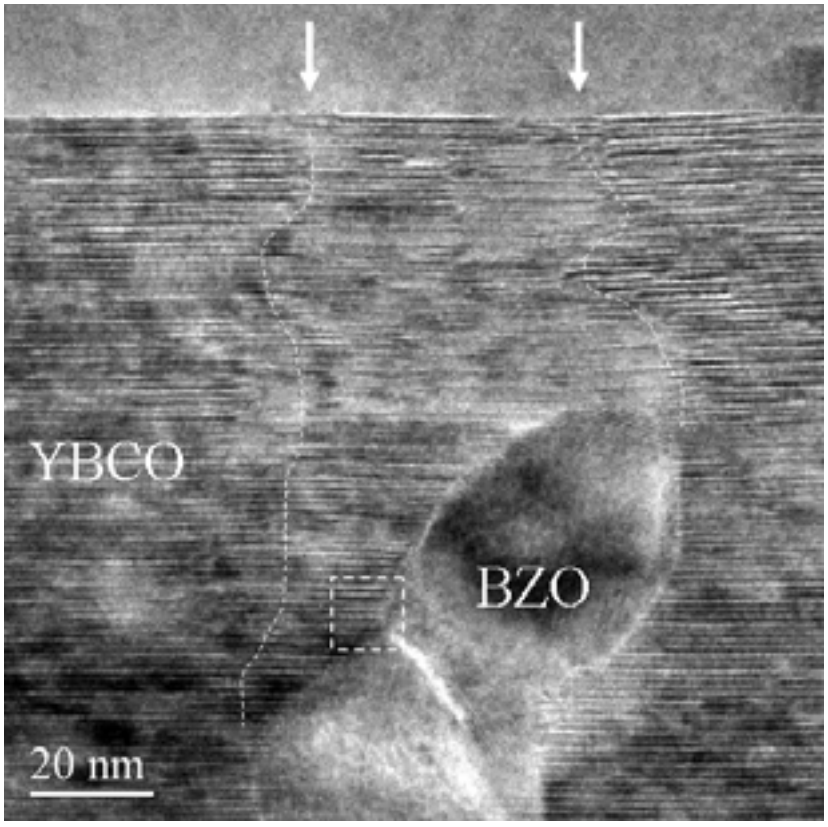

Figure 6-12. XTEM image viewed along the <100> direction of YBCO+BZO film. Nanoparticles are clearly discenible, as well as the defective zone above them.

As it was discussed above, the distribution of SF's is strongly modified by the presence of BZO addition, which yields to a homogeneous distribution, in contrast with the standard TFA-YBCO thin films. In investigating the faulted structures of these nanocomposites, it was found numerous SF's at the interface between BZO nanoparticles and YBCO. Figure 6-13 is a HRTEM image of the zone signalled by a dashed square of the former image, Figure 6-12. White arrows signalled SF's generated on the YBCO/BZO interface. The measurement of the unit cell height in the c-direction match the Y248 lattice parameter, 13.3 Å [105].

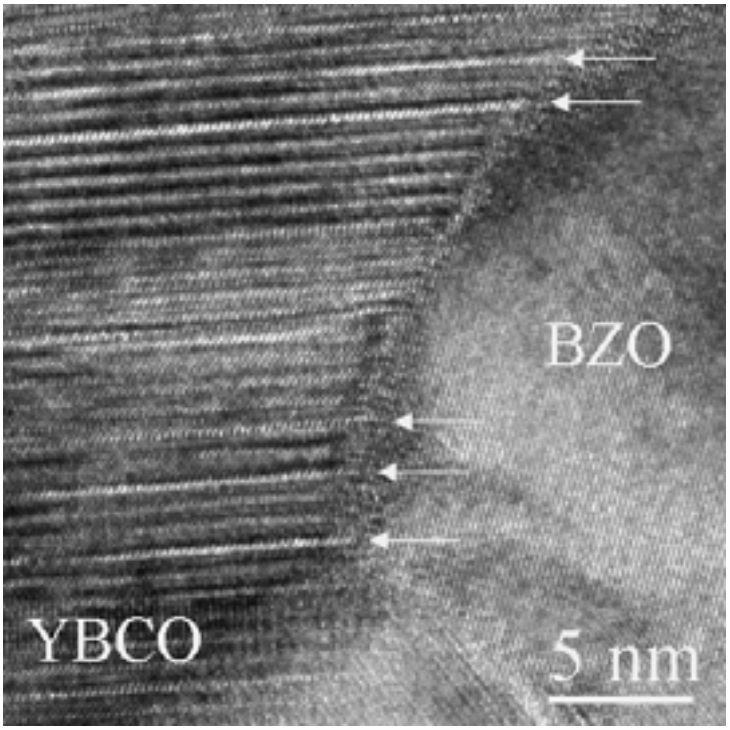

Figure 6-13. High-resolution image of the YBCO/BZO interface. The Y248 srtructures are arrowed.

The formation of Cu-O extrinsic SF requires the availability of Cu in excess relative to the YBCO stoichiometry. This could be reached, al least, by two processes which would take place during the oxygenation process of YBCO. The first one is associated with the already mentioned formation of a solid solution between BZO and Y_2O_3. Even if an excess of Y is added in the precursor solution in order to compensate the formation of such a solid solution, the phase segregation inherent to the TFA processing can lead to a Cu-O excess in some areas, near the BZO particles, for instance. The CuO released is likely to diffuse into the YBCO structure forming double CuO_x layers at random depths of the film. On the other hand, Zhang and Evetts

described chemical reactions between YBCO and ZrO_2 resulting in the formation of BZO, Y_2BaCuO_5 (211) and CuO phases [144]. However, our analyses reveal no formation of 211 and CuO phases but BZO solid solution. Hence, the excess of Cu produced from the interfacial reactions could reinforce the Y248 SF's formation.

Besides, the formation of Y248 SF's is also expected to be linked to stress-related effects due to the misfit strain between YBCO and BZO. Indeed, BZO nanoparticles were though to act as stressors inducing extended defects such as threading dislocations due to misfit strain. However, BZO particles can induce a tensile stress that facilitates the intercalation of double CuO_x layers, being analogue to the nucleation of Y248 SF's at Y_2BaCuO_5-YBCO interphases in melt-textured materials [101,113].

6.5 Conclusions

Chemical solution growth is a very flexible methodology to nanostructure YBCO films. BZO nucleates heterogeneously and homogenously within YBCO precursor matrix. Their growth is frozen during YBCO growth process, leading to 10-30 nm-sized particles. Detailed TEM analysis shows that BZO nanoparticles grow epitaxially onto the substrate surface and randomly oriented within the YBCO matrix. The distribution of SF's is strongly modified by the presence of BZO addition, which yields to a homogeneous distribution. However, the density of faulted structures can dramatically increase around some particles. Transport measurements showed a shift upwards in all the angular range for YBCO+BZO composites compared with the pure YBCO, indicative of vortex pinning controlled by isotropic defects. In fact, the contribution of anisotropic defects parallel to c-axis is not relevant, in contrast with PLD films [145,136]. Thus, our observations suggest indeed that the strain introduced into the matrix yields to a homogeneous distribution of defects. Such homogeneous collection of defects could act as isotropic point-like pinning centers. The identification of such defects and the nature of their pinning mechanism deserve further investigation.

GENERAL CONCLUSIONS

The goal of this thesis has been to investigate the specifics of CSD processed CeO_2 buffer and YBCO layers. The superconducting properties strongly depend on the microstructure of these films, which is intimately tied to their particular fabrication process and it will determine their applicability as coated conductor.

In chapter 3 it was observed that MOD-derived CeO_2 under reducing atmospheres promoted the trapping of carbon impurities at the ceria grain boundaries. These impurities inhibit the ceria (001) epitaxial development, resulting in randomly oriented grains at the surface, preventing any further YBCO epitaxial growth. Once the carbon impurities are removed by thermal post-processing at 1000 ºC under oxidizing conditions the granular regime is suppressed. This result pointed out the necessity of increasing the grain boundary mobility. The Gd dopant provides free oxygen vacancies to the host cations thus enhancing the grain boundary mobility. The effect of Gd on grain boundary mobility of CeO_2 depends on the concentration and growth conditions. An almost fully epitaxial layer can be achieved by doping ceria with 10% Gd and growing it at 900 ºC under Ar/5%H_2 atmosphere. In spite of the overall roughness of the Gd-doped ceria (~4.7 nm), governed by the formation of facetted hillocks, its terraced surface with atomically flat areas corresponding to (001) planes, provided suitable sites for YBCO nucleation and growth. The doped ceria is processed under reducing atmosphere condition, thereof avoiding undesirable substrate oxidation.

A superconducting TFA-derived YBCO film with a J_c (77 K) up to 10^6 A/cm^2 was achieved on top of the MOD-derived Gd-CeO_2 buffer layer, despite of the massive transformation of the Gd-ceria buffer to (Gd)$BaCeO_3$ observed all along the interface. No evidence of YBCO deterioration was observed, which suggest that it results not from the reaction between the precursor and Gd-CeO_2 but between YBCO and Gd-CeO_2.

In chapter 4 we addressed crystallization of YBCO. After the pyrolysis, simultaneously with the disappearance of the organic content, a BYF matrix with embedded CuO nanoparticles is formed. Upon heating, the microstructural evolution of the precursor is driven by the reduction of the solid solubility of Y in the BYF solid

solution. Thus, Y is released in the form of Y_2O_3 which can react with CuO to form $Y_2Cu_2O_5$ at ~700 ºC, i.e., close to the YBCO nucleation temperature. At 795 ºC, EELS analyses of the matrix reveal significant oxygen content and only a weak signal of Y. No traces of BaO are detected at any stage of the process, thus reinforcing the view that YBCO forms by a diffusive topotactic-like mechanism within the OF matrix. We have not found any conclusive microstructural evidence supporting the formation of partial melts during the process.

Besides the evolution of the fluoride/oxyfluoride type matrix, the microstructural evolution of the precursor film is characterized by coarsening of the CuO particles and the formation of $Y_2Cu_2O_5$ in the bulk matrix. In particular, the formation of this latter oxide is particularly relevant because it occurs at temperatures very close to the epitaxial nucleation of YBCO, and therefore both processes may constitute competitive phenomena thereof affecting the kinetics of the conversion process.

The present work supports that (111) oriented OF domains provide low barrier nucleation sites on the buried substrate surface. Surprisingly, however, such regions only represent about 15% of the total OF matrix. It is not clear, at present, whether under operating supersaturation conditions, initial nucleation of YBCO is restricted to such regions or, on the contrary, the supersaturation is too large to make nucleation sensitive to barrier differences associated with the different environments found on the substrate surface. In this context, anomalously large distances between nuclei found in this system would support a preferential affinity for the nucleation on low barrier (111) oriented OF domains.

The high critical current densities exhibited by YBCO thin films bear on the strong vortex pinning along extended defects. In chapter 4 we addressed the identification of such defects. TFA-YBCO thin films present different types of correlated disorders, among which are twin boundaries, twin intersections, stacking faults, twin boundaries-stacking faults intersections, threading and basal dislocations. Among them, the predominant extended defects are stacking faults as well as twin boundaries.

The influence of structural defects found in TFA-YBCO thin films on the critical currents is a complex problem because it is difficult to isolate the effect of a single kind of defect on the experimental J_c.

TFA-YBCO samples are twined in the two directions, with the existence of many twin intersection areas within YBCO grains, giving place to a large number of crossing points that might represent a pinning center, i.e. twin planes in YBCO are significant source of correlated disorder, both in and out of plane.

Two types of SF's have been found in our YFA-YBCO films. Y248 SF's constitute a prominent defect in TFA-YBCO thin films and consists of a double Cu-O chain layer. The formation mechanism of these SF's was discussed on the basis of their observed distribution. The observed clustering of Y248 SF's at some regions is interpreted as a mechanism with which to accommodate the lattice stresses where growth fronts meet. Furthermore, these zones are those which would allow the incorporation of Cu in excess from the Cu-rich precursor areas.

The second type of SF's found in our TFA-YBCO films consist of the intercalation of a perovskite like layer, an extra (Ba-CuO_x) or (Y-CuO) block, in the YBCO structure. The genesis of such SF is not known and deserves more investigation.

Dislocations do also enhance the flux pinning, indeed due to their dimensionality they seem to be ideal for magnetic-flux lines. In YBCO dislocations, as well as their dissociated configurations, are confined onto a prominent glide plane, (001). Dislocations lining out of this plane are hardly encountered in our TEM studies, which could explain the different J_c versus H_c behavior between PLD and TFA processed YBCO films. Moreover oxyfluoride mediated solid phase epitaxy favors a layered growth in contrast with vacuum deposition.

During YBCO growth the lattice mismatch between substrate and film causes strain which is relaxed via dislocation nucleation. The observation of fully relaxed films refers to the generation of misfit dislocations, which seem to be introduced at a stage of nucleation and growth where a transient cubic perovskite phase active glide planes different than (001) plane, characteristic of the YBCO compound. In particular, in a c-axis oriented perovskite films, the energetically feasible form of the introduction of misfit dislocations is expected to be the glide of pure edge dislocations on {101} slip planes with Burgers vectors of type a⟨101⟩.

In chapter 5 we showed that chemical solution growth is a very flexible methodology to nanostructure YBCO films. Studies of magnetic field dependence of the critical current density showed an increase of the irreversibility line for YBCO+BZO thin films versus *undoped* YBCO thin films. TEM observations of the nanocomposites

films show that the BZO nucleates heterogeneously and homogenously within YBCO precursor matrix. Their growth is frozen during YBCO growth process, leading to 10-30-sized particles. Detailed x-rays and TEM analysis show that BZO nanoparticles grow epitaxially onto the substrate surface and randomly oriented within the YBCO matrix. The distribution of Y248 SF's is strongly modified by the presence of BZO addition. In contrast with the standard TFA-YBCO thin films the distribution of the SF's are now homogeneous. Besides, the density of faulted structures can dramatically increase around some particles.

TABLE OF THE OBSERVED PHASES

Phase	Structure	Cell parameters (Å)
$BaCeO_3$	Pseudocubic	4.38
YSZ	Cubic, fluorite	5.16
NiO	Cubic, rock-salt	4.17
$BaCeO_3$	Tetragonal	a = 6.212 c = 8.804
	Pseudocubic	a =4.380
$BaCuO_2$	Cubic (Im3m)	a = 18.285
BaF_2	Cubic (Fm3m)	a = 6.200
BaO	Cubic (Fm3m)	a = 5.355
$BaZrO_3$	Cubic (P23)	a = 4.181
CeO_2	Cubic (Fm3m)	5.411
CuO	Monoclinic (C2/c)	a = 4.688 b = 3.422 c = 5.131
CuO_2	Cubic (Pn3m)	a = 4.269
$LaAlO_3$	Rhombohedral (R3m)	a = 5.364 c = 13.110
	Pseudocubic	a = 3.792
$SrTiO_3$	Cubic (Pm3m)	a = 3.905
$Y_2Cu_2O_5$	Orthorhombic (Pna2l)	a = 10.799 b = 3.496 c = 12.456
Y_2O_3	Cubic (Ia3)	a = 10.604
$YBa_2Cu_3O_6$	Tetragonal (P4/mmm)	a = 3.857 c = 11.839
$YBa_2Cu_3O_7$	Orthorhombic (Pmmm)	a = 3.886 b = 3.818 c = 11.680
YSZ	Cubic (Fm3m)	a = 5.160

REFERENCES

1. Waldram J.R., "Superconductivity of Metals and Cuprates" Institute of Physics Publishing (1996).

2. M.A.Beno, L.Soderholm, D.W.Capone, D.G.Hinks, J.D.Jorgensen, J.D.Grace, I.K.Schuller, C.U.Segre, and K.Zhang, "Structure of the Single-Phase High-Temperature Superconductor $YBa_2Cu_3O_{7-\delta}$" Applied Physics Letters, **51**, 57 (1987).

3. D.Larbalestier, A.Gurevich, D.M.Feldmann, and A.Polyanskii, "High-T-c superconducting materials for electric power applications" Nature, **414**, 368 (2001).

4. A.Usoskin, J.Dzick, A.Issaev, J.Knoke, F.Garcia-Moreno, K.Sturm, and H.C.Freyhardt, "Critical currents in long-length YBCO-coated conductors" Superconductor Science & Technology, **14**, 676 (2001).

5. J.Knauf, R.Semerad, W.Prusseit, B.DeBoer, and J.Eickemeyer, "YBaCuO - deposition on metal tape substrates" Ieee Transactions on Applied Superconductivity, **11**, 2885 (2001).

6. B.Utz, S.RiederZecha, and H.Kinder, "Continuous $YBa_2Cu_3O_{7-\delta}$ film deposition by optically controlled reactive thermal co-evaporation" Ieee Transactions on Applied Superconductivity, **7**, 1181 (1997).

7. H.Yamane, T.Hirai, K.Watanabe, N.Kobayashi, Y.Muto, M.Hasei, and H.Kurosawa, "Preparation of A High-J_c Y-Ba-Cu-O Film at 700 ºC by Thermal Chemical Vapor-Deposition" Journal of Applied Physics, **69**, 7948 (1991).

8. Y.Yamada, T.Suga, and I.Hirabayashi, "Low-temperature growth conditions of $YBa_2Cu_3O_{7-\delta}$ using Ba-Cu-Ag-O-F solvent" Journal of Crystal Growth, **236**, 221 (2002).

9. P.M.Mankiewich, J.H.Scofield, W.J.Skocpol, R.E.Howard, A.H.Dayem, and E.Good, "Reproducible Technique for Fabrication of Thin-Films of High Transition-Temperature Superconductors" Applied Physics Letters, **51**, 1753 (1987).

10. V.F.Solovyov, H.J.Wiesmann, L.J.Wu, Y.M.Zhu, and M.Suenaga, "Kinetics of $YBa_2Cu_3O_7$ film growth by postdeposition processing" Applied Physics Letters, **76**, 1911 (2000).

11. T.Kumagai, H.Yamasaki, K.Endo, T.Manabe, H.Niino, T.Tsunoda, W.Kondo, and S.Mizuta, "Critical-Current Densities at 77-K in $Ba_2YCu_3O_{7-Y}$-Ag Films Prepared by Dipping-Pyrolysis Process" Japanese Journal of Applied Physics Part 2-Letters, **32**, L1602 (1993).

12. T.Manabe, I.Yamaguchi, S.Nakamura, W.Kondo, T.Kumagai, and S.Mizuta, "Crystallization and Inplane Alignment Behavior of $YBa_2Cu_3O_{7-y}$ Films on Mgo(001) Prepared by the Dipping-Pyrolysis Process" Journal of Materials Research, **10**, 1635 (1995).

13. P.C.Mcintyre, M.J.Cima, and M.F.Ng, "Metalorganic Deposition of High-J_c $Ba_2YCu_3O_{7-X}$ Thin-Films from Trifluoroacetate Precursors Onto (100) $SrTiO_3$" Journal of Applied Physics, **68**, 4183 (1990).

14. X.Obradors, T.Puig, A.Pomar, F.Sandiumenge, N.Mestres, M.Coll, A.Cavallaro, N.Roma, J.Gazquez, J.C.Gonzalez, O.Castano, J.Gutierrez, A.Palau, K.Zalamova, S.Morlens, A.Hassini, M.Gibert, S.Ricart, J.M.Moreto, S.Pinol, D.Isfort, and J.Bock, "Progress towards all-chemical superconducting $YBa_2Cu_3O_7$-coated conductors" Superconductor Science & Technology, **19**, S13 (2006).

15. K.Yamagiwa, T.Araki, Y.Takahashi, H.Hiei, S.B.Kim, K.Matsumoto, J.Shibata, T.Hirayama, H.Ikuta, U.Mizutani, and I.Hirabayashi, "Epitaxial growth of $REBa_2Cu_3O_{7-y}$ films on various substrates by chemical solution deposition" Journal of Crystal Growth, **229**, 353 (2001).

16. D.P.Norton, "Epitaxial $YBa_2Cu_3O_7$ on biaxially textured nickel (001): An approach to superconducting tapes with high critical current density" Science, **274**, 755-757 (1996).

17. G.Brinker and G.W.Scherer, "Sol-Gel Science: The Physics and Chemistry of Sol-Gel Processing" , New York (Academic) (1990).

18. J.D.Mackenzie and E.Bescher, "Some factors governing the coating of organic polymers by sol-gel derived hybrid materials" Journal of Sol-Gel Science and Technology, **27**, 7 (2003).

19. K.T.Miller, C.J.Chan, M.G.Cain, and F.F.Lange, "Epitaxial Zirconia Thin-Films from Aqueous Precursors" Journal of Materials Research, **8**, 169 (1993).

20. A.Gupta, R.Jagannathan, E.I.Cooper, E.A.Giess, J.I.Landman, and B.W.Hussey, "Superconducting Oxide-Films with High Transition-Temperature Prepared from Metal Trifluoroacetate Precursors" Applied Physics Letters, **52**, 2077 (1988).

21. R.Roy, "Gel Route to Homogeneous Glass Preparation" Journal of The American Ceramics Society, **52**, 344 (1969).

22. R.W.Schwartz, "Chemical Solution Deposition of Perovskite Thin Films" Chem . Mater., **9**, 2335 (1997).

23. C.V.Thompson, "Grain growth in thin films" Annu. Rev. Mater. Sci., **20**, 45-68 (1999).

24. Chiang Yet-Ming, Birnie III Dunbar, and Kingery W.David, "Physical Ceramics, Principles for Ceramic Science and Engineering" John Wiley and Sons, MIT, New York

25. J.W.Cahn, "Impurity-Drag Effect in Grain Boundary Motion" Acta Metallurgica, **10**, 789 (1962).

26. Williams D.B. and Carter C.B., "Transmission Electron Microscopy. A Textbook for Materials Science" Plenum Press. New York (1996).

27. von Heimendahl M., "Electron Microscopy of Materials" Academic Press. New York (1980).

28. Watt I.M., "The Principles and Practice of Electron Microscopy" Cambridge University Press. New York (1985).

29. Egerton R.F., "Electron Energy Loss Spectroscopy in the Electron Microscope" 2nd Editon, Plenum Press. New York (1996).

30. O'Connor D.J., Sexton B.A., and Smart R.St.C., "Surface Analysis Methods in Materials Science" 2nd Edition. Springer. New York (2003).

31. Wiesendanger R., "Scanning Probe Microscopy and Spectroscopy. Methods and Applications" Cambridge University Press. New York (1998).

32. Willey VCH, "Scanning Probe Microscopy and Spectroscopy. Theory, Techniques and Applications" 2nd Edition. Ed. Dawn Bonnell. New York (2001).

33. Cullity B.D., "Elements of X-Ray Diffraction" Addison-Wesley, London (1978).

34. Hammond C., "The Basics of Crystallography and Diffraction" 2nd Edition. Oxford University Press. New York (2006).

35. J.Gutierrez, "Ancoratge de Vòrtexs en Cintes Superconductores i Capes Monocrsital·lines de $YBa_2Cu_3O_{7-x}$" PhD. Tesina, Universitat Autònoma de Barcelona, ICMAB, Spain (2006).

36. Y.A.Boikov, T.Claeson, D.Erts, F.Bridges, and Z.Kvitky, "CeO_2 compatibility with $YBa_2Cu_3O_{7-\delta}$ in superconducting film multilayers" Phys. Rev. B, **56**, 11312

37. A.Cavallaro, "Optimization of MOD-CeO_2 buffer layers for $YBa_2Cu_3O_7$ coated conductor development" PhD. Thesis, Universitat Autònoma de Barcelona, ICMAB, Spain (2005).

38. M.Coll, "Chemical Solution Deposition of oxide buffers and superconducting layers for $YBa_2Cu_3O_7$ coated conductors" PhD. Thesis, Universitat Autònoma de Barcelona, ICMAB, Spain (2006).

39. A.Cavallaro, F.Sandiumenge, J.Gazquez, T.Puig, X.Obradors, J.Arbiol, and H.C.Freyhardt, "Growth mechanism, microstructure, and surface modification of nanostructured CeO2 films by chemical solution deposition" Advanced Functional Materials, **16**, 1363 (2006).

40. M.Spanková, I.Vávra, S.Gazi, D.Machajdik, S.Chromik, K.Fröhlich, L.Hellemans, and S.Benacka, "Growth and recrystallization of CeO_2 thin films deposited on R-plane sapphire by off-axis sputtering" J. Crysrt. Growth, **218**, 278-293 (2000).

41. S.N.Jacobsen, L.D.Madsen, and U.Helmersson, "Epitaxial cerium oxide buffer layers and $YBa_2Cu_3O_{7-\delta}$ thin films for microwave device applications" Journal of Materials Research, **14**, 2385 (1999).

42. Cardarelli F., "Materials Handbook" Springer, London (2000).

43. I.A.Ovid'ko, "Misfit dislocation walls in solid films" Journal of Physics-Condensed Matter, **11**, 6521 (1999).

44. I.A.Ovid'ko and A.G.Sheinerman, "Grain-boundary dislocations and enhanced diffusion in nanocrystalline bulk materials and films" Philosophical Magazine, **83**, 1551 (2003).

45. C.Noguera, "Polar oxide surfaces" Journal of Physics-Condensed Matter, **12**, R367 (2000).

46. G.S.Herman, "Characterization of surface defects on epitaxial CeO_2(001) films" Surface Science, **437**, 207 (1999).

47. T.X.T.Sayle, S.C.Parker, and C.R.A.Catlow, "The role of oxygen vacancies on ceria surfaces in the oxidation of carbon monoxide" Surf. Sci., **316**, 329-336 (1994).

48. S.N.Jacobsen, U.Helmersson, R.Erlandsson, B.Skarman, and L.R.Wallenberg, "Sharp microfaceting of (001)-oriented cerium dioxide thin films and the effect of annealing on surface morphology" Surface Science, **429**, 22 (1999).

49. P.L.Chen and I.W.Chen, "Role of Defect Interaction in Boundary Mobility and Cation Diffusivity of CeO_2" Journal of the American Ceramic Society, **77**, 2289 (1994).

50. P.L.Chen and I.W.Chen, "Grain growth in CeO_2: Dopant effects, defect mechanism, and solute drag" Journal of the American Ceramic Society, **79**, 1793 (1996).

51. Kilner S.B. and Steele B.C.H., "*Nonstoichiometric Oxides*" O. T. Sorensen Editor, Academic Press. New York, **p. 233** (1981).

52. B.C.H.Steele and Floyid J.M., "Oxygen self-diffusion and electrical transport properties of nonstoichiometric ceria and ceria solid solution" Proc. Brit. Ceram. Soc., **19** (1971).

53. P.Knappe and L.Eyring, "Preparation and Electron-Microscopy of Intermediate Phases in the Interval Ce7O12-Ce11O20" Journal of Solid State Chemistry, **58**, 312 (1985).

54. M.Flytzani-Stephanopoulos, "Nanostructured cerium oxide "ecocatalysts"" Mrs Bulletin, **26**, 885 (2001).

55. A.Trovarelli, "Catalytic properties of ceria and CeO_2-containing materials" Catalysis Reviews-Science and Engineering, **38**, 439 (1996).

56. E.P.Murray, T.Tsai, and S.A.Barnett, "A direct-methane fuel cell with a ceria-based anode" Nature, **400**, 649 (1999).

57. B.C.H.Steele, "Appraisal of $Ce_{1-y}Gd_yO_{2-y/2}$ electrolytes for IT-SOFC operation at 500 ºC" Solid State Ionics, **129**, 95 (2000).

58. S.R.Wang, H.Inaba, H.Tagawa, M.Dokiya, and T.Hashimoto, "Nonstoichiometry of $Ce_{0.9}Gd_{0.1}O_{1.95-x}$" Solid State Ionics, **107**, 73 (1998).

59. M.Mogensen, N.M.Sammes, and G.A.Tompsett, "Physical, chemical and electrochemical properties of pure and doped ceria" Solid State Ionics, **129**, 63 (2000).

60. Humphreys F.J.and Hetherly M., "Recrystallization and Related Annealing Phenomena" Pergamon, Oxford (1995).

61. N.L.Wu, S.Y.Wang, and I.A.Rusakova, "Inhibition of crystallite growth in the sol-gel synthesis of nanocrystalline metal oxides 4" Science, **285**, 1375 (1999).

62. P.C.Mcintyre, M.J.Cima, J.A.Smith, R.B.Hallock, M.P.Siegal, and J.M.Phillips, "Effect of Growth-Conditions on the Properties and Morphology of Chemically Derived Epitaxial Thin-Films of $Ba_2YCu_3O_{7-X}$ on (001) $LaAlO_3$" Journal of Applied Physics, **71**, 1868 (1992).

63. J.A.Smith, M.J.Cima, and N.Sonnenberg, "High critical current density thick MOD-derived YBCO films" Ieee Transactions on Applied Superconductivity, **9**, 1531 (1999).

64. J.Shibata, T.Honjo, H.Fuji, T.Araki, I.Hirabayashi, T.Hirayama, T.Izumi, Y.Shiohara, T.Yamamoto, and Y.Ikuhara, "Crystallization mechanism of $Nd_{1+x},Ba_{2-x}Cu_3O_{7-y}$ and $YBa_2Cu_3O_{7-y}$ films deposited by metalorganic deposition method using trifluoroacetates" Journal of Materials Research, **17**, 1266 (2002).

65. M.Yoshizumi, I.Seleznev, and M.J.Cima, "Reactions of oxyfluoride precursors for the preparation of barium yttrium cuprate films" Physica C, **403**, 191 (2004).

66. B.P.Sobolev and N.L.Tkachenko, "Phase diagrams of BaF_2-$(Y,Ln)F_3$ systems" Journal of the Less-Common Metals, **85**, 155-170 (1982).

67. P.C.Mcintyre and M.J.Cima, "Heteroepitaxial Growth of Chemically Derived Ex-Situ $Ba_2YCu_3O_{7-X}$ Thin-Films" Journal of Materials Research, **9**, 2219 (1994).

68. S.F.Karmanenko, "Influence of growth rate on the structural orientation of YBCO superconducting films" Superconductor Science & Technology, **12**, 36 (1999).

69. V.F.Solovyov, H.J.Wiesmann, and M.Suenaga, "Growth rate limiting mechanisms of $YBa_2Cu_3O_7$ films manufactured by ex situ processing" Physica C, **353**, 14 (2001).

70. V.F.Solovyov, H.J.Wiesmann, L.J.Wu, Y.Zhu, and M.Suenaga, "Ex-situ post-deposition processing for large area $YBa_2Cu_3O_7$ films and coated tapes" Ieee Transactions on Applied Superconductivity, **11**, 2939 (2001).

71. T.Puig, J.C.Gonzalez, A.Pomar, N.Mestres, O.Castano, M.Coll, J.Gazquez, F.Sandiumenge, S.Pinol, and X.Obradors, "The influence of growth conditions on the microstructure and critical currents of TFA-MOD $YBa_2Cu_3O_7$ films" Superconductor Science & Technology, **18**, 1141 (2005).

72. L.Wu, Y.Zhu, V.F.Solovyov, H.J.Wiesmann, A.R.Moodenbaugh, R.L.Sabatini, and M.Suenaga, "Nucleation and growth of $YBa_2Cu_3O_{7-x}$ on $SrTiO_3$ and CeO_2 by a BaF_2 postdeposition reaction process" Journal of Materials Research, **16**, 2869 (2001).

73. T.Ohnishi, R.H.Hammond, and W.Jo, "High rate in situ $YBa_2Cu_3O_7$ film growth assisted by liquid phase" Journal of Materials Research, **19**, 977 (2004).

74. W.Wong-Ng, L.P.Cook, J.Suh, I.Levin, M.Vaudin, M.Vaudin, R.Feenst, and J.P.Cline, Material Research Society Symposium, Boston MA, **689**, 337 (2002).

75. T.Honjo, Y.Nakamura, R.Teranishi, Y.Tokunaga, H.Fuji, J.Shibata, S.Asada, T.Izumi, Y.Shiohara, Y.Iijima, T.Saitoh, A.Kaneko, and K.Murata, "Fabrication and growth mechanism of YBCO coated conductors by TFA-MOD process" Physica C, **392**, 873 (2003).

76. J.C.Gonzalez, "Coeated Conductors and Chemical Solution Growth of YBCO Films: A Micro-Raman Spectroscopy Study" PhD. Thesis, Universitat Autònoma de Barcelona, ICMAB, Spain (2005).

77. Shannon, R. D. Acta Cryst. A, **32**, 751 (1976).

78. M.Suenaga, "BaF_2 processes for $YBa_2Cu_3O_7$ conductors, promises and challenges" Physica C, **378-381**, 1045 (2002).

79. M.J.Cima, Fall meeting, Material Research Society Symposium, Boston MA (2002).

80. W.Wong-Ng, I.Levin, R.Feenstra, L.P.Cook, and M.Vaudin, "Phase evolution of $Ba_2YCu_3O_{6+x}$ films during the BaF_2 process" Superconductor Science & Technology, **17**, S548 (2004).

81. Maffott W.G., "Handbook of Binary Phase Diagrams" Gerium, Achenectady. New York (1999).

82. L.Wu, V.F.Solovyov, H.J.Wiesmann, Y.Zhu, and M.Suenaga, "Mechanisms for hetero-epitaxial nucleation of $YBa_2Cu_3O_{6.1}$ at the buried precursor/$SrTiO_3$ interface in the postdeposition reaction process" Applied Physics Letters, **80**, 419 (2002).

83. M.Murakami, K.Yamaguchi, H.Fujimoto, N.Nakamura, T.Taguchi, N.Koshizuka, and S.Tanaka, "Flux Pinning by Nonsuperconducting Inclusions in Melt-Processed YBCO Superconductors" Cryogenics, **32**, 930 (1992).

84. L.Civale, A.D.Marwick, T.K.Worthington, M.A.Kirk, J.R.Thompson, L.Krusinelbaum, Y.Sun, J.R.Clem, and F.Holtzberg, "Vortex Confinement by Columnar Defects in $YBa_2Cu_3O_7$ Crystals - Enhanced Pinning at High Fields and Temperatures" Physical Review Letters, **67**, 648 (1991).

85. J.Rabier and M.F.Denanot, "Dislocation Mirror-Twin-Boundary Interactions in $YBa_2Cu_3O_{7-\delta}$" Philosophical Magazine A-Physics of Condensed Matter Structure Defects and Mechanical Properties, **65**, 427 (1992).

86. B.Dam, J.M.Huijbregtse, F.C.Klaassen, R.C.F.van der Geest, G.Doornbos, J.H.Rector, A.M.Testa, S.Freisem, J.C.Martinez, B.Stauble-Pumpin, and R.Griessen, "Origin of high critical currents in $YBa_2Cu_3O_{7-\delta}$ superconducting thin films" Nature, **399**, 439 (1999).

87. J.Mannhart, D.Anselmetti, J.G.Bednorz, A.Catana, C.Gerber, K.A.Muller, and D.G.Schlom, "Correlation Between Jc and Screw Dislocation Density in Sputtered $YBa_2Cu_3O_{7-\delta}$ Films" Zeitschrift fur Physik B-Condensed Matter, **86**, 177 (1992).

88. V.M.Pan, A.L.Kasatkin, V.L.Svetchnikov, and H.W.Zandbergen, "Dislocation Model of Superconducting Transport-Properties of YBCO Thin-Films and Single-Crystals" Cryogenics, **33**, 21 (1993).

89. C.Gerber, D.Anselmetti, J.G.Bednorz, J.Mannhart, and D.G.Schlom, "Screw Dislocations in High-Tc Films" Nature, **350**, 279 (1991).

90. M.Hawley, I.D.Raistrick, J.G.Beery, and R.J.Houlton, "Growth-Mechanism of Sputtered Films of $YBa_2Cu_3O_7$ Studied by Scanning Tunneling Microscopy" Science, **251**, 1587 (1991).

91. D.H.Lowndes, D.K.Christen, C.E.Klabunde, Z.L.Wang, D.M.Kroeger, J.D.Budai, S.Zhu, and D.P.Norton, "Strong, Asymmetric Flux-Pinning by Miscut-Growth-Initiated Columnar Defects in Epitaxial $YBa_2Cu_3O_{7-X}$ Films" Physical Review Letters, **74**, 2355 (1995).

92. A.Diaz, L.Mechin, P.Berghuis, and J.E.Evetts, "Evidence for vortex pinning by dislocations in $YBa_2Cu_3O_{7-\delta}$ low-angle grain boundaries" Physical Review Letters, **80**, 3855 (1998).

93. N.Roma, S.Morlens, S.Ricart, K.Zalamova, J.M.Moreto, A.Pomar, T.Puig, and X.Obradors, "Acid anhydrides: a simple route to highly pure organometallic solutions for superconducting films" Superconductor Science & Technology, **19**, 521 (2006).

94. K.Zalamova, N.Roma, A.Pomar, S.Morlens, T.Puig, J.Gazquez, Sandiumenge F, Carrillo A.E., S.Ricart, and Obradors X., "Stress Relief control of Trifluoroacetate metal-organic solutions for YBCO film growth" Chem . Mater. (2006).

95. K.J.Leonard, A.Goyal, D.M.Kroeger, J.W.Jones, S.Kang, N.Rutter, M.Paranthaman, D.F.Lee, and B.W.Kang, "Thickness dependence of microstructure and critical current density of $YBa_2Cu_3O_{7-\delta}$ on rolling-assisted biaxially textured substrates" Journal of Materials Research, **18**, 1109 (2003).

96. L.Civale, B.Maiorov, A.Serquis, J.O.Willis, J.Y.Coulter, H.Wang, Q.X.Jia, P.N.Arendt, J.L.Manus-Driscoll, M.P.Maley, and S.R.Foltyn, "Angular-dependent vortex pinning mechanisms in $YBa_2Cu_3O_7$ coated conductors and thin films" Applied Physics Letters, **84**, 2121 (2004).

97. L.Civale, B.Maiorov, J.L.Manus-Driscoll, H.Wang, T.G.Holesinger, S.R.Foltyn, A.Serquis, and R.N.Arendt, "Identification of intrinsic ab-plane pinning in $YBa_2Cu_3O_7$ thin films and coated conductors" Ieee Transactions on Applied Superconductivity, **15**, 2808 (2005).

98. D.R.Nelson and V.M.Vinokur, "Boson Localization and Correlated Pinning of Superconducting Vortex Arrays" Physical Review B, **48**, 13060 (1993).

99. T.K.Worthington, W.J.Gallagher, D.L.Kaiser, F.H.Holtzberg, and T.R.Dinger, "The Anisotropic Nature of the Superconducting Properties of Single-Crystal $YBa_2Cu_3O_{7-X}$" Physica C, **153**, 32 (1988).

100. B.Roas, L.Schultz, and G.Saemannischenko, "Anisotropy of the Critical Current-Density in Epitaxial $YBa_2Cu_3O_x$ Films" Physical Review Letters, **64**, 479 (1990).

101. F.Sandiumenge and J.Rabier, "Studies of High Temperature Superconductors" Ed. Narlikar, Nova Science, New York, **Vol. 28**, p. 43 (1999).

102. F.Sandiumenge, S.Pinol, X.Obradors, E.Snoeck, and C.Roucau, "Microstructure of Directionally Solidified High-Critical-Current $YBa_2Cu_3O_7$-Y_2BaCuO_5 Composites" Physical Review B, **50**, 7032 (1994).

103. Z.L.Wang, A.Goyal, and D.M.Kroeger, "Structural and Chemical Disorder Near the $Y_2BaCuO_5/YBa_2Cu_3O_{7-\delta}$ Interface and Its Possible Relation to the

Flux-Pinning Behavior in Melt-Textured $YBa_2Cu_3O_{7-\delta}$" Physical Review B, **47**, 5373 (1993).

104. S.K.Streiffer, E.M.Zielinski, B.M.Lairson, and J.C.Bravman, "Thickness Dependence of the Twin Density in $YBa_2Cu_3O_{7-\delta}$ Thin-Films Sputtered Onto MgO Substrates" Applied Physics Letters, **58**, 2171 (1991).

105. H.W.Zandbergen, R.Gronsky, K.Wang, and G.Thomas, "Structure of $(CuO)_2$ Double-Layers in Superconducting $YBa_2Cu_3O_7$" Nature, **331**, 596 (1988).

106. K.Char, M.Lee, R.W.Barton, A.F.Marshall, I.Bozovic, R.H.Hammond, M.R.Beasley, T.H.Geballe, A.Kapitulnik, and S.S.Laderman, "Properties of Y-Ba-Cu-O Thin-Films with Ordered Defect Structure - $Y_2Ba_4Cu_8O_{20-X}$" Physical Review B, **38**, 834 (1988).

107. J.Karpinski, S.Rusiecki, E.Kaldis, B.Bucher, and E.Jilek, "Phase-Diagrams of $YBa_2Cu_4O_8$ and $YBa_2Cu_{3.5}O_{7.5}$ in the Pressure Range 1 Bar Less-Than-Or-Equal-to PO_2 Less-Than-Or-Equal-to 3000 Bar" Physica C, **160**, 449 (1989).

108. J.Narayan, V.N.Shukla, S.J.Lukasiewicz, N.Biunno, R.Singh, A.F.Schreiner, and S.J.Pennycook, "Microstructure and Properties of $YBa_2Cu_3O_{9-\delta}$ Superconductors with Transitions at 90 and near 290 K" Applied Physics Letters, **51**, 940 (1987).

109. J.Tafto, M.Suenaga, and R.L.Sabatini, "Characterization of Planar Crystal-Lattice Defects in the High-Temperature Superconductor $YBa_2Cu_3O_7$" Applied Physics Letters, **52**, 667 (1988).

110. S.Bals, G.Van Tendeloo, G.Rijnders, M.Huijben, V.Leca, and D.H.A.Blank, "Transmission electron microscopy on interface engineered superconducting thin films" Ieee Transactions on Applied Superconductivity, **13**, 2834 (2003).

111. R.K.Williams, K.B.Alexander, J.Brynestad, T.J.Henson, D.M.Kroeger, T.B.Lindemer, G.C.Marsh, J.O.Scarbrough, and E.D.Specht, "Oxidation Induced Decomposition of $YBa_2Cu_3O_{7-X}$" Journal of Applied Physics, **70**, 906 (1991).

112. Milton Ohring, "Materials Science of Thin Films. Deposition & Structure" Second Edition. Academic Press. New York (2002).

113. F.Sandiumenge, T.Puig, J.Rabier, J.Plain, and X.Obradors, "Optimization of flux pinning in bulk melt textured 1-2-3 superconductors: Bringing dislocations under control" Advanced Materials, **12**, 375 (2000).

114. A.F.Marshall, K.Char, R.W.Barton, A.Kapitulnik, and S.S.Laderman, "Microstructural Interaction of $Y_2Ba_4Cu_8O_{16}$ Stacking-Faults Within $YBa_2Cu_3O_{7-X}$" Journal of Materials Research, **5**, 2049 (1990).

115. J.W.Matthews, "Defects Associated with Accommodation of Misfit Between Crystals" Journal of Vacuum Science & Technology, **12**, 126 (1975).

116. C.L.Jia, R.Hojczyk, M.Faley, U.Poppe, and K.Urban, "The interfaces in $YBa_2Cu_3O_7/BaTbO_3$ and $PrBa_2Cu_3O_7/BaTbO_3$ heterostructure thin films" Philosophical Magazine A-Physics of Condensed Matter Structure Defects and Mechanical Properties, **79**, 873 (1999).

117. F.C.Frank and J.H.Merwe, "One-Dimensional Dislocations" Proc. R. Soc. (London), **A 198**, 216 (1949).

118. S.J.Pennycook, M.F.Chisholm, D.E.Jesson, R.Feenstra, S.Zhu, X.Y.Zheng, and D.J.Lowndes, "Growth and Relaxation Mechanisms of $YBa_2Cu_3O_{7-X}$ Films" Physica C, **202**, 1 (1992).

119. M.Yeadon, M.Aindow, F.Wellhofer, and J.S.Abell, "Topographical development and misfit relief in laser-ablated heteroepitaxial $YBa_2Cu_3O_{7-\delta}$ thin films" Journal of Crystal Growth, **172**, 145 (1997).

120. Y.Chen and J.Washburn, "Structural transition in large-lattice-mismatch heteroepitaxy" Physical Review Letters, **77**, 4046 (1996).

121. D.E.Jesson, S.J.Pennycook, J.M.Baribeau, and D.C.Houghton, "Direct Imaging of Surface Cusp Evolution During Strained-Layer Epitaxy and Implications for Strain Relaxation" Physical Review Letters, **71**, 1744 (1993).

122. F.Leonard and R.C.Desai, "Implications of a model for instability during film growth for strained InGaAs and SiGe layers" Applied Physics Letters, **74**, 40 (1999).

123. J.M.Huijbregtse, B.Dam, R.C.F.van der Geest, F.C.Klaassen, R.Elberse, J.H.Rector, and R.Griessen, "Natural strong pinning sites in laser-ablated $YBa_2Cu_3O_{7-\delta}$ thin films" Physical Review B, **62**, 1338 (2000).

124. Y.Chen, X.W.Lin, Z.LilientalWeber, J.Washburn, J.F.Klem, and J.Y.Tsao, "Dislocation formation mechanism in strained $In_xGa_{1-x}As$ islands grown on GaAs(001) substrates" Applied Physics Letters, **68**, 111 (1996).

125. P.A.Langjahr, F.F.Lange, T.Wagner, and M.Ruhle, "Lattice mismatch accommodation in perovskite films on perovskite substrates" Acta Materialia, **46**, 773 (1998).

126. C.J.Lu, "Type of dissociated misfit dislocation in perovskite films on $LaAlO_3$" Applied Physics Letters, **85**, 2768 (2004).

127. T.Suzuki, Y.Nishi, and M.Fujimoto, "Analysis of misfit relaxation in heteroepitaxial $BaTiO_3$ thin films" Philosophical Magazine A-Physics of Condensed Matter Structure Defects and Mechanical Properties, **79**, 2461 (1999).

128. L.B.Freund, "A Criterion for Arrest of A Threading Dislocation in A Strained Epitaxial Layer Due to An Interface Misfit Dislocation in Its Path" Journal of Applied Physics, **68**, 2073 (1990).

129. Z.Mao and K.M.Knowles, "Dissociation of lattice dislocations in $SrTiO_3$" Philosophical Magazine A-Physics of Condensed Matter Structure Defects and Mechanical Properties, **73**, 699 (1996).

130. J.Nishigaki, K.Kuroda, and H.Saka, "Electron-Microscopy of Dislocation-Structures in $SrTiO_3$ Deformed at High-Temperatures" Physica Status Solidi A-Applied Research, **128**, 319 (1991).

131. Y.M.Zhu, M.Suenaga, J.Tafto, and D.O.Welch, "Variable Nature of Twin Boundaries in $YBa_2Cu_3O_{7-\delta}$ and Its Alloys" Physical Review B, **44**, 2871 (1991).

132. W.K.Kwok, U.Welp, G.W.Crabtree, K.G.Vandervoort, R.Hulscher, and J.Z.Liu, "Direct Observation of Dissipative Flux Motion and Pinning by Twin Boundaries in $YBa_2Cu_3O_{7-\delta}$ Single-Crystals" Physical Review Letters, **64**, 966 (1990).

133. B.M.Lairson, S.K.Streiffer, and J.C.Bravman, "Vortex Pinning and Twin Boundaries in $YBa_2Cu_3O_{7-\delta}$ Thin-Films" Physical Review B, **42**, 10067 (1990).

134. J.Plain, T.Puig, F.Sandiumenge, X.Obradors, and J.Rabier, "Microstructural influence on critical currents and irreversibility line in melt-textured $YBa_2Cu_3O_{7-x}$ reannealed at high oxygen pressure" Physical Review B, **65** (2002).

135. J.L.Manus-Driscoll, S.R.Foltyn, Q.X.Jia, H.Wang, A.Serquis, B.Maiorov, L.Civale, Y.Lin, M.E.Hawley, M.P.Maley, and D.E.Peterson, "Systematic enhancement of in-field critical current density with rare-earth ion size variance in superconducting rare-earth barium cuprate films" Applied Physics Letters, **84**, 5329 (2004).

136. J.L.Manus-Driscoll, S.R.Foltyn, Q.X.Jia, H.Wang, A.Serquis, L.Civale, B.Maiorov, M.E.Hawley, M.P.Maley, and D.E.Peterson, "Strongly enhanced current densities in superconducting coated conductors of $YBa_2Cu_3O_{7-x}$+$BaZrO_3$" Nature Materials, **3**, 439 (2004).

137. T.Haugan, P.N.Barnes, I.Maartense, C.B.Cobb, E.J.Lee, and M.Sumption, "Island growth of Y_2BaCuO_5 nanoparticles in (211(~ 1.5 nm)/123(~ 10) (nm))xN composite multilayer structures to enhance flux pinning of $YBa_2Cu_3O_{7-\delta}$ films" Journal of Materials Research, **18**, 2618 (2003).

138. K.V.Paulose, J.Koshy, and A.D.Damodaran, "Superconductivity in $YBa_2Cu_3O_{7-\delta}$-ZrO_2 Systems" Superconductor Science & Technology, **4**, 98 (1991).

139. Patent, In preparation (2006).

140. T.Schober and H.G.Bohn, "Water vapor solubility and electrochemical characterization of the high temperature proton conductor $BaZr_{0.9}Y_{0.1}O_{2.95}$" Solid State Ionics, **127**, 351 (2000).

141. S.Kang, A.Goyal, J.Li, A.A.Gapud, P.M.Martin, L.Heatherly, J.R.Thompson, D.K.Christen, F.A.List, M.Paranthaman, and D.F.Lee, "High-performance high-T_c superconducting wires" Science, **311**, 1911 (2006).

142. R.Cloots, B.Robertz, F.Auguste, A.Rulmont, H.Bougrine, N.Vandewalle, and M.Ausloos, "Effect of $BaZrO_3$ additions on the microstructure and physical properties of melt-textured Y-123 superconducting materials" Materials Science and Engineering B-Solid State Materials for Advanced Technology, **53**, 154 (1998).

143. Y.Y.Luo, Y.C.Wu, X.M.Xiong, Q.Y.Li, W.Gawalek, and Z.H.He, "Effects of precursors with fine $BaZrO_3$ inclusions on the growth and microstructure of textured YBCO" Journal of Superconductivity, **13**, 575 (2000).

144. Zhang J.L. and Evetts J.E., "Zirconium Doping of $YBa_2Cu_3O_{7-x}$ Ceramic Superconductor" Chinese Journal of Physics, **31**, 1139 (1993).

145. A.Goyal, S.Kang, K.J.Leonard, P.M.Martin, A.A.Gapud, M.Varela, M.Paranthaman, A.O.Ijaduola, E.D.Specht, J.R.Thompson, D.K.Christen, S.J.Pennycook, and F.A.List, "Irradiation-free, columnar defects comprised of self-assembled nanodots and nanorods resulting in strongly enhanced flux-pinning in $YBa_2Cu_3O_{7-\delta}$ films" Superconductor Science & Technology, **18**, 1533 (2005).

LIST OF PUBLICATIONS

"Chemical Solution Growth of Superconductors: a New Path Towards High Critical Current Coated Conductors". X. Obradors, T. Puig, A. Pomar, N. Mestres, F. Sandiumenge, S. Piñol, O. Castaño, A. Cavallaro, A. Palau, J. C. Gonzalez, M. Coll, J. Gazquez.. Physica C **408-410**, 913-914 (2004).

"Chemical Solution Deposition: a Path Towards Low Cost Coated Conductors". X. Obradors, T. Puig, A. Pomar, F. Sandiumenge, S. Piñol, N. Mestres, O. Castaño, M. Coll, A. Cavallaro, A. Palau, J. Gazquez, J. C. Gonzalez, J. Gutierrez, N. Roma, S.Ricart, J. M. Moreto, M. D. Rossell, G. van Tendeloo. Supercond.Sci.Technol. **17**, 1055-1064 (2004).

"Biaxial texture analysis of $YBa_2Cu_3O_7$ coated conductors by micro-Raman spectroscopy". J. C. González, N. Mestres, T. Puig, J. Gàzquez, F. Sandiumenge, X. Obradors, A. Usoskin, Ch. Jooss, H. C. Freyhardt, and R. Feenstra. Phys. Rev. B. **70**, 094525 (2004).

"High Jc YBCO Thin Films and Multilayers Grown by Chemical Solution Deposition". A. Pomar, M. Coll, A. Cavallaro, J. Gazquez, J. C. Gonzalez, N. Mestres, F. Sandiumenge, T. Puig, X. Obradors. IEEE Trans.on Appl.Supercond. **15**, 2747-2750 (2005).

"The influence of Growth Conditions on the Microstructure and Critical Currents of TFA-MOD $YBa_2Cu_3O_7$ Films". T. Puig, J. C. Gonzalez, A. Pomar, N. Mestres, O. Castaño, M. Coll, J. Gazquez, F. Sandiumenge, S. Piñol, X. Obradors. Supercond.Sci.Technol. **18**, 1141-1150 (2005).

"Mechanisms of nanostructural and morphological evolution of CeO_2 functional films by chemical solution deposition". F. Sandiumenge, A. Cavallaro, J. Gazquez, T. Puig, X. Obradors, J. Arbiol and H. C. Freyhardt. Nanotechnology **16** 1809-1813 (2005).

"All Chemical YBaCuO Coated Conductors on IBAD/YSZ Substrates". A. Pomar, A. Cavallaro, M. Coll, J. Gazquez, F. Sandiumenge, T. Puig, X. Obradors, H. C. Freyhardt. Supercond.Sci.Technol. **19**, L1-L4 (2006).

"All Chemical High Jc YBCO Multilayers with $SrTiO_3$ as Cap Layer". A. Pomar, M. Coll, A. Cavallaro, J. Gàzquez, J.C. González, N. Mestres, F. Sandiumenge, T. Puig, X. Obradors. J. Mater. Res. **21**, 1106-1116 (2006).

"Growth mechanism, microstructure and surface modification of nanostructured CeO_2 films by chemical solution deposition". A. Cavallaro, F. Sandiumenge, J. Gazquez, T. Puig, X. Obradors, J. Arbiol and H. C. Freyhardt. Adv. Funct. Mater. **16** 1363 (2006).

"Interface Control in all metalorganic deposited Coated Conductors: Influence on Critical Currents". A. Pomar, M. Coll, A. Cavallaro, J. Gàzquez, N. Mestres, F. Sandiumenge, T. Puig and X. Obradors. J. Mater. Res. **21**, 2176-2184 (2006).

"Stress induced spontaneous dewetting of heteroepitaxial $YBa_2Cu_3O_7$ thin films". M.Coll, J.Gázquez, A.Pomar, T.Puig, F.Sandiumenge and X.Obradors X. Obradors. Phys. Rev. B **73**, 075420 (2006).

"Progress towards all chemical superconducting YBCO Coated Conductors". X. Obradors, T. Puig, A. Pomar, F. Sandiumenge, N. Mestres, M.Coll, A. Cavallaro, N. Romà, , J.Gázquez, J. C. Gonázlez, O. Castaño, J. Gutierrez, A. Palau, K. Zalamova, S. Morlens, A. Hassini, M. Givert, S. Ricart, J. M. Moretó, S. Piñol, D. Isfort, J. Bock. Supercond. Sci. Technol. **19** S1-S14 (2006).

"Stress Relief control of Trifluoroacetate metal-organic solutions for YBCO film growth". K. Zalamova, N. Roma, A. Pomar, S. Morlens, T. Puig, J. Gazquez, F. Sandiumenge, A.E. Carrillo, S. Ricart, X. Obradors. Chemistry of Materials (2006) In press.

"Precursor evolution and mechanism of $YBa_2Cu_3O_x$ films by TFA metal-organic decomposition". J.Gázquez, F. Sandiumenge, M.Coll, A. Pomar, N. Mestres, T. Puig, X. Obradors, Y. Kihn, M.J. Casanove, C. Ballesteros. Chemistry of Materials (2006) In press.